DEVELOPMENT OF DOSIMETRY AND IMAGING TECHNIQUES FOR PRE-CLINICAL STUDIES OF GOLD NANOPARTICLE-AIDED RADIATION THERAPY

A Dissertation
Presented to
The Academic Faculty

By

Bernard Jones

In Partial Fulfillment
Of the Requirements for the Degree
Doctor of Philosophy in Nuclear Engineering

Georgia Institute of Technology

May 2011

Development of Dosimetry and Imaging Techniques for Pre-Clinical Studies of Gold Nanoparticle-Aided Radiation Therapy

Approved by:

Dr. Sang Hyun Cho, Adviser
School of Mechanical Engineering,
NRE/MP Department
Georgia Institute of Technology

Dr. Eric Elder
School of Mechanical Engineering,
NRE/MP Department
Georgia Institute of Technology

Dr. C.-K. Chris Wang
School of Mechanical Engineering,
NRE/MP Department
Georgia Institute of Technology

Dr. John Oshinski
School of Biomedical Engineering
Georgia Institute of Technology

Dr. Andrew Karellas
Department of Radiology
University of Massachusetts Medical School

ACKNOWLEDGEMENTS

I am very grateful to my advisor, Dr. Sang Hyun Cho, for his guidance and support as I completed this work. These projects were all based on his vision for gold nanoparticles. I would also like to thank the members of our lab group who worked on GNRT and XFCT with me, and made the long hours of scanning x-rays possible: Dr S-K Cheong, Arsalan Siddiqi, Nivedh Manohar, and Katie Dextraze.

I would like to thank the members of my committee for volunteering their time and expertise to improve my work: Dr. Chris Wang, Dr. Eric Elder, and Dr. John Oshinski of Georgia Tech, and Dr. Andrew Karellas of the University of Massachusetts Medical School.

There are many other people who contributed in other ways to this work, and I hope that my memory allows me to include them all. Thank you to Dr. Sunil Krishnan of the M.D. Anderson Cancer Center for his insight and help on the biological applications of GNRT and GNPs. Thank you to Dr. Vladimir Semenenko of the Medical College of Wisconsin for providing us with the NOREC code. Thank you to Dennis Denney at the GTRI Machine Shop for his patience in dealing with me to have our phantoms drawn up and fabricated. Thank you to Angela Lin of Georgia Tech for her expertise with MicroCT and allowing us to use their scanner.

TABLE OF CONTENTS

LIST OF TABLES

LIST OF FIGURES

LIST OF ABBREVIATIONS

CERT	Contrast-Enhanced Radiation Therapy
CT	Computed Tomography
EGFR	Epidermal Growth Factor Receptor
EPR	Enhanced Permeability and Retention
FDG-PET	Fluorine-deoxyglucose Positron Emission Tomography
GNP	Gold Nanoparticle
GNRT	Gold Nanoparticle-aided Radiation Therapy
MC	Monte Carlo
MDEF	Macroscopic Dose Enhancement Factor
mDEF	Microscopic Dose Enhancement Factor
ML-EM	Maximum Likelihood/Expectation Maximization
HER2	Human Epidermal Growth Factor Receptor 2
HOPG	Highly Oriented Pyrolitic Graphite
HVL	Half-Value Layer
PET	Positron Emission Tomography
PMMA	Polymethyl Methacrylate
SEM	Scanning Electron Microscopy
SNR	Signal-to-Noise Ratio
SPECT	Single Photon Emission Tomography
SSD	Source-to-Surface Distance
VEGF	Vascular Endothelial Growth Factor Receptor
XFCT	X-ray Fluorescence Computed Tomography
Z	Atomic Number

SUMMARY

Cancer is one of the leading causes of death worldwide, and affects roughly 1.5 million new people in the United States every year. One of the leading tools in the detection and treatment of cancer is radiation. Tumors can be detected and identified using computed tomography (CT) or positron emission tomography (PET) scans, and can then be treated with external beam radiotherapy or brachytherapy. By taking advantage of the physical properties of gold and the biological properties of nanoparticles, gold nanoparticles (GNPs) can be used to improve both cancer radiotherapy and imaging. By infusing a tumor with GNPs, either using passive extravasation of nanoparticles by the tumor vasculature or active targeting of antibody-conjugated nanoparticles to a specific tumor marker, the higher photon interaction cross-section of gold will cause more radiation dose to be deposited in the tumor during photon-based radiotherapy. In principle, this would allow escalation of dose to the tumor while not increasing the dose to normal healthy tissue. Additionally, if a tumor infused with GNPs was irradiated by an external kilo-voltage source, the fluorescence emitted by the gold atoms would allow one to localize and quantify the GNP concentration.

This work had two main aims: to quantify the GNP-mediated dose enhancement during gold nanoparticle-aided radiation therapy (GNRT) on a nanometer scale, and to develop a refined imaging modality capable of quantifying GNP location and concentration within a small-animal-sized object. In order to quantify the GNP-mediated dose enhancement

on a nanometer scale, a computational model was developed. This model combines both large-scale and small-scale calculations in order to accurately determine the heterogeneous dose enhancement pattern due to GNPs. The secondary electron spectra were calculated using a condensed history Monte Carlo code, which is able to accurately take into account changes in beam quality throughout the tumor and calculate the average energy spectrum of the secondary charged particles created. Then, the dose distributions due to these electron spectra were calculated on a nanometer scale using an event-by-event Monte Carlo code.

The second aim was to develop an imaging system capable of reconstructing a tomographic image of GNP location and concentration in a small animal-sized object by capturing gold fluorescence photons emitted during irradiation of the object by an external beam. This would not only allow for localization of GNPs during GNRT, but also facilitate the use of GNPs as imaging agents for drug-delivery or other similar studies. It has been shown that a benchtop system utilizing a pencil beam of polychromatic x-rays is capable of generating this kind of image. In theory, using a cone-beam x-ray source would allow for extensive parallelization of data collection and decreasing scanning time. Thus, the specific aim of the current study was to develop a cone-beam implementation of x-ray fluorescence computed tomography (XFCT) that meets realistic constrains on image resolution, detection limit, scan time, and dose. A Monte Carlo model of this imaging geometry was developed and used to test the methods of data acquisition and image reconstruction. The results of this study were then used to drive the production of a functioning benchtop, polychromatic cone-beam XFCT system.

CHAPTER 1

INTRODUCTION

1.1 – Cancer and Gold Nanoparticles

Cancer is one of the leading causes of death worldwide and affects roughly 1.5 million new people in the United States every year. One of the leading tools in the detection and treatment of cancer is radiation. Tumors can be detected and identified using Computed Tomography (CT) or Positron Emission Tomography (PET) scans, and can then be treated with external beam radiotherapy or brachytherapy. By taking advantage of the physical properties of gold and the biological properties of nanoparticles, gold nanoparticles (GNPs) can be used to improve both cancer radiotherapy and imaging.

GNPs are an attractive option for these applications due to both the chemical properties of gold and the tumor specificity of properly-sized nanoparticles. Gold is chemically inert, biologically non-reactive, and molecularly stable. Nanoparticle specificity to the tumor can be accomplished simply by "passive" targeting, which relies on the leaky vasculature of tumors.[1] Through a phenomenon known as "Enhanced Permeability and Retention (EPR),"[2] GNPs of sufficiently small size are able to penetrate the tumor vasculature and interstitium, resulting in an elevated concentration of nanoparticles in the tumor as compared to that of normal tissue. In addition, nanoparticles can be conjugated to an array of tumor-specific biomarkers under an "active" targeting scenario. These potential targets include tumor markers such as epidermal growth factor receptor

(EGFR)[3] and human epidermal growth factor receptor-2 (HER2),[4] and mediators of angiogenesis such as vascular endothelial growth factor (VEGF).[5] Whereas antibody conjugation would localize the nanoparticles to the surface of cancerous cells, other biomarkers could concentrate the nanoparticles inside the cells. For instance, deoxyglucose could bring gold nanoparticles into metabolically active cells via a mechanism similar to fluorine-18 deoxyglucose positron emission tomography (FDG-PET) imaging.[6]

By infusing a tumor with GNPs, either using passive extravasation of nanoparticles by the tumor vasculature or active targeting of antibody-conjugated nanoparticles to a specific tumor marker, the higher photon cross-section of gold will cause more radiation dose to be deposited in the tumor during photon-based radiotherapy. In principle, this would allow escalation of dose to the tumor while not increasing the dose to normal healthy tissue. Additionally, if a tumor infused with GNPs was irradiated by an external kilo-voltage source, the fluorescence emitted by the gold atoms would allow one to localize and quantify the GNP concentration.

1.2 – Gold Nanoparticle-aided Radiation Therapy

Mechanisms of Interaction Enhancement

Photon-based radiation therapy relies on the energy deposition within a tumor by secondary electrons created due to various physical interactions between photons and tumor tissue. Most advances in photon-based radiation therapy have been made through modifications to the radiation treatment field, either by modifying the radiation quality of

sources (such as increasing beam energy to MV range) or by improving the conformity of the photon beam to the tumor (such as 3D Conformal Radiotherapy, Intensity Modulated Radiation Therapy, Arc Therapy). However, by adjusting the photon interaction probabilities of tumor, it would be possible to selectively increase the tumor dose during photon-based radiation therapy.

$$\frac{\tau}{\rho} \propto \left(\frac{Z}{h\upsilon} \right)^3 \qquad \text{Eq. 1.2.1}$$

Equation 1.2.1 shows the proportionality among the photoelectric mass attenuation coefficient, τ/ρ, the atomic number of the interaction medium, Z, and the energy of the incoming photon, $h\nu$. The probability of photoelectric interactions increases as the third power of Z, and decreases as the third power of the energy. In principle, since the probability of photoelectric absorption drastically increases with the atomic number (Z) of the medium, infusion of the tumor with any high Z substance during photon irradiation would result in a greater fraction of the incident photon energy being imparted without escalation of damage to the surrounding healthy tissue. Figure 1.2.1 (adapted from Ref. 20) shows the amount by which the attenuation coefficient of tissue is increased with the addition of small amounts of gold, and it can be seen that there is a significant increase in interaction probability for low energy photons.

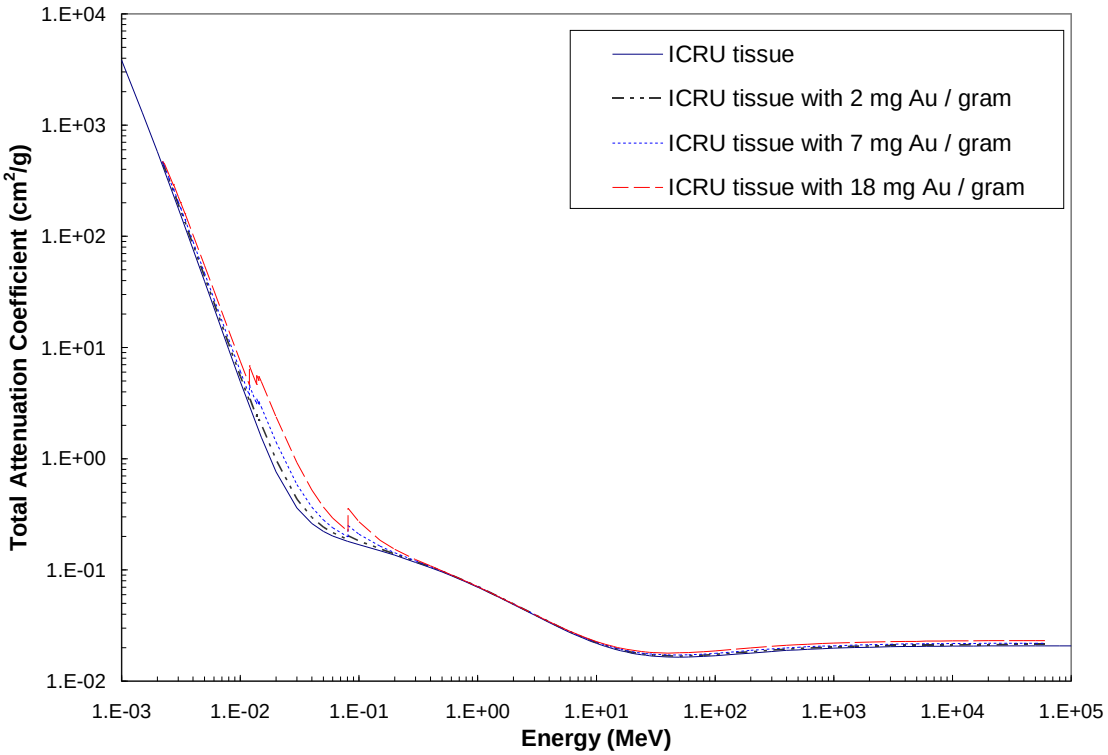

Figure 1.2.1: Increase in attenuation coefficient due to the addition of small concentrations of gold to tissue (Adapted from Ref. 20).

Contrast-Enhanced Radiation Therapy

Researchers have examined several methods of radiosensitization/dose enhancement using high-Z materials, focusing mainly on iodine or other similar CT contrast agents during kilo-/mega-voltage irradiation.[7-14] Iodine (Z=53) is a widely used contrast agent for CT due to the same principles described above: namely, increased photon absorption due to the Z^3 dependence of the photoelectric cross section. Materials with high iodine content can be injected intravenously into a patient, and the restriction of these compounds to the circulatory system or other organs can create contrast in the resulting image where there may not be any noticeable material difference otherwise. This is an especially powerful tool for imaging blood vessels. However, it was seen in dose

measurements during imaging with contrast agents that the increased interaction probability was resulting in increases to the dose deposited during imaging.[15]

This mechanism forms the basis of a method of radiotherapy dose enhancement known as Contrast Enhanced Radiation Therapy (CERT). In this technique, the therapeutic dose of x-rays delivered to an object is increased in regions of higher iodine content. It was seen that CERT using iodine was capable of enhancing dose deposition during *in-vitro* treatment using 20-110 keV (effective) beams by as much as a factor of 3 at iodine concentrations of 5% by volume.[7] This study also reported a significant increase in tumor regression in mice by using intratumoral injection of iodine followed by irradiation by 100 kVp x-rays, as compared to x-ray therapy alone. These results were confirmed by subsequent *in vitro*[8] and *in vivo*[9] studies.

Gold Nanoparticle-aided Radiation Therapy

An approach utilizing GNPs has the potential to be more effective than previous approaches due to both the higher Z of gold and the greater tumor specificity of properly-sized nanoparticles. For example, an animal study demonstrated that mice irradiated with 250 kVp x-rays after intravenous injection of GNPs demonstrated remarkable tumor regression and long-term survival compared to mice irradiated without gold present.[16-17] Additionally, it has been demonstrated that gold nanoparticle-aided radiation therapy (GNRT) can be more effective at treating traditionally radio-resistant tumors such as squamous cell carcinoma in mice.[18] These encouraging outcomes could be attributed to the dose enhancement to the tumor and tumor vasculature due to GNPs and kilovoltage x-

rays. The dose enhancement due to GNPs and various photon sources was quantified by a subsequent Monte Carlo[19-20] study, and demonstrated that the macroscopic dose enhancement (shown in Figure 1.2.2, adapted from Ref. 20) depended on both the gold concentration and photon beam quality. Additionally, it was shown that this enhancement had the potential to exceed several hundred percent for lower energy sources.[19] Some of these results were independently confirmed by a non-Monte Carlo theoretical study based on the energy-dependent absorption coefficients of different materials.[21]

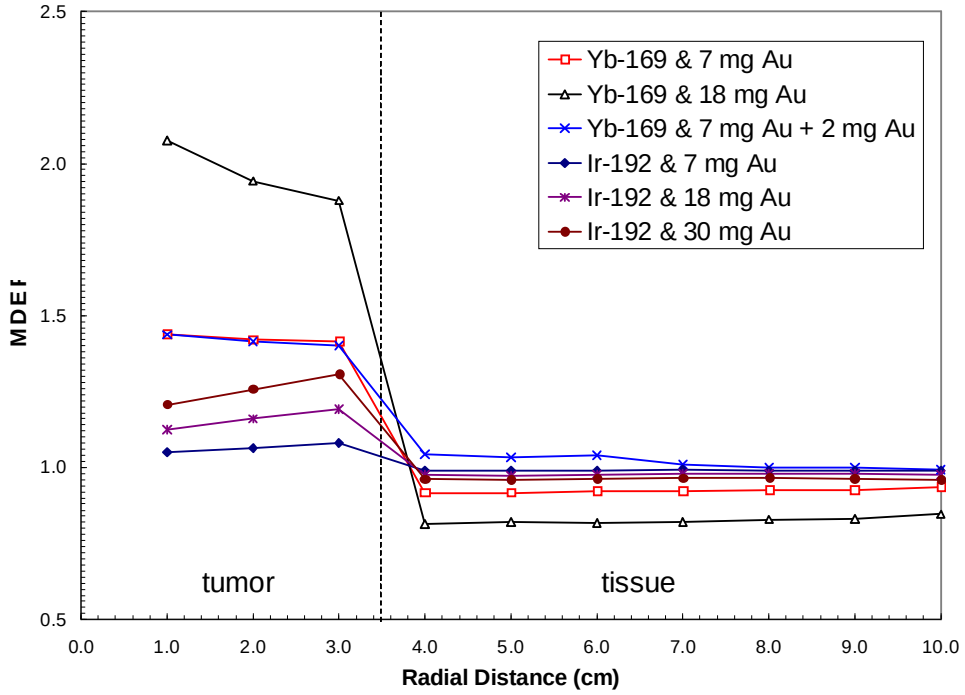

Figure 1.2.2: Macroscopic Dose Enhancement Factor (MDEF) for tumors loaded with 0.7%-3.0% Au by weight under irradiation by ^{169}Yb and ^{192}Ir (Adapted from Ref. 20). MDEF represents the amount by which the macroscopic dose is enhanced by the addition of GNPs, and is equal to the ratio of the dose during irradiation in the presence/absence of GNPs.

In a recent Monte Carlo study, it has also been shown that gold enhances dose to a tumor through an increase in the amount of photoelectric absorption, which can lead to an

increase of up to two orders of magnitude in the number of photoelectrons and Auger/Coster-Kronig electrons produced, depending on the energy spectra of photon sources.[20] Figure 1.2.2 (adapted from Ref. 20) shows that macroscopic dose enhancement (MDEF) seen in this study was as high as 100% for ^{192}Ir and ^{169}Yb photons sources irradiating tumors loaded with 0.7%-3.0% Au by weight. Due to these spectral considerations, it is important to carefully choose the photon source spectrum to maximize the fraction of photoelectric absorptions. Brachytherapy is well-suited to GNRT, as typical radionuclide seed sources such as ^{125}I, ^{103}Pd, and ^{192}Ir emit photons primarily in the keV range. Photoelectric absorption can be enhanced further by selecting a source with a preponderance of photons just above the absorption edges of gold. For example, ^{169}Yb has an intensity-weighted average energy of about 93 keV,[22] just exceeding the gold K-edge of 80.7 keV.

While it has been demonstrated computationally that GNPs can enhance the dose during brachytherapy by up to about 70% macroscopically[20] (or on average across the tumor) at a tumor gold concentration deemed achievable *in vivo*[16] (i.e., 7 mg per g tumor after an intravenous injection of 1.9 nm diameter GNPs), it is not known exactly how a nanoparticle influences the dose on a nanometer or cellular scale. Due to the short ranges of 10-100 keV electrons, it is likely that the dose due to secondary electrons from GNPs may be concentrated in the vicinity of GNPs themselves, leading to an even more dramatic increase in the dose to nearby tumor cells. Consequently, it is reasonable to argue radiobiological outcomes (e.g., radiosensitization) from GNRT could be better correlated with the dose enhancement estimated microscopically on a nano-/cellular-scale

than that estimated macroscopically. Moreover, the spatial variation of microscopic dose enhancement could be crucial in deciding between passive or active nanoparticle targeting scenarios.

Unfortunately, current macroscopic dose estimation methods[19-20] which rely on condensed history Monte Carlo calculations are unable to accurately determine the localized enhancement of radiation dose on the small scale (nm - μm), as the typical electron step size of these codes is on the order of millimeters. Additionally, as the dose-enhancement process is dominated by low-energy (1-10 keV) Auger/photo-electrons, condensed history codes have some difficulty in accurately determining the spatial distribution of dose deposition of these short-ranged electrons. Therefore, it is necessary to utilize an approach which can perform these small scale calculations, such as an event-by-event Monte Carlo technique.

1.3 – X-Ray Fluorescence Computed Tomography for GNP Localization

Emission tomography has a long history of successful application in the field of radiology. In general, this technique involves generating a tomographic image of activity inside an object by detecting radiation emitted by the substance in question. Typically, the substance is a radioisotope which emits either a single photon (Single Photon Emission Tomography, SPECT) or a positron, which annihilates and emits two photons (Positron Emission Tomography, PET). This imaging modality hinges on the successful detection of radiation that is specific to the radioisotope, such as the 140-keV photon in ^{99m}Tc SPECT or the dual 511-keV annihilation photons in PET. An image can also be

reconstructed by capturing photons stimulated by irradiation with an external beam of radiation, instead of injection radioactivity directly. Such imaging modalities can be called *Stimulated* Emission Tomography. For instance, it is possible to verify dose delivery in proton radiotherapy by performing PET imaging to detect ^{11}C and ^{15}O produced during interactions of protons with tissue.[23] This principle of Stimulated Emission Tomography forms the basis of X-Ray Fluorescence Computed Tomography (XFCT), which involves the detection of characteristic fluorescence x-rays emitted by an object under irradiation by an external x-ray beam.

Within the last decade, some notable applications utilizing GNPs have emerged for cancer imaging [6, 24-27], radiation therapy [16-20, 28], and thermal therapy [29-32]. While the development of these applications relies on animal studies, previous research effort was often hindered or delayed by some research challenges inadequately addressed. One such challenge appears to be the lack of an effective *in-vivo* assay or imaging tool to determine the biodistribution of GNPs injected into animals. Without such a tool, the biodistribution of GNPs needs to be determined via *ex-vivo* analysis after sacrificing animals. In principle, it would be possible to determine the biodistribution of GNPs *in vivo* if the spatial distribution and amount of GNPs within a tumor and other critical organs can be quantified by imaging a live animal injected with GNPs.

In order to calculate the amount of dose enhancement that would occur during GNRT, one must be able to quantify the amount of GNPs within a tumor or other critical organs *in vivo*. Since gold is a high atomic number substance (Z=79), and its K-Shell

fluorescence (~65 keV) is able to escape a small animal-sized object, XFCT is a promising approach to addressing these imaging challenges. XFCT is typically performed using monochromatic x-rays, such as those from a synchrotron, to take advantage of photoelectric edge absorption in the interrogated material.[33-36] This method has been used to quantify the distribution of substances within a homogeneous medium[37] as well as iodine within a thyroid sample.[38] However, this technique does not lend itself to *in-vivo* imaging due to high dose rate and limited access of synchrotron beams. Therefore, it would be advantageous to develop a benchtop XFCT system capable of measuring the distribution and concentration of GNPs *in vivo*.

There are a handful of existing imaging techniques which may be able to meet the technical criteria above. Optical spectroscopy has been found feasible for quantification of nanoparticle concentration *in vivo*.[26, 39] GNPs may also be detected in certain x-ray computed tomography (CT) imaging situations, similar to Iodine contrast.[25] There are also several emerging imaging modalities which may prove capable of locating gold nanoparticles in organs, such as dual energy CT[40] and K-edge x-ray CT.[41] However, it is not known whether these newer techniques will have the sensitivity required to detect biologically relevant concentrations of GNPs. To our knowledge, no single imaging modality apart from XFCT is able to simultaneously determine both the distribution and concentration of GNPs *in vivo*. Recently, XFCT has been shown to be feasible using a 110 kVp polychromatic, pencil-beam source.[42] This technique was used to generate an image of the spatial distribution and concentration of GNP-loaded regions in a 5-cm-

diameter plastic phantom. However, this technique requires refinement for *in vivo* applications due to excessive dose and prolonged scan time.

1.4 – GNRT and XFCT: Aims of Current Work

While GNRT and XFCT are already very powerful tools for radiation-based treatment and imaging, they could be made more powerful with further refinement. Investigations into the mechanisms of dose enhancement for GNRT are currently based on large scale, macroscopic calculations of radiation dose enhancement.[19-20] Additionally, tools to quantify heterogeneous dose enhancement patterns for GNRT must be based on the distributions and concentration of GNPs within the tumor, which currently require synchrotron-based non-destructive analysis or *ex vivo* analysis after the sacrifice of live animals. Therefore, this work had two main aims: to quantify the GNP-mediated dose enhancement during GNRT on a nanometer scale, and to develop a refined imaging modality capable of quantifying GNP location and concentration within a small-animal-sized object.

First, in order to quantify the GNP-mediated dose enhancement on a nanometer scale, a computational model was developed. In this model, the spectrum of secondary electrons emitted by gold and water under irradiation with different photon sources was determined by Monte Carlo methods. Then, event-by-event Monte Carlo transport of these electrons was used to calculate the resulting dose from a hypothetical nanoparticle of gold or water.

This model combined both large-scale and small-scale calculations in order to accurately determine the heterogeneous dose enhancement pattern due to GNPs. The secondary electron spectra were calculated using a condensed history Monte Carlo code, which is able to accurately take into account changes in beam quality throughout the tumor and calculate the average energy spectrum of the secondary charged particles created. Then, the dose distributions due to these electron spectra were calculated on a nanometer scale using an event-by-event Monte Carlo code.

The second aim was to develop an imaging system capable of reconstructing a tomographic image of GNP location and concentration in a small animal-sized object by capturing gold fluorescence photons emitted during irradiation of the object by an external beam. This would not only allow for localization of GNPs during GNRT, but also facilitate the use of GNPs as imaging agents for drug-delivery or other similar studies. It has been shown that a benchtop system utilizing a pencil beam of polychromatic x-rays is capable of generating this kind of image.[42] In theory, using a cone-beam x-ray source would allow for extensive parallelization of data collection and decreasing scanning time. Thus, the specific aim of this study was to develop a cone-beam implementation of XFCT that meets realistic constrains on image resolution, detection limit, scan time, and dose. A Monte Carlo model of this imaging geometry was developed and used to test the methods of data acquisition and image reconstruction. The results of this study were then used to drive the production of a functioning benchtop, polychromatic cone-beam XFCT system.

CHAPTER 2

GOLD NANOPARTICLE-AIDED RADIATION THERAPY

2.1 – Introduction

Traditionally, methods to calculate the dose enhancement during photon-based radiotherapy due to gold nanoparticles (GNPs) have centered around macroscopic approaches.[19-20] These approaches are reasonable, as they constitute a direct test of the effect of GNPs. Using Monte Carlo methods, dose is recorded in a volume before and after the addition of GNPs, and the ratio of these two doses is the factor by which GNPs enhanced dose deposition. While this generates an accurate model of the macroscopic effects of GNPs, this approach is insufficient for three reasons. First, the nanoparticles are by definition small, even when compared to cells. Sizes of GNPs can range from 120 nm[43] to as small as 1.9 nm.[16] Second, dose is enhanced during GNRT primarily through the photoelectric effect and subsequent Auger emission,[20] and the range of these electrons is also small on cellular scales. For instance, the range of 10-50 keV electrons in water is 2.5 μm to 43 μm.[44] Third, the distribution of GNPs *in vivo* can be very heterogeneous.[30] Taken together, this would indicate that it may not be sufficient to assume a homogeneous pattern of dose enhancement, but rather that the enhancement may be concentrated within a few microns of the GNPs and that the overall enhancement is strongly dependent on the distribution of GNPs *in vivo*.

In this study, a three-step approach is taken in order to calculate the dose enhancement due to GNPs on a micro-/nano-meter scale. It is similar to the kernel-based approach taken in many radiotherapy dose calculation algorithms, where the directional dose kernel of electrons is convolved with the distribution of photon interactions in tissue. Consider the scanning electron microscopy (SEM) image shown in Figure 2.1.1, showing GNPs (gold nanoshells to be precise) appeared as white spots in tissue. Conventional condensed history Monte Carlo technique is unable to calculate the dose enhancement in this case directly, as the typical electron step size on the order of mm far exceeds the problem domain. However, the dose due to this heterogeneous distribution of GNPs could be calculated if the point dose kernel of a GNP was known. This point dose kernel could be calculated if the energy spectrum of the secondary electrons emitted by GNPs was known.

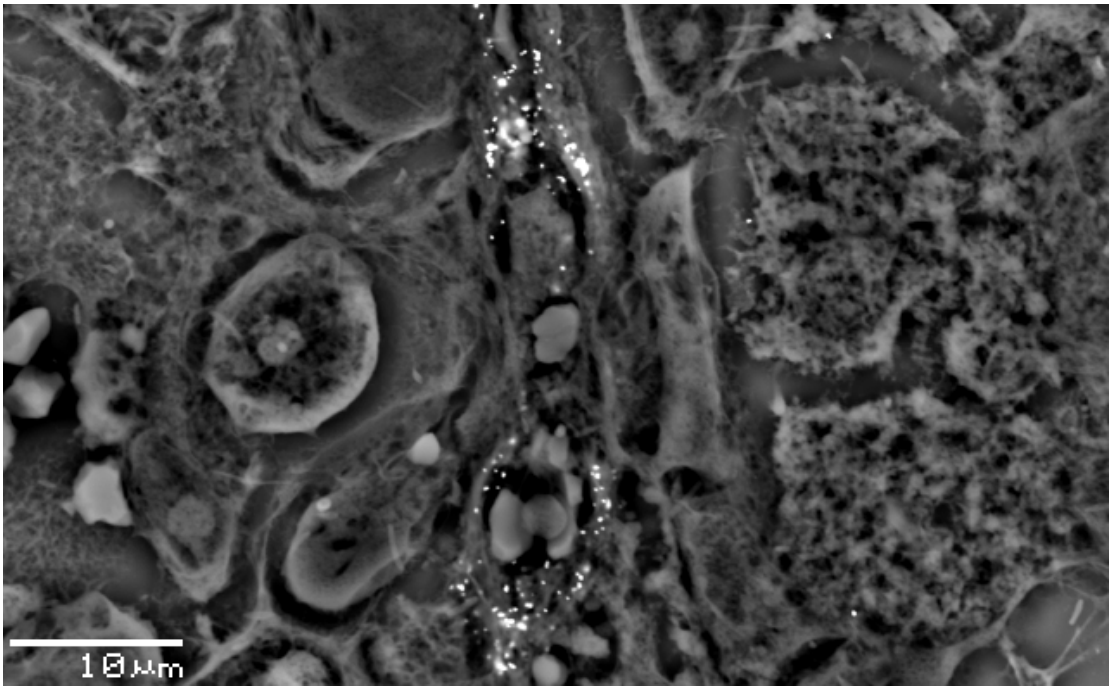

Figure 2.1.1: SEM image of gold nanoshells (appearing as white dots) in tissue.[30]

The steps of this nanoscale dose calculation are as follows. First, the spectrum of secondary electrons generated by gold and water during photon irradiation of a GNP-loaded water phantom is calculated using large-scale Monte Carlo calculations. These simulations determine, on average, the energy spectrum of secondary electrons, and take into account changes in the photon spectrum throughout the phantom. The second step is to calculate the point dose kernel of these electron spectra. Finally, these kernels are applied to the SEM image in Figure 2.0.1 in order to determine the effect of GNPs.

2.2 - Updates to Point Dose Kernels and Microscopic Dose

The aforementioned method for nanoscale dose calculations was first reported in a previous publication.[45] The spectrum of secondary electrons from atoms of gold and molecules of water resulting from irradiation by common photon sources (^{125}I, ^{103}Pd, ^{169}Yb, ^{192}Ir, 6 MV, 50 kV) have been reproduced in Appendix A for the sake of completeness. The calculations of the point dose kernels, microscopic dose enhancement factor, and microscopic dose enhancement to the sample SEM image have been improved, and the results presented in this publication are considered to be more accurate. Specifically, event-by-event Monte Carlo calculations using the NOREC code at locations very near the GNP have been improved, resulting in a more accurate estimation of the sub-micron point dose kernel. Additionally, the calculation of scaling factors for gold/water dose was also improved. To verify the methods used, benchmarking was performed against other similar codes, resulting in acceptable agreement.

2.3 - Electron Point Dose Kernels

In order to determine the microscopic dose distribution due to secondary electrons, an event-by-event (or detailed history) electron Monte Carlo code NOREC[46] was used. To obtain accurate results on a nanometer scale, it was important to utilize an event-by-event code rather than a condensed history code due to the fact that the intended spatial resolution of the dose distribution (< 1 μm) is much smaller than the typical electron step size used for condensed history codes such as EGSnrc or MCNP. The NOREC code has been benchmarked well against several other common condensed history Monte Carlo codes including EGS4 and ETRAN on a larger scale.[47-48] Accordingly, NOREC is expected to produce reliable results on a nanometer scale as well by virtue of its event-by-event electron transport algorithm, although calculated results on such a small scale are difficult to verify experimentally. NOREC is implemented as a C++ class which performs event-by-event transport of electrons in water for the energy range from 7.4 eV to 1 MeV. The effects of this energy limitation on sources with higher energy components such as ^{103}Pd and 6 MV x-ray are addressed during the presentation of the results. More details about NOREC can be found elsewhere.[46-47]

Benchmarking of NOREC Code

The current NOREC implementation was benchmarked against published values for dose kernels of monoenergetic eletrons.[47] The results of these benchmarks are shown in Figures 2.3.1-2. These figures show the scaled point dose kernels of 20 keV and 1 MeV electrons as a function of the r_0, the CSDA range. There were minor differences in some

parameters of the two dose kernel studies, such as the thickness of the dose scoring shell, location of the dose scoring shell, and number of histories; however, there is good agreement in the results. The current NOREC implementation was also benchmarked against the EDKnrc code.[49] For this simulation, two polyenergetic secondary electron spectra were used; namely, ^{169}Yb and 6 MV. Unlike the monoenergetic spectra, these dose kernels decrease strongly with distance, as the lower energy electrons do not travel as far as those with higher energy. As NOREC is an event-by-event code, it is expected that it will have more accurate results for the very short electron ranges considered. As seen in Figure 2.3.3, there is general agreement between the two codes; however, there are slight differences in the very low dose regions at an increased distance from the source. This is likely due to the condensed history method used by EGSnrc.

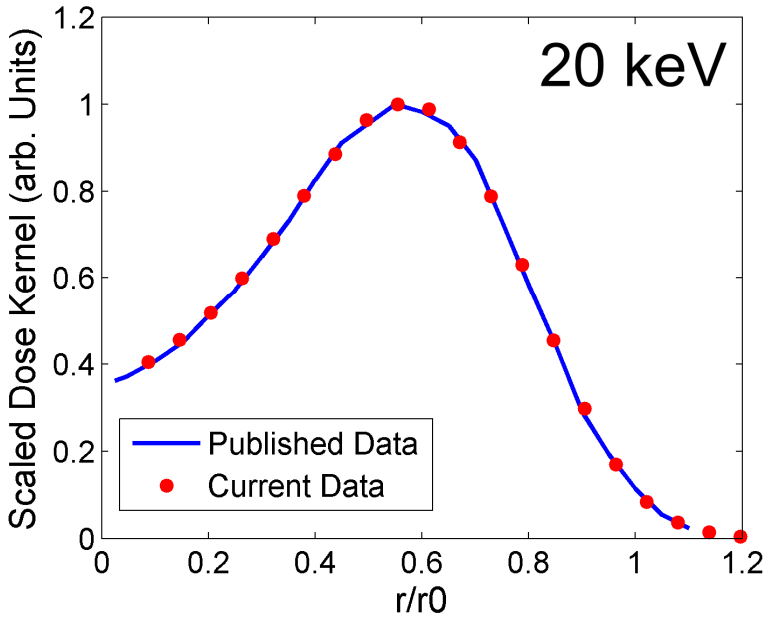

Figure 2.3.1: Benchmarking results for NOREC code for monoenergetic 20 keV electrons. The implementation of NOREC used in this work was benchmarked against existing scaled dose kernels for monoenergetic electrons using NOREC.[47]

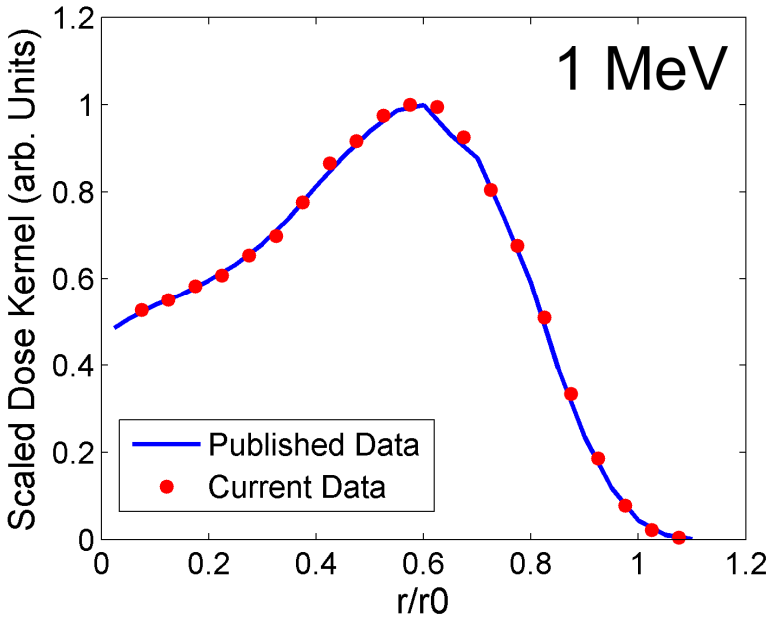

Figure 2.3.2: Benchmarking results for NOREC code for monoenergetic 1 MeV electrons. The implementation of NOREC used in this work was benchmarked against existing scaled dose kernels for monoenergetic electrons using NOREC.[47]

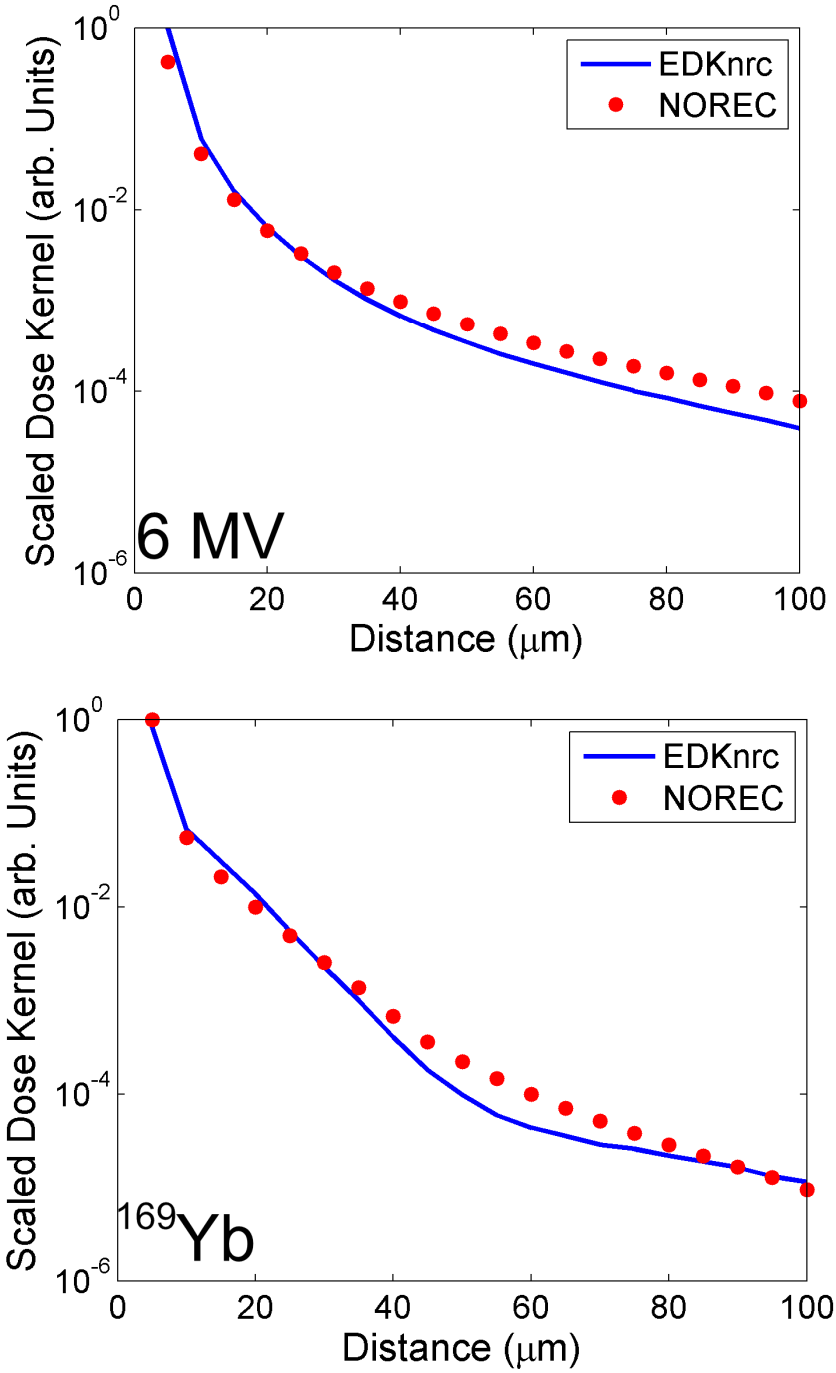

Figure 2.3.3: Benchmarking of NOREC code against EDKnrc, the dose kernel module of EGSnrc. These data are shown for two polyenergetic electron spectra resulting from irradiation by the photon sources shown (6 MV and ^{169}Yb).

NOREC Calculations

To calculate the dose kernels of the secondary electron spectra, NOREC calculations were performed by treating each secondary electron spectrum as a point source of electrons in an infinite medium of water. The number of histories for these calculations ranged from 0.5 to 50 M, depending on the secondary electron spectrum. The energy deposition of the electrons was recorded in a set of 100 nm-thick concentric spherical shells out to a maximum radial distance of 500 μm. The uncertainty in the results was estimated by tracking the number of energy deposition events in each shell and calculating the Poisson standard deviation of $N^{-1/2}$. The uncertainty in each significant region (with dose greater than 1% of maximum) in all cases was less than 1%.

In order to compare the dose point kernel results between different cases, several corrections were necessary. First, the dose per electron at each radial distance was divided by the maximum dose to yield the electron dose point kernel. Also, since NOREC simulations for gold and water were performed with the same number of electron histories, some corrections were necessary to scale the dose point kernels for gold to allow comparison with the water case under an identical photon irradiation scenario. The first scaling factor accounted for the different amount of electrons emitted by gold and water during spectrum acquisition, and was simply the ratio of the total number of electrons emitted by gold and water. The second factor accounted for the different concentration of water molecules and gold atoms approximating GNPs in a given volume of gold-loaded water medium (i.e. tumor) being irradiated during spectrum

acquisition and was a constant value of 142 in the current study, regardless of photon sources. The values of these scaling factors are shown in Table 2.3.1.

Table 2.3.1: Scaling Factors for Energy Deposition Kernels

Photon Source	Scaling Factor
^{169}Yb	82.3
^{125}I	255.2
^{103}Pd	254.1
^{192}Ir	14.6
50 kVp	232.4
6 MV	4.4

In order to quantify the effect of GNPs present within the tumor during radiation therapy, a comparison was made between the dose due to gold and water scaled dose point kernels. The ratio of these two values at a specific radial distance yielded the enhancement in dose kernel due to the inclusion of GNPs within the tumor. Considering only the dose originating from a single point of water, this number represents the factor by which the dose would be increased by replacing that point with a GNP. This enhancement in the dose kernel is defined as the microscopic dose enhancement factor (mDEF).

Results of NOREC Calculations

The relative electron dose point kernel for the six photon sources are shown in Figures 2.3.4-9(a) and is presented as a fraction of the maximum dose deposited at each radial distance. The dose point kernel depends strongly on the quality of the secondary electron spectrum, as evidenced by the sharp dose fall-off in the lower energy sources (e.g., ^{103}Pd,

^{125}I, and 50 kVp) as compared to the higher energy sources. For each source, the dose point kernel gives insight into the range of effect of GNPs during treatment. For ^{103}Pd, ^{125}I, and 50 kVp, it is apparent that GNPs would only significantly affect the region within 30-40 μm. For ^{169}Yb, the dose point kernel extends beyond 100 μm, while for ^{192}Ir and 6 MV x-rays the dose kernel extends out beyond the 100 μm range. In the case of the 6 MV x-ray dose kernel, NOREC was unable to simulate those secondary electrons with energy greater than 1 MeV. This limitation possibly introduced some uncertainty in the current dose point kernels for 6 MV x-rays, because the dose contribution from those omitted high energy secondary electrons within 500 μm radial distance was not properly taken into account. On the other hand, the effect of this uncertainty on the estimation of mDEF and microscopic dose enhancement for the test case was believed to be small, because the contribution of high energy secondary electrons originating from gold and water could roughly cancel each other when taking the ratios during the calculations.

The dose point kernel in terms of dose per source photon per GNP, or scaled dose point kernel, is shown in Figure 2.3.4-9(b). One can see the benefit of a lower energy source spectrum, as the increased contribution of photoelectric absorption in gold creates many more secondary electrons per incident photon. ^{125}I, ^{103}Pd, ^{169}Yb, and 50 kVp, all having a strong spectral component below the K-edge of gold, show a substantial increase in energy deposition within the 50 μm range. On the other hand, ^{169}Yb, with an average energy very close to the K-edge of gold, shows a large amount of electron energy deposition even as far away as 100 μm.

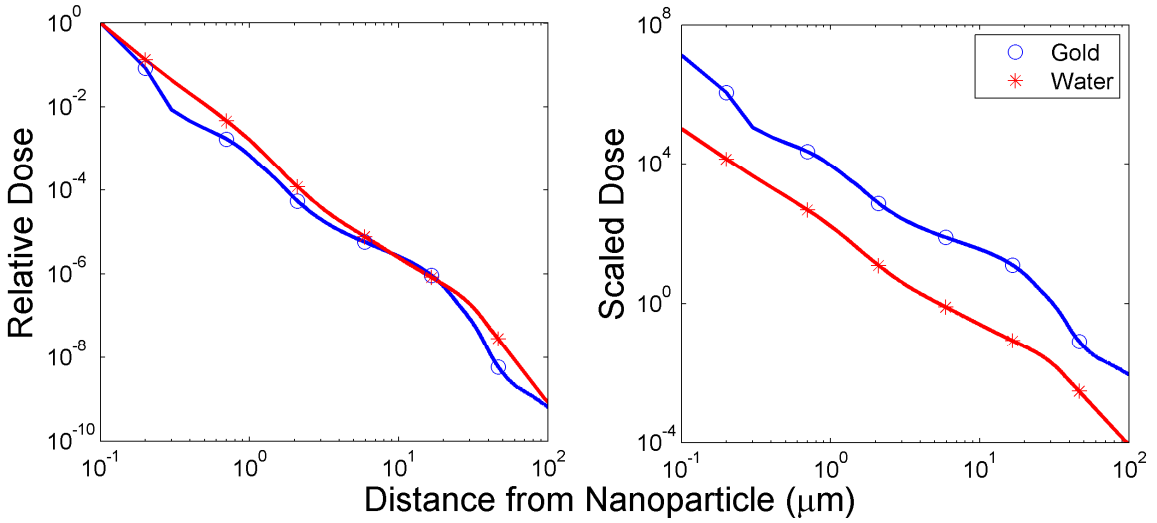

(a) (b)

Figure 2.3.4: **^{169}Yb** - (a) Relative Dose Point Kernels and (b) Scaled Dose Point Kernels in a water medium for a gold nanoparticle and a hypothetical water nanoparticle under irradiation by ^{169}Yb.

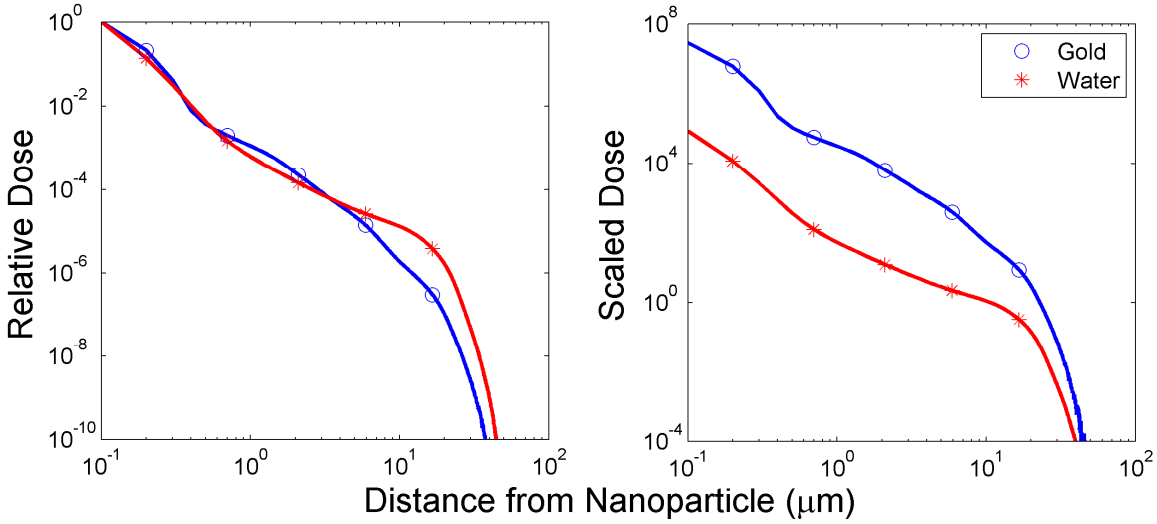

(a) (b)

Figure 2.3.5: **^{125}I** - (a) Relative Dose Point Kernels and (b) Scaled Dose Point Kernels in a water medium for a gold nanoparticle and a hypothetical water nanoparticle under irradiation by ^{125}I.

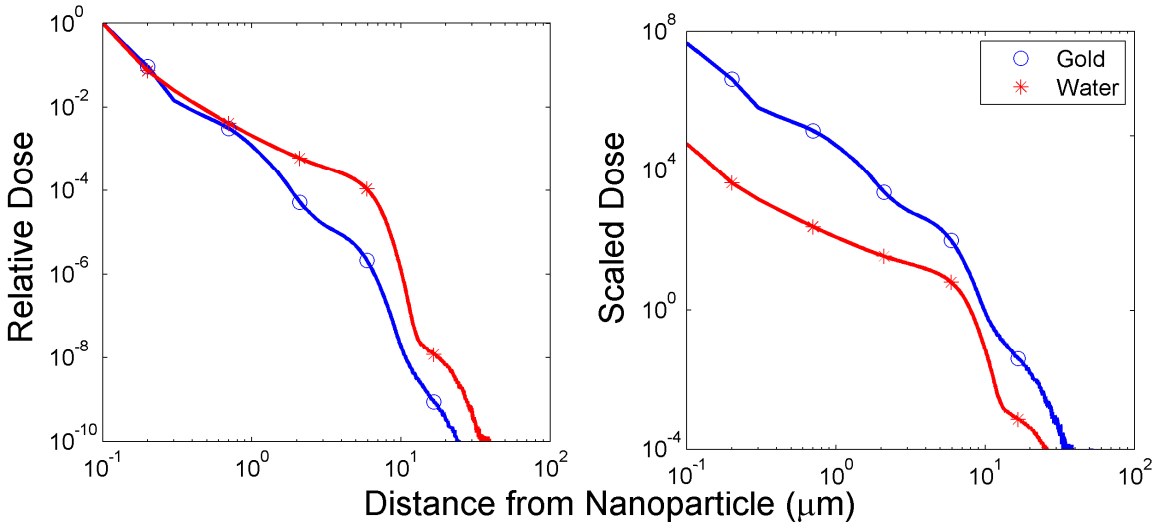

(a) (b)

Figure 2.3.6: **^{103}Pd** - (a) Relative Dose Point Kernels and (b) Scaled Dose Point Kernels in a water medium for a gold nanoparticle and a hypothetical water nanoparticle under irradiation by ^{103}Pd.

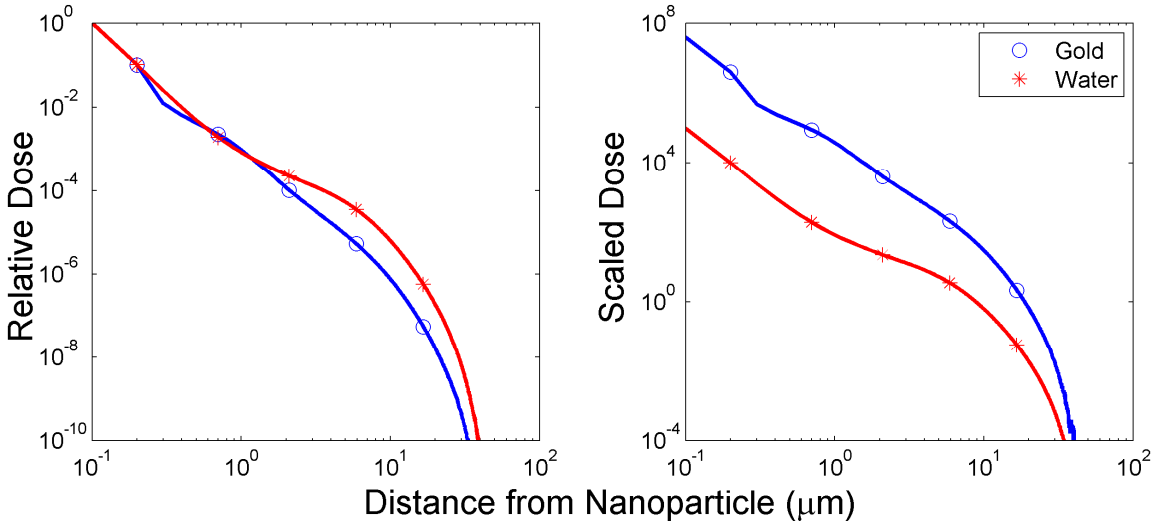

(a) (b)

Figure 2.3.7: **50 kVp** - (a) Relative Dose Point Kernels and (b) Scaled Dose Point Kernels in a water medium for a gold nanoparticle and a hypothetical water nanoparticle under irradiation by 50 kVp.

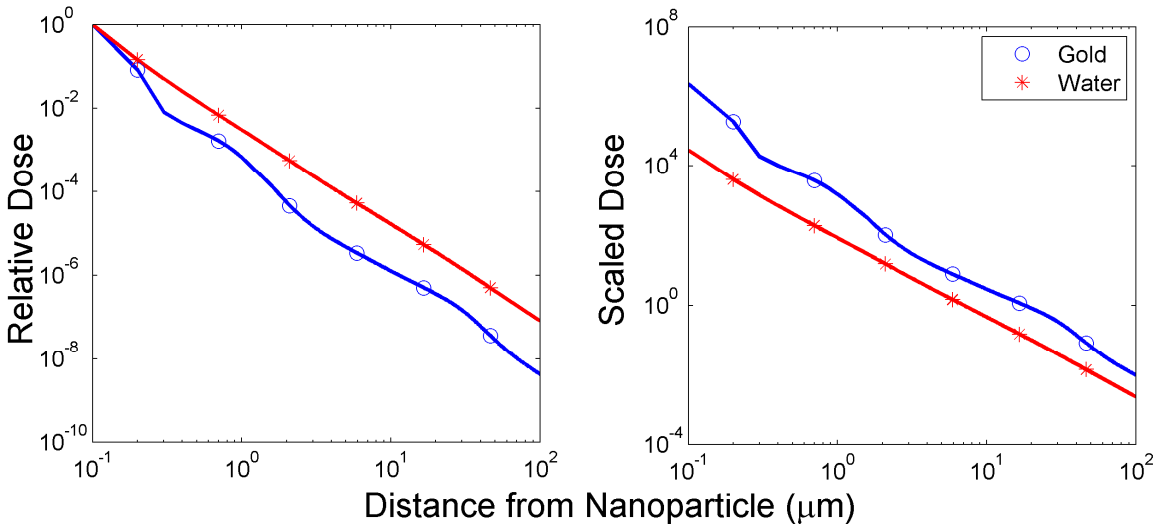

(a) (b)

Figure 2.3.8: **^{192}Ir** - (a) Relative Dose Point Kernels and (b) Scaled Dose Point Kernels in a water medium for a gold nanoparticle and a hypothetical water nanoparticle under irradiation by ^{192}Ir.

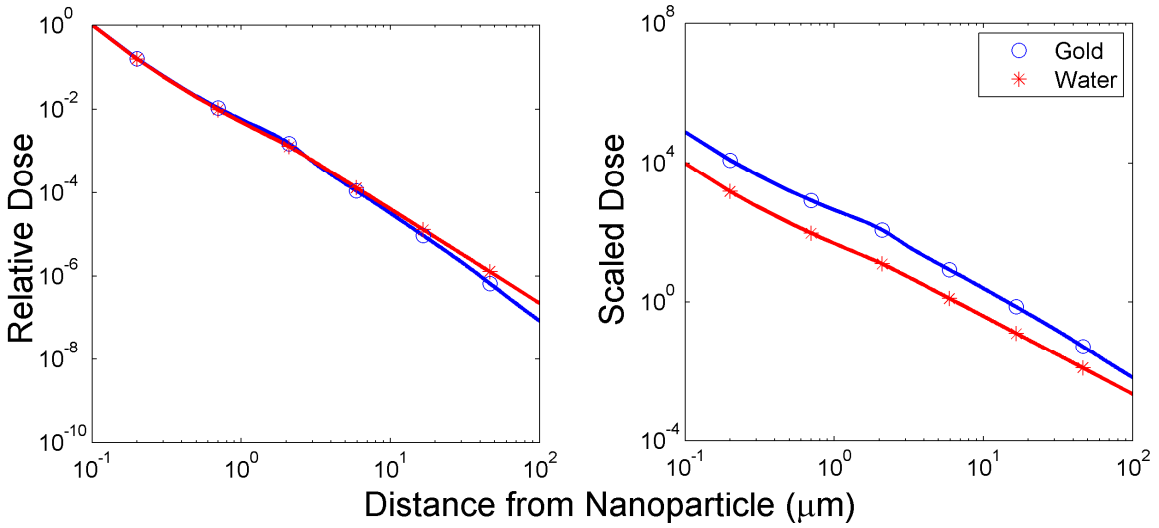

(a) (b)

Figure 2.3.9: **6 MV** - (a) Relative Dose Point Kernels and (b) Scaled Dose Point Kernels in a water medium for a gold nanoparticle and a hypothetical water nanoparticle under irradiation by 6 MV.

The microscopic dose enhancement factor (mDEF) is graphically shown in Figures 2.3.10. These values are only shown out to a radial distance of 100 μm, as the energy deposition beyond that distance is negligible. As expected, the mDEF in the area immediately surrounding the GNP is quite large, being at least 80 for all cases apart from the 6 MV source, which had mDEF values ranging from 1.4-9.8. As shown in Figure 2.3.11, the effects of a lower energy source spectrum are again evident, as the ^{125}I, 50 kVp, ^{103}Pd, and ^{169}Yb spectra show a two order of magnitude mDEF over short distances. The intermediate energy source, ^{169}Yb (Figure 2.3.12), has mDEF values exceeding 100 at a greater range from the GNP location. The high energy sources, ^{192}Ir and 6 MV (Figure 2.3.13) show little mDEF.

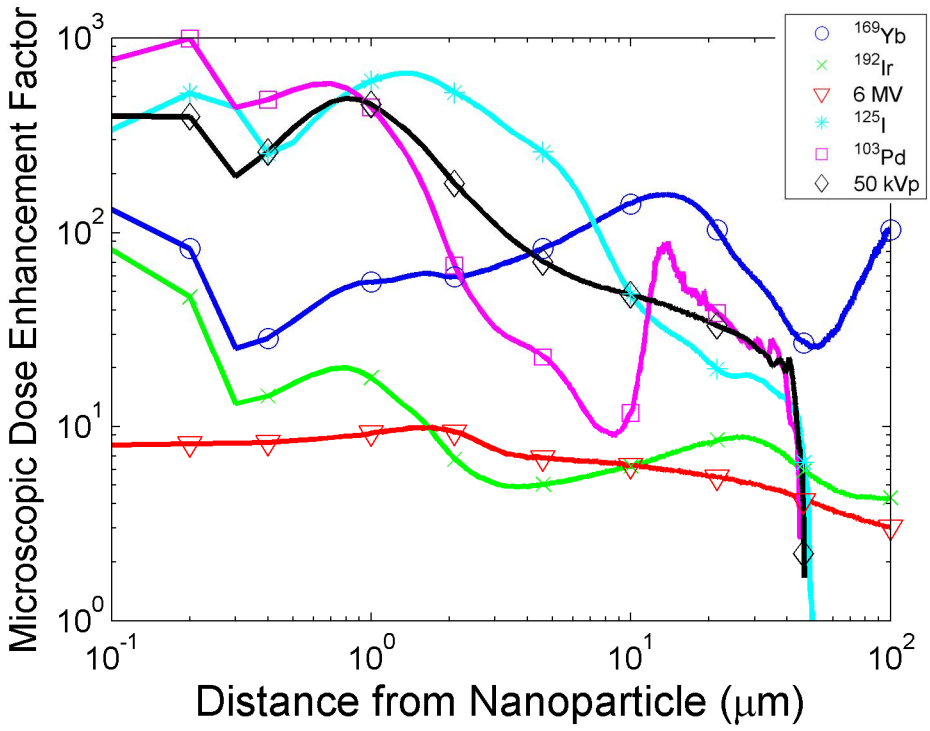

Figure 2.3.10: Microscopic dose enhancement factor (mDEF) obtained by taking the ratio between the scaled kernels for gold and water at a given distance.

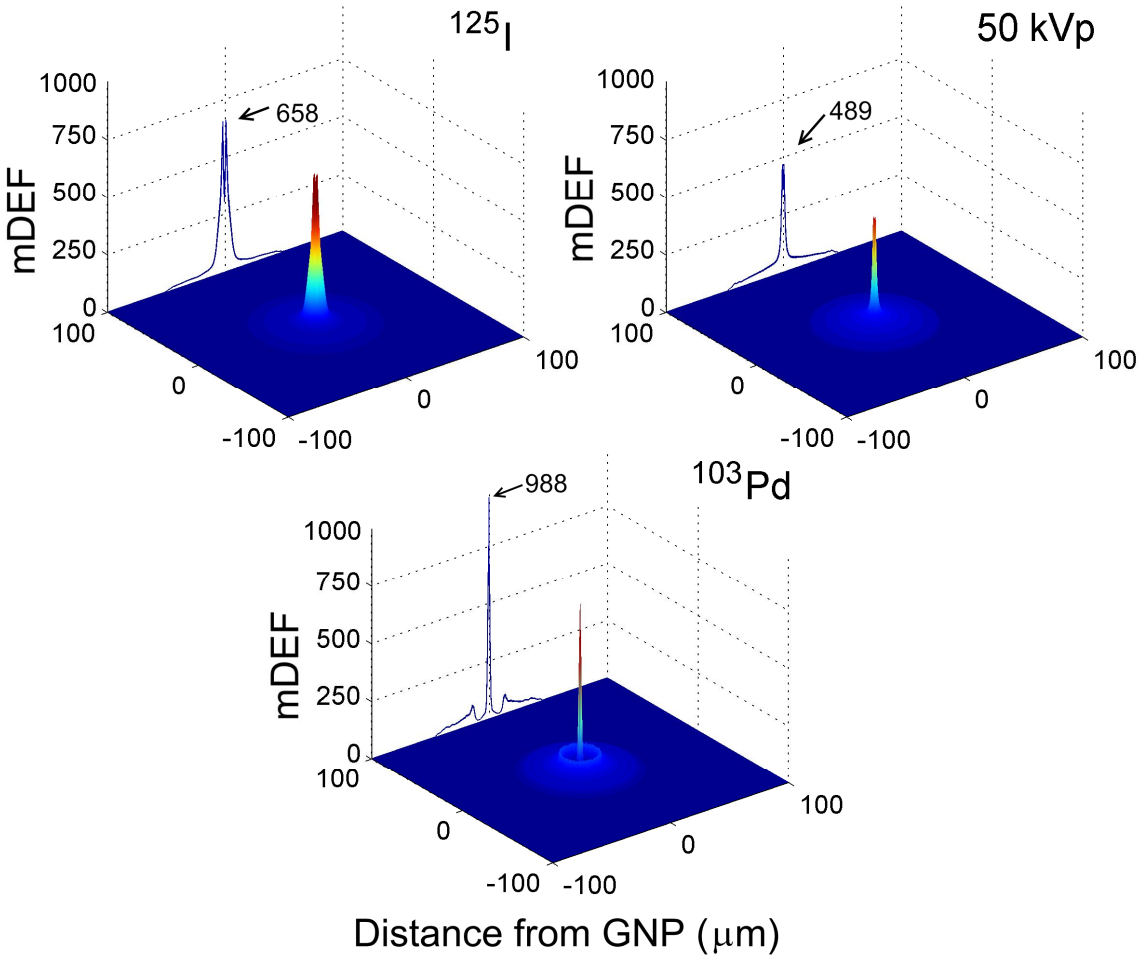

Figure 2.3.11: Low Energy mDEF - Spatial variation of microscopic Dose Enhancement Factor (mDEF) around a GNP. mDEF represents the factor by which that the dose would be increased by replacing that point with a GNP. The results are shown along the radial direction from a hypothetical GNP at the center. The value shown in each panel is the maximum mDEF for the given source.

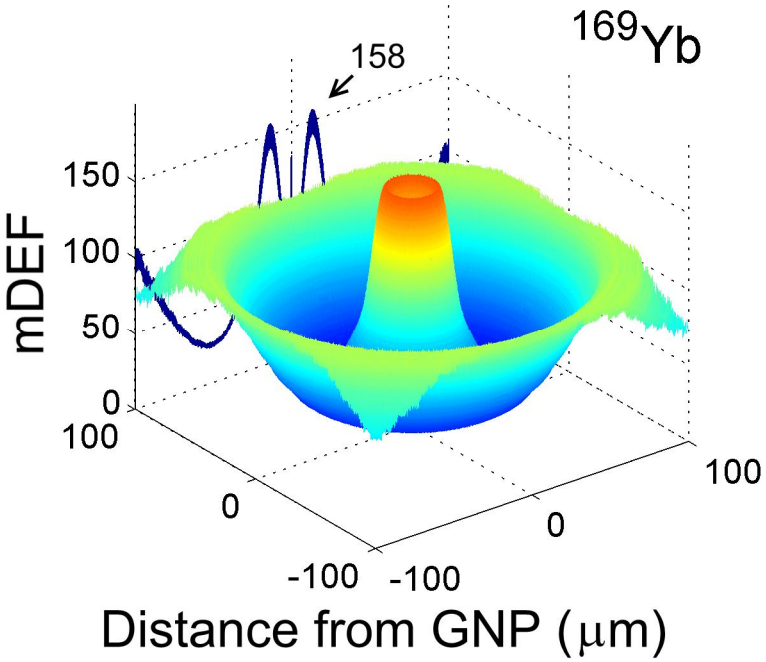

Figure 2.3.12: Intermediate Energy mDEF - Spatial variation of microscopic Dose Enhancement Factor (mDEF) around a GNP.

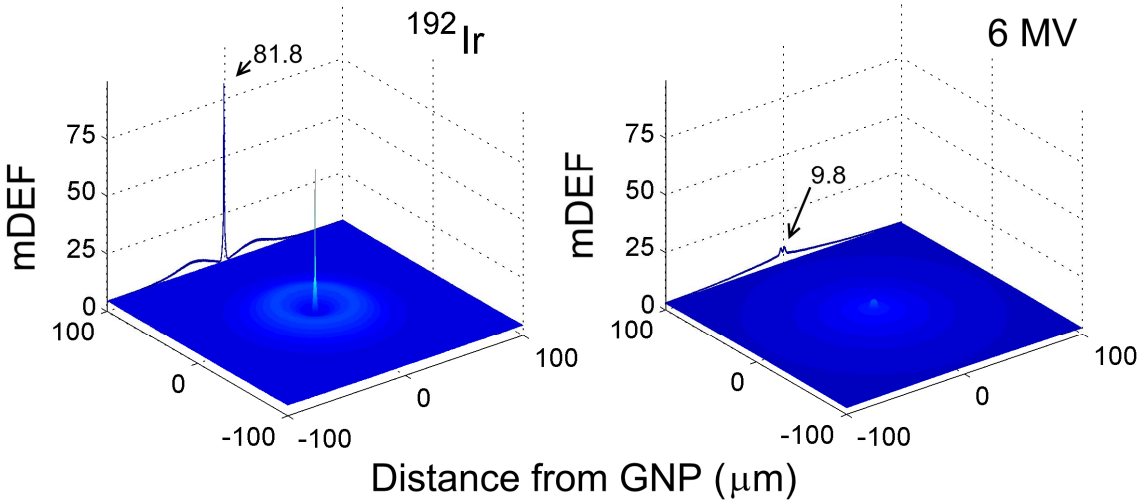

Figure 2.3.13: High Energy mDEF - Spatial variation of microscopic Dose Enhancement Factor (mDEF) around a GNP.

2.4 - Nanometer-Scale Dose Calculations

To further understand the phenomenon of dose enhancement in GNRT, the dose kernel of secondary electrons from GNPs was calculated on a nanometer scale using Monte Carlo methods. It can be seen in Figure 2.3.2 that, even within 1 μm from the GNP, the dose kernel exhibits a very steep gradient. Furthermore, nanoparticles anywhere from 2-100 nm in size may be applied to GNRT. The target of the radiation dose, DNA, has a width of only 2 nm. Thus, determining the dose kernel on a sub-micron level is necessary to fully characterize the dose enhancement process.

In order to calculate the dose on a nanometer-sized grid, several refinements must be made to the methods presented in Sections 2.2 and 2.3. First, the secondary spectrum must be recorded in much finer bins, since small changes in energy can have a ~1 nm change in the range of secondary electrons. Second, the energy cutoff for the secondary spectrum measurement must be lower than 1 keV, since these electrons can have a significant impact on the dose kernel under 1 μm. Third, these methods must be tested on a microscopy image of GNPs with a finer spatial resolution in order for the changes to be visible.

To that end, these computational methods were applied to the irradiation of a mouse using 250 kVp photons. The EGSnrc geometry was modified in order to replicate the treatment scenario; specifically, a 1x1x1 cm^3 gold-loaded region protruded from the front face of a 30x30x30 cm^3 water phantom. The gold-loaded region contained a mixture of water and gold (0.7 % Au by weight), and was irradiated by a 2x2 cm^2 250 kVp beam (50

cm SSD). The cutoff energy was lowered to 100 eV for photon and electrons, allowing the collection of very low energy auger electrons. The results of these simulations are shown in Figure 2.4.1.

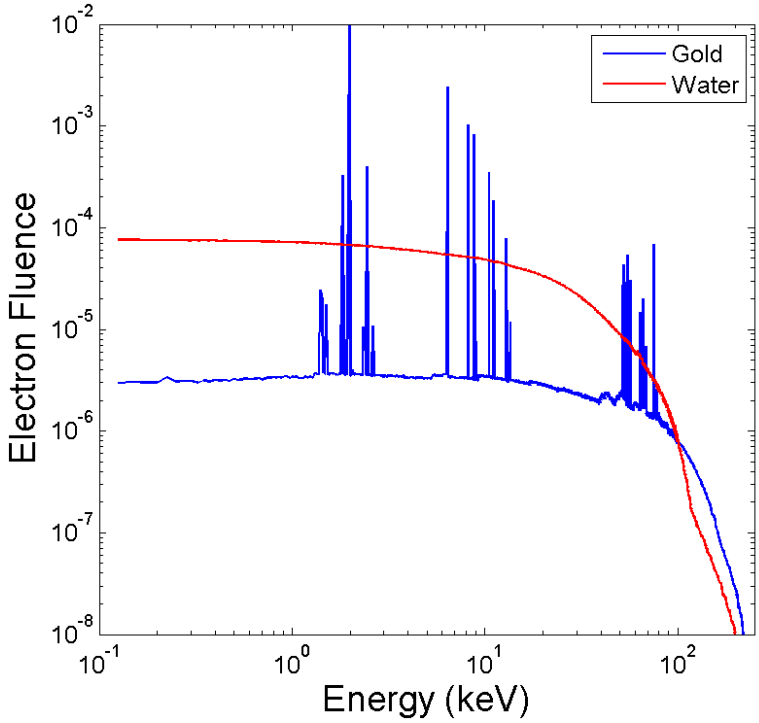

Figure 2.4.1: Secondary spectrum of electrons for 250 kVp photon source

The dose kernel of these secondary electrons was calculated using the event-by-event code NOREC, using the methodology described previously. In this simulation, the width of the dose collection shells was lowered to 1 nm in order to obtain a very fine resolution on the dose kernel. Since the short-range kernel was the focus of this investigation, the dose was only collected out to a maximum radial distance of 30 μm. From the secondary electron spectra, the gold/water dose scaling factor was calculated to be 54. This agrees well with expectations, as the scaling factors for ^{169}Yb and ^{192}Ir were 84 and 14,

respectively. The mDEF was calculated by taking the ratio of the scaled gold and water dose kernels. The dose kernels are shown in Figure 2.4.2, and the mDEF is shown in Figures 2.4.3 and 2.4.4.

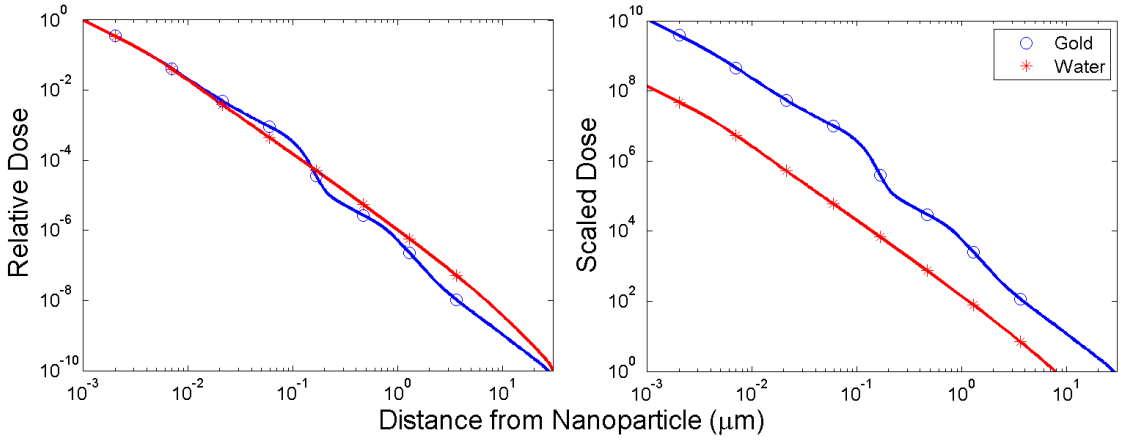

Figure 2.4.2: Relative and Scaled dose kernels for 250 kVp secondary electrons

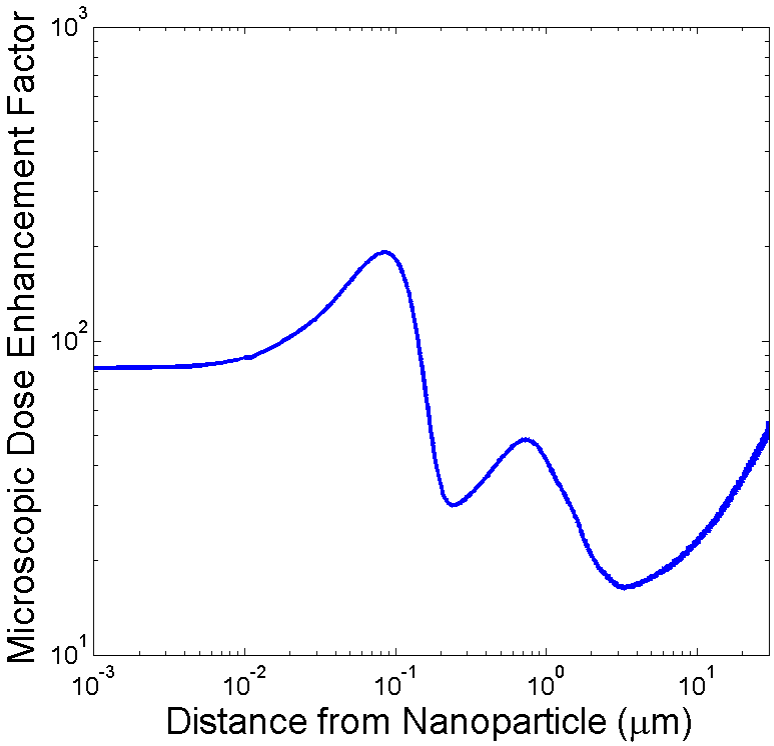

Figure 2.4.3: Microscopic Dose Enhancement Factor (mDEF) for 250 kVp secondary electrons.

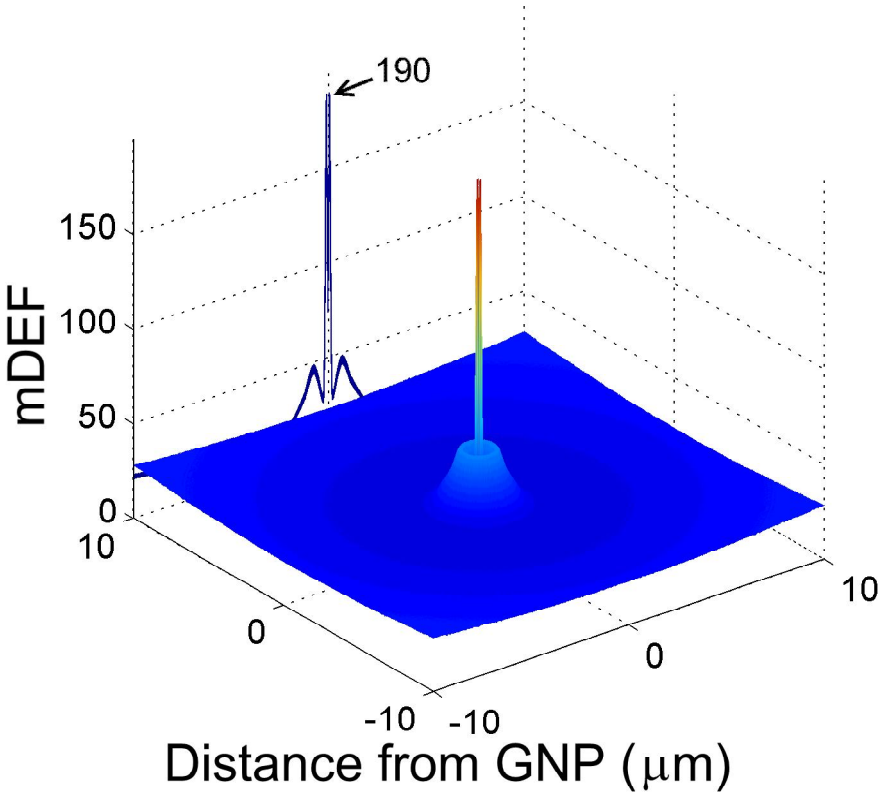

Figure 2.4.4: 250 kVp mDEF - Spatial variation of microscopic Dose Enhancement Factor (mDEF) around a GNP. mDEF represents the factor by which that the dose would be increased by replacing that point with a GNP. The results are shown along the radial direction from a hypothetical GNP at the center. The value shown in each panel is the maximum mDEF for the given source.

2.5 - Microscopic Dose Enhancement

To calculate the microscopic dose enhancement due to the presence of gold, the kernels were applied to a scanning electron microscopy (SEM) image of a GNP distribution in tissue.[30] Each pixel in the image was treated as a point source of either gold or water secondary electrons based on the intensity of that pixel, and with the dose point kernels, the radial dose distribution around each pixel was calculated. The dose enhancement calculation was performed in two steps under the assumption that the GNP distribution in three dimensions is similar to that of the two-dimensional image used. First, the water-

only dose was calculated for each pixel in the image by summing the dose contribution of every other pixel in the image using the dose kernel for water secondary electrons. In the second step, the dose contribution of each gold pixel in the image was found for every other pixel by adding the difference of the gold and water 2-D radial dose at that distance. Finally, the dose collected at each point was divided by the water-only dose to yield the factor by which the dose was enhanced at that point by the inclusion of GNPs. Note, during the current dose calculations, possible perturbation due to neighboring GNPs (i.e., screening effect) was not taken into account. This effect could be pronounced if GNPs are severely clustered within tissue and, may need to be investigated in future studies.

The microscopic dose enhancement due to GNPs in the sample SEM image, defined as the ratio of dose deposited at each point between the gold and water cases, is shown in Figures 2.5.1-4 for the representative sources ^{169}Yb, 50 kVp, and 250 kVp. The results for ^{192}Ir, ^{103}Pd, ^{125}I, and 6 MV are shown in Appendix B. The 50 kVp and 250 kVp sources, which contained the strongest low-energy component, demonstrated a microscopic dose enhancement as high as 500-2000% within the tumor vasculature. One can also see that the 5% enhancement line extends roughly 10 μm from the nanoparticle clusters. A greater long-range effect was seen in the ^{169}Yb and 250 kV sources, where the 5% enhancement line extended upwards of 30 μm from the nanoparticle clusters, and the dose enhancement inside the vasculature exceeded 200%.

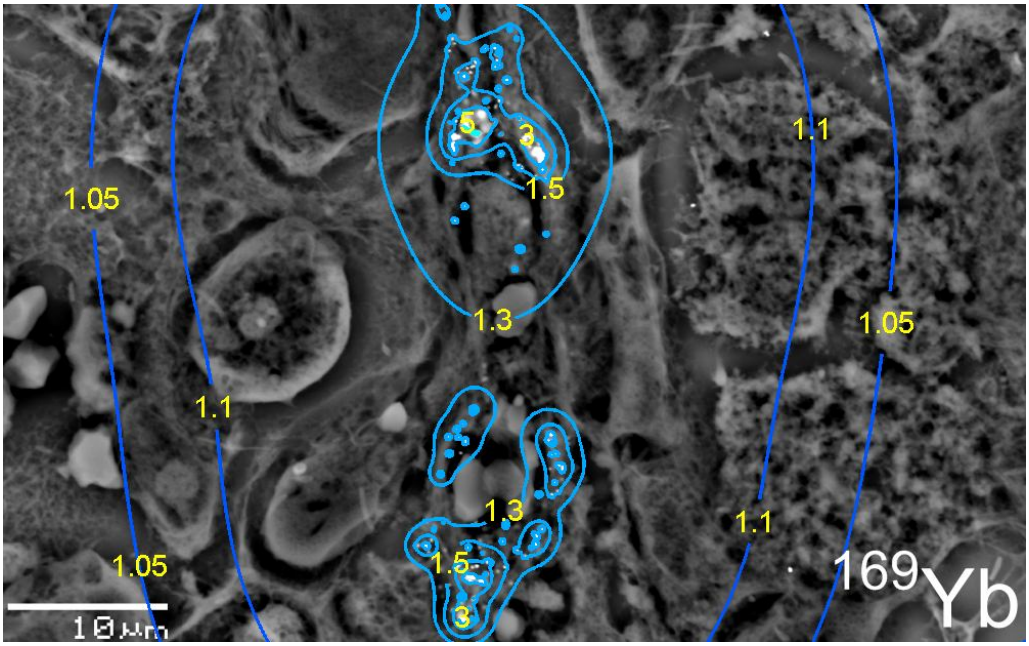

Figure 2.5.1: Microscopic Dose Enhancement from ^{169}Yb photon source for the specific GNP distribution *in vivo* obtained from the previous work.[32] 1.05, 1.10, and 2 represent 5%, 10%, and 100% enhancement, respectively.

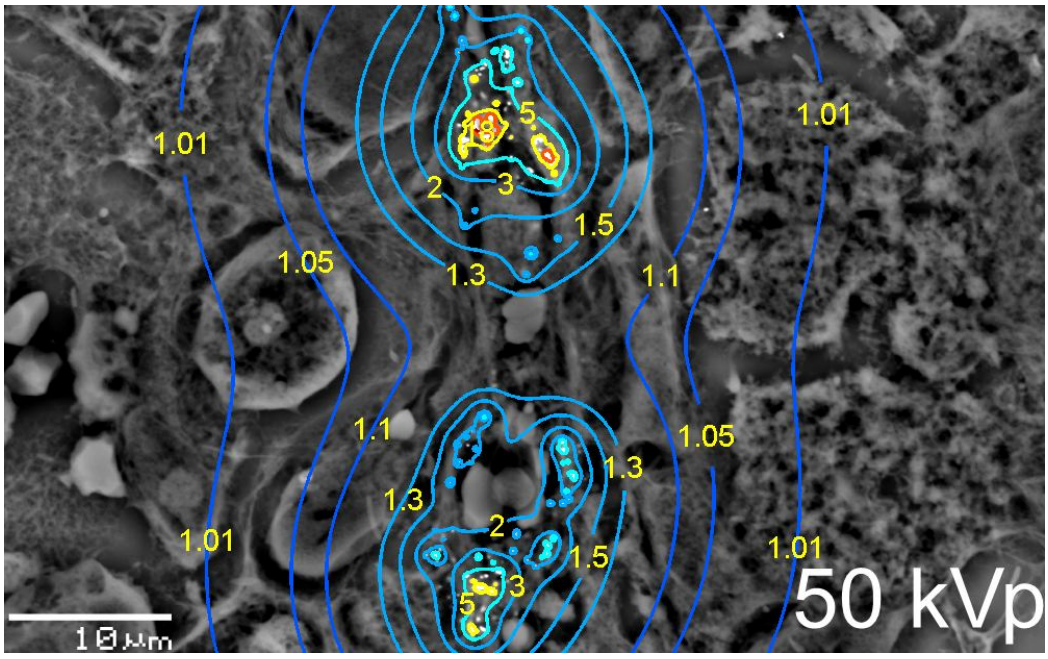

Figure 2.5.2: Microscopic Dose Enhancement from 50 kVp photon source for the specific GNP distribution *in vivo* obtained from the previous work.[32]

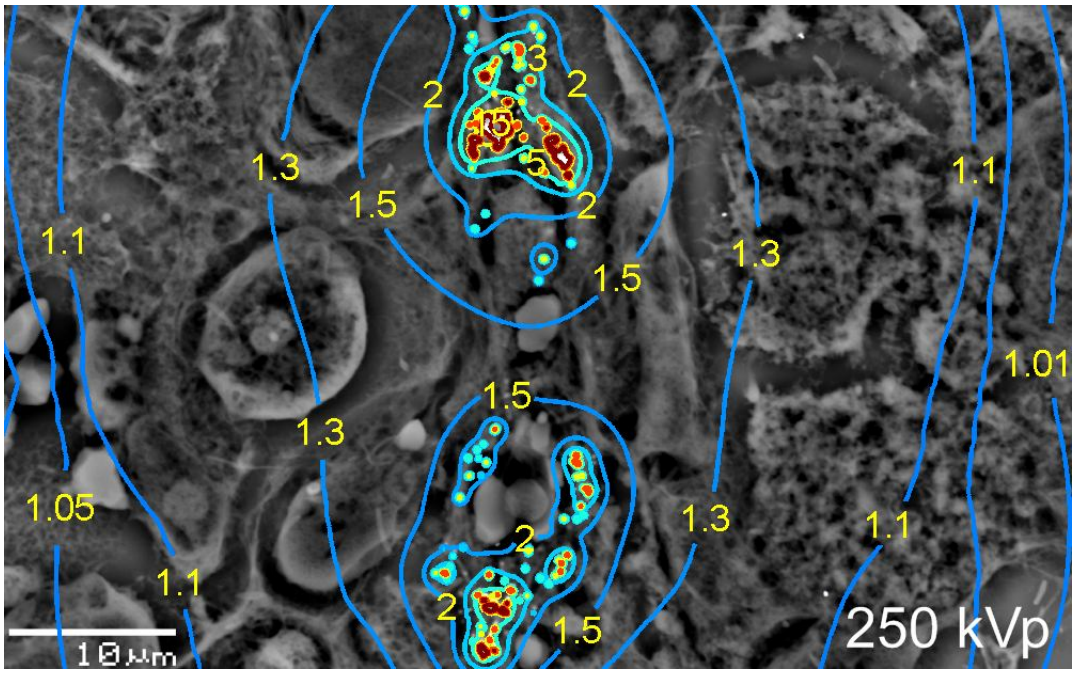

Figure 2.5.3: Microscopic Dose Enhancement from 250 kVp photon source for the specific GNP distribution *in vivo* obtained from the previous work.[32]

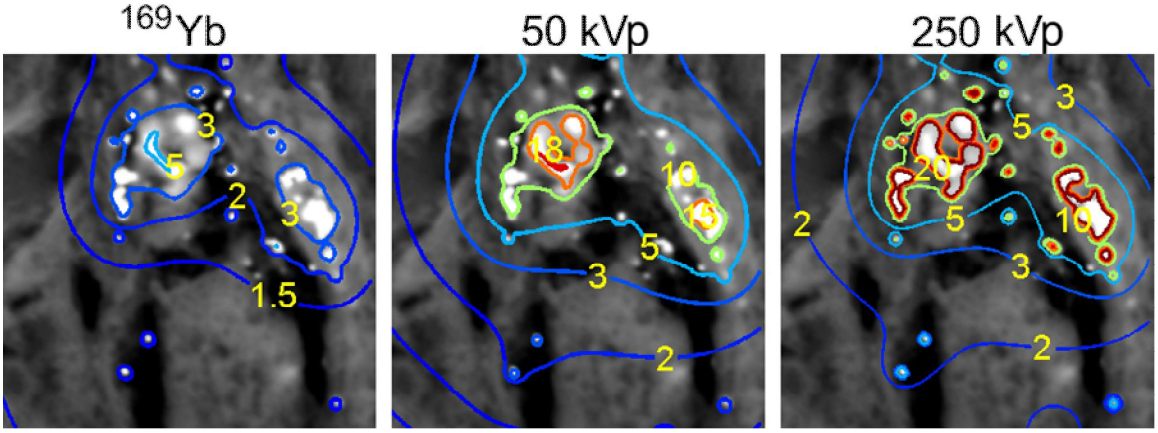

Figure 2.5.4: Microscopic Dose Enhancement from various photon source for the specific GNP distribution *in vivo* obtained from the previous work.[32] The dose enhancement is shown zoomed to the large GNP cluster in the upper part of Fig. 2.4.1-3

Note that, in Figure 2.5.4, the isodose lines were only shown up to a maximum of a factor of 20, since any enhancement above this occurred inside the GNPs, and these values were considered non-physical as the self-absorption of the gold is expected to be roughly 5% for a 250 kVp source.[50]

2.6 - Discussion

It has been shown previously that the macroscopic dose enhancement for ^{125}I, ^{169}Yb, and 50 kVp ranged from 50% to 100% at a uniform gold concentration of 7 mg Au/g tumor.[20] The current study demonstrates that the microscopic dose around a GNP is enhanced by factors up to more than 100, and the microscopic dose within a tumor is enhanced by over 100% over short distances for a test case based on a realistic (i.e., non-uniform) gold nanoparticle distribution in tissue. Although performed under somewhat different conditions, the current computational study strongly supports a finding from a previous experimental study with diagnostic x-rays that reported a similar level of dose enhancement (i.e., a factor of 100) on a cellular level due to the presence of gold (i.e. gold foil).[51] Moreover, it shows significant variation in microscopic dose enhancement between the different source cases. This variation could be exploited to allow for tailoring of the source to the spatial distribution of GNPs *in vivo*. For instance, ^{125}I or 50 kVp would result in large increases in the radiobiological effectiveness if GNPs can be brought within sufficient distance of the targeted cells. On the other hand, irradiation using a ^{169}Yb source leads to a meaningful dose increase over a larger distance, and could still be effective given a more heterogeneous spatial distribution of GNPs. The 250 kVp source shows even greater promise for microscopic dose enhancement. In Figures 2.5.3-4, the microscopic dose is enhanced by 10% at distances of 30-40 μm from the GNP clusters, and by over 2000% at sub-micron distances.

In general, it can be seen that there is very significant (>100%) dose enhancement with GNPs for a wide range of photon sources. However, it is seen that this extreme

enhancement is confined to the region within roughly 5 μm of the GNPs. Previous studies indicate that untargeted nanoparticles tend to remained trapped in the perivascular space within tumors, but targeted nanoparticles have the potential to penetrate the tumor interstitium and bind directly to tumor cells.[27] Given the short range of GNP secondary electrons, it can be expected that the maximum radiobiological benefit (killing of tumor cells) can be accomplished by bringing the GNPs as close as possible to the target of the radiation, DNA. It is also apparent that the radiobiological consequences of GNRT are most likely dependant on the GNP distribution and energy spectrum used to take advantage of the enhanced photoelectric cross section.

CHAPTER 3

MONTE CARLO STUDY OF CONE-BEAM POLYCHROMATIC XFCT

3.1 - Introduction

Tomographic reconstruction involves mathematically assembling a series of 1-Dimensional images (or projections) to form a 2-Dimensional image. This powerful tool allows one to examine the internal structure of an object without disturbing it. However, for this type of imaging, the irradiation geometry and image reconstruction problem are very closely related. Depending on the application, many different configurations are possible. X-Ray Fluorescence Computed Tomography (XFCT) is a stimulated emission tomography whereby the location and concentration of a high-Z substance is determined by measuring the signal of emitted fluorescence radiation.

Synchrotron XFCT

XFCT is traditionally performed using a pencil beam of monochromatic, synchrotron-generated x-rays in order to generate an image of the distribution of some substance in a small object.[52] The source spectrum is tailored to lie just above a photoelectric absorption edge of the element whose location inside the object is being interrogated to determine. The emitted fluorescence photons are detected by an uncollimated detector which lies outside the object; thus, each data point consists of the response along the path of the pencil beam. The beam (or object) is translated laterally so that the object is reasonably covered by these pencil beams, and this procedure is repeated as the object is

rotated. This setup is shown in Figure 3.1.1. The 1-D projections are formed for each projection angle by assembling the response of each pencil beam, and an image is tomographically reconstructed using either Fourier back-projection or iterative algebraic reconstruction.

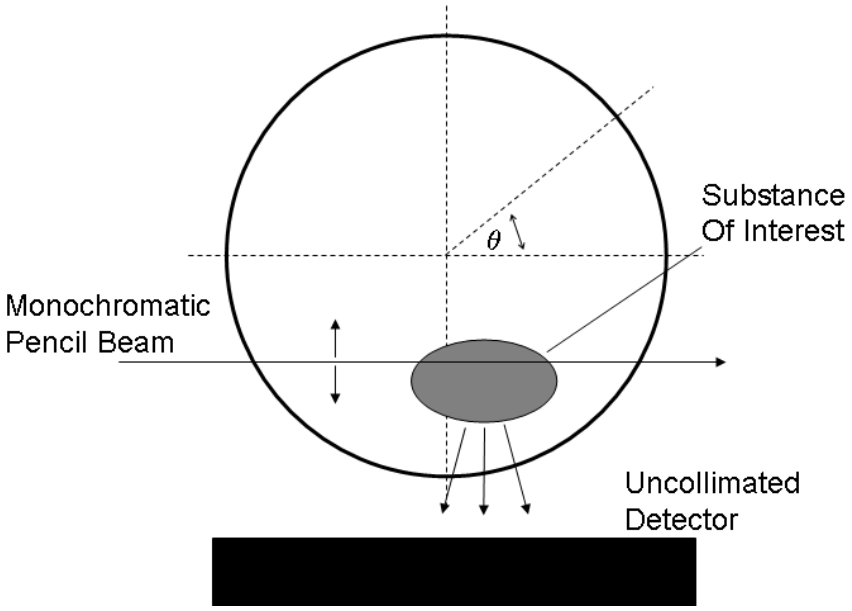

Figure 3.1.1: Imaging geometry for synchrotron-based XFCT. The fluorescence photons emitted by an object under irradiation by a monochromatic pencil beam are detected by an uncollimated detector. The pencil beam is translated through the phantom, and this process is repeated as the phantom is rotated.

The synchrotron-based approach to XFCT has several strengths. The monochromatic source allows the fluorescence signal to easily be extracted from the scatter background, making it possible to image very small concentrations of high-Z substances such as iodine or gadolinium. The resolution can be increased by using very small pencil beams. Also, the high dose rate source makes the time required for image acquisition small. The drawbacks of this method include the prohibitively high cost and poor availability of synchrotron beams. Also, the high dose rate makes imaging living objects a concern.

Polychromatic XFCT

An investigation was performed to determine the feasibility of using XFCT for human medical imaging, and the authors claimed that this technique would not be possible for large animals, given realistic constraints on dose and resolution.[53] However, it was shown that Gold Nanoparticle (GNP)-based benchtop XFCT for a 5-cm-diameter object was possible with a polychromatic pencil-beam source.[42] The image geometry was very similar to that shown in Figure 3.1.1; however, in order to deal with the increased Compton scatter due to the polychromatic source, the detector was collimated so as to have a restricted view within the phantom. The image acquisition process was repeated for five different lateral translations of the detectors, and the projection data was constructed by summing the detector response along the line of each pencil beam.

There are several problems with the polychromatic pencil beam XFCT scanning which make it impractical for *in-vivo* imaging. The process of translating both the pencil beam and the detector made the scans extremely long (~50 hours) and the dose delivered very high (2 Gy). Also, while the back-projection-based image reconstruction method produced an accurate image of GNP concentration/location, the details of its implementation make it impractical for imaging under variable geometries. Specifically, the attenuation correction was performed by manually calculating the path length of the pencil beam/fluorescence photons for each projection under conditions of known geometry.

The purpose of this Monte Carlo study was to optimize the image acquisition and reconstruction in order to improve image quality and decrease dose/scan time. To that end, a cone-beam-based system was developed. Under this imaging scenario, the entire phantom was irradiated by a broad beam of photons. Instead of using a detector with a wide view within the phantom, the detector was collimated to have a narrow view. Thus, spatial discrimination of the emitted fluorescence signal was not accomplished by restricting the size of the beam, but rather by the detector view. This allowed for parallel data acquisition and removed the geometrical requirement of translating the pencil beam through the phantom, but increased the amount of noise due to Compton scatter.

This study also sought to implement a better image reconstruction algorithm. A Maximum Likelihood (ML-EM) iterative reconstruction algorithm[54-56] was used, which allowed for better treatment of attenuation of both the primary beam and fluorescence photons. This also allowed for the gold location/concentration determined in an iteration to be used to update the attenuation correction of the next iteration.

3.2 - Monte Carlo Model

Imaging Geometry

To simulate XFCT scanning of a small animal-sized object by the Monte Carlo (MC) method, MCNP5[57] calculations of polychromatic irradiation of a 5-cm-diameter polymethyl methacrylate (PMMA) phantom were performed. The general imaging geometry is shown in Figure 3.2.1A. A cone beam of photons was incident on the phantom along the z-axis (or beam's central axis). The source of the cone beam was a

point source located 25 cm from the phantom. The spectrum of these photons is shown in Figure 3.2.2, and was taken from measurements of a 110 kVp Hamamatsu Micro-Focus X-ray source having been filtered by 680 μm of lead.[42] Note that, only photons above the *K*-edge of gold (80.7 keV) are able to create *K*-shell fluorescence, so the filtration is intended to reduce the fluence of photons below this level as they add only dose and noise.

The phantom was composed of PMMA, and was 5 cm in both height and diameter. The phantom contained several GNP-loaded regions, which were cylindrical in shape and ranged from 4 to 10 mm in diameter. The GNP-loaded columns were 3 cm high, and sat 2.5 cm deep in the phantom (leaving 0.5 cm extending from the top, as was the case in the pencil-beam XFCT study[42]). These columns contained a mixture of GNPs and water, with a gold concentration ranging from 0.1% to 2.0% Au by weight (or 1 mg to 20 mg Au per g water). These values were chosen to reflect possible concentrations of GNPs *in vivo*.[16]

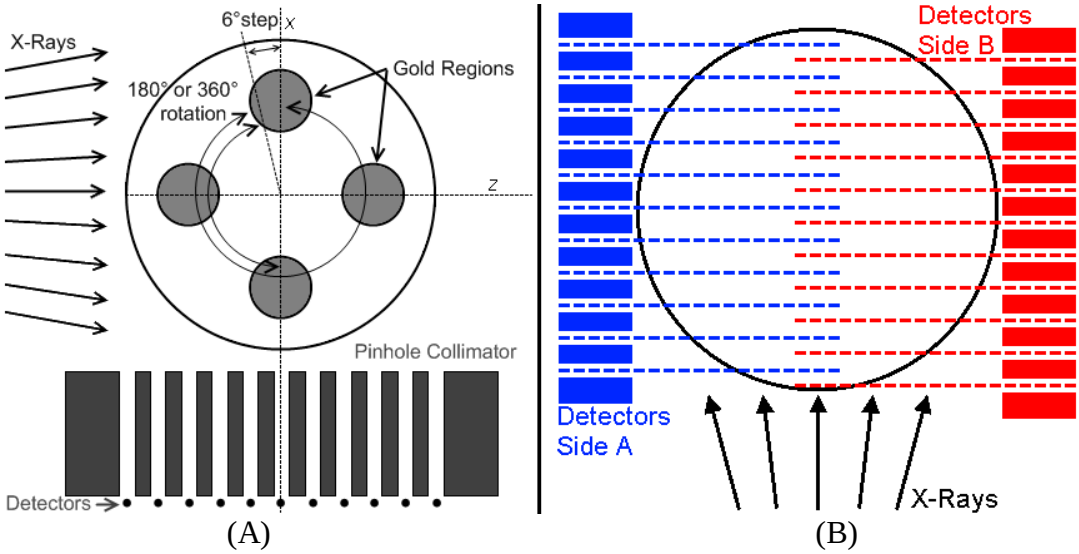

Figure 3.2.1: Schematic for Cone-beam Implementation of XFCT. (A) Geometry for Image Acquisition. The phantom is rotated in steps of 6°, with a full scan being composed of either 30 projections (180°) or 60 projections (360°). (B) Offset detector configuration. A second bank of detectors (Side B) is added to the opposite side of the phantom. The dotted lines indicate the view of each detector behind the parallel-hole collimator.

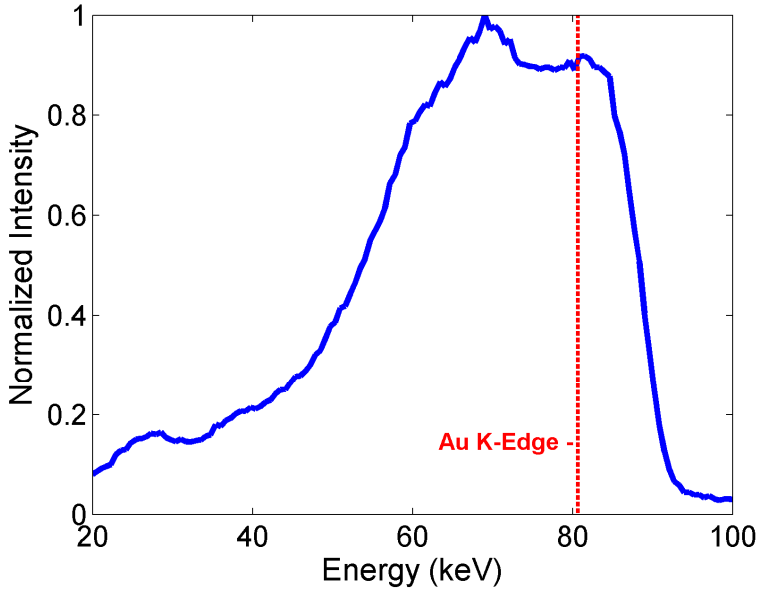

Figure 3.2.2: Filtered X-Ray Spectrum of Hamamatsu 110 kVp Microfocus X-ray Source

Data were acquired by a series of energy-sensitive tallies which are also shown in Figure 3.2.1A. They were positioned 1 mm behind a 4-cm-thick lead collimator with a series of parallel pinhole openings with a diameter of 2.5 mm. The phantom-to-collimator distance was 5 mm. By virtue of the parallel-hole collimation, each detector had a view inside the phantom along the x-axis at an angle of 90° relative to the beam central axis. Note that, in traditional synchrotron-based XFCT, spatial signal discrimination is accomplished by using a pencil beam, whereas in cone-beam XFCT spatial discrimination is accomplished using detector collimation. Thus the reconstruction problem resembles Single Photon Emission Tomography (SPECT). In order to improve detection efficiency and resolution while decreasing scanning time, a second set of detectors was added to the far side of the phantom. This configuration is shown in Figure 3.2.1B. Note that the second parallel-hole collimator is offset from the first in order to decrease the effective pixel pitch and increase resolution.

In order to simulate the XFCT scanning geometry, an independent simulation was performed for each projection angle. Additionally, an independent simulation was performed for each unique configuration of the imaging geometry, including varying the number of detectors (11, 17, or 25) or the position of the gold columns within the phantom. Each detector in the imaging setup was represented as a deterministic point detector tally (F5) with an exclusion radius of 5 mm. Each simulation was performed using 20 M histories, resulting in an uncertainty on the order of 5% for relevant energies (50-70 keV).

Data Analysis

At gold concentrations on the order of 0-2% Au by weight, the spectrum of photons arriving at the detectors is dominated by Compton Scatter. However, since Compton scatter creates a continuum of energies while atomic fluorescence occurs only at discrete energies, the gold fluorescence signal intensity can be extracted from the Compton background. Due to the attenuation of low energy photons in the phantom, it was not practical to use the gold *L*-shell fluorescence (~10 keV) for image reconstruction. The gold K_α lines (67.0 and 68.8 keV) are the best candidates for this type of imaging due to the decreased absorption at higher energies as well as the greater probability of K_α fluorescence emission compared to K_β fluorescence emission (~78 keV).

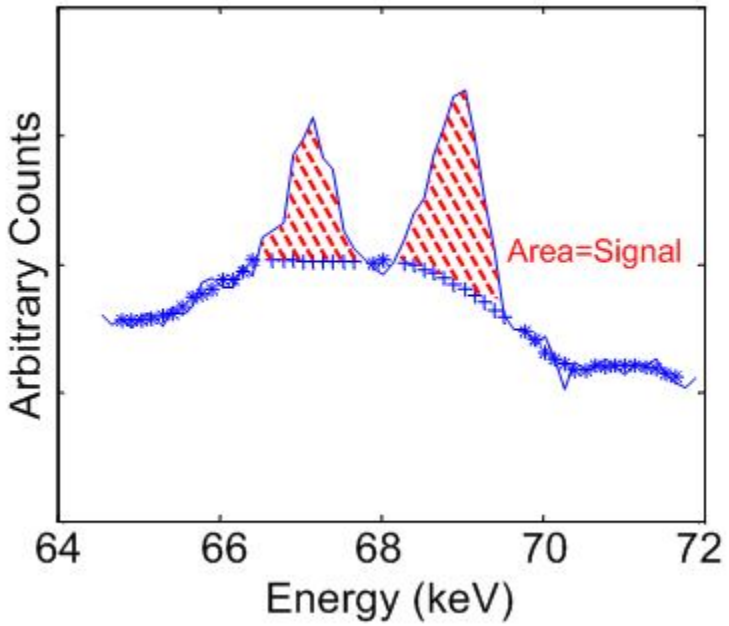

Figure 3.2.3: Extracting Gold fluorescence signal from Compton background. Solid line represents typical fluorescence spectrum when gold column containing 2% Au is in view of the detector. The area covered by the dashed lines is the signal for a particular detector and angle. (*) - 3rd degree polynomial fit of Compton background data. (+) - Interpolated Compton background in Au channels.

A portion of a sample spectrum acquired from a detector during one projection is shown in Figure 3.2.3. To extract the gold fluorescence peak height from the Compton background, a 3rd degree polynomial was fit to the points on either side of the gold fluorescence peaks. The gold fluorescence signal intensity at that detector for that projection angle was then given by the difference of the measured signal and the polynomial fit. By extracting the gold fluorescence signal intensity from each detector at each projection angle, a sinogram of the gold fluorescence signal intensity was constructed. More details about the gold fluorescence data acquisition and processing can be found elsewhere.[42]

3.3 - Image Reconstruction

Using the sinograms created during the data acquisition, an image of the gold distribution inside the phantom was reconstructed by applying a Maximum Likelihood (ML-EM) iterative reconstruction algorithm.[54-56] Given the projection dataset p described by the measured sinograms, and some initial guess of the intensity in each pixel a, one must construct the matrix M, where each element $M_{i,j}$ is the probability that a fluorescence photon will be created at the pixel a_i and detected in the projection element p_j. This relationship is described in Eq. (3.3.1), and the operating equation for computing the next iteration of the image is described in Eq. (3.3.2).

$$p_j = \sum_i M_{i,j} a_i \tag{3.3.1}$$

$$a_i^{k+1} = \frac{a_i^k}{\sum_j M_{i,j}} \times \sum_j M_{i,j} \frac{p_j}{\sum_i M_{i,j} a_i^k} \tag{3.3.2}$$

The construction of the attenuation matrix M was accomplished by considering four factors which influence the photon emission and detection probability: attenuation of the primary beam as it passes through the phantom, attenuation of emitted gold fluorescence photons by the phantom, attenuation of emitted gold fluorescence photons by other GNP-loaded regions, and the $1/r^2$ dependence of the fluence of gold fluorescence photons from an isotropic source (i.e., GNP).

Consider the geometry shown in Fig. 3.3.1. To construct the attenuation matrix M, it is necessary to determine the probability that, for a beamlet entering the phantom at point A, a fluorescence photon will be emitted at point B and detected at point D. The attenuation of the primary beam as it travels from point A to B, P_1, is given by Eq. (3.3.3). Also, the probability that the emitted fluorescence photon reaches the detector, P_2, is given by Eq. (3.3.4). Note that the attenuation coefficient $\mu(r)$ is a function of position within the phantom in order to take into consideration changes in gold concentration along the intended path. It also varies with energy and geometry; μ_{beam} is given by broad beam attenuation of those source photons (~85 keV) which can cause gold K-shell fluorescence, while μ_{gold} is given by narrow beam attenuation of gold K_α photons. Although each attenuation coefficient in this study was taken as *a priori*

knowledge, it can be determined during the realistic XFCT scanning by employing a transmission detector that produces an attenuation map of the imaged object. After each iteration of the reconstruction algorithm, the μ(r) value was updated for each point in the phantom by using the current map of the gold concentration. This was used to update the attenuation matrix M.

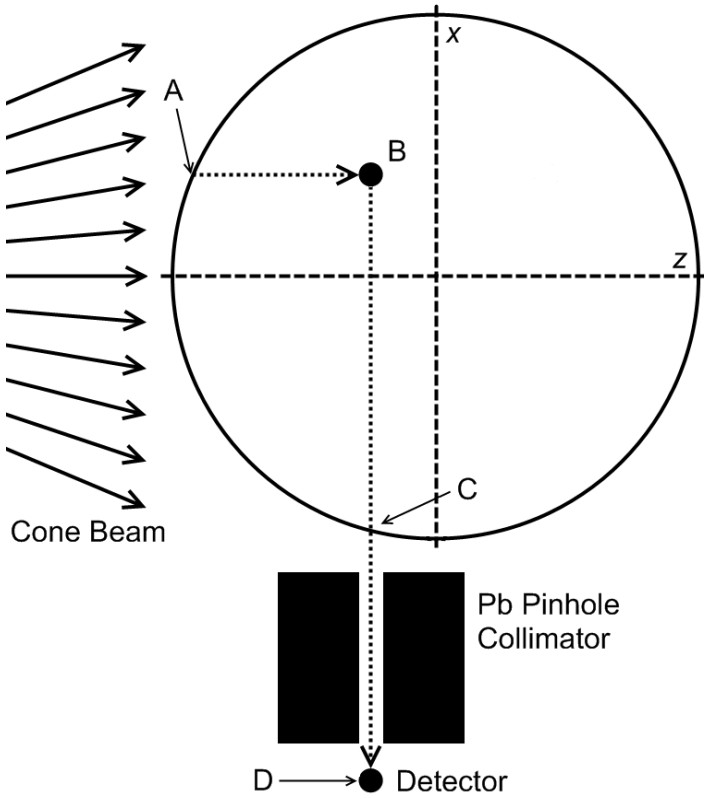

Figure 3.3.1: Geometry for Attenuation Correction. It is necessary to determine the probability that, for an arbitrary point B within the phantom, a fluorescence event is induced by an external x-ray irradiation from the source (enetering the phantom at Point A), and the fluorescence photon reaches the detector (point D). The complete attenuation correction matrix is constructed by iterating Eqs. (3) and (4) over all points (B) in the phantom and all detectors (D).

$$P_1 = \exp\left(-\int_A^B \mu_{beam}(z)dz\right) \tag{3.3.3}$$

$$P_2 = \frac{\exp\left(-\int_B^C \mu_{gold}(x)dx\right)}{\left|\overline{BD}\right|^2} \tag{3.3.4}$$

One well-known problem in iterative reconstruction for emission tomography is the tendency of image noise to increase if the number of iterations performed becomes large [58]. For SPECT, it has been shown that the optimal solution for this problem is to apply a smoothing filter after each iteration to decrease noise.[59] In the case of XFCT, an edge-preserving Gaussian filter[60] was applied.

To test the performance of cone-beam XFCT scanning, images were reconstructed using MC data obtained under several different conditions. MC data were acquired with either a single bank of detectors on one side, or two banks of detectors on both sides (1-sided or 2-sided scan). The number of detectors in each bank was 11, 17, or 25. 60 projections covering the full 360° of phantom rotation were used during the MC data acquisition; however, by ignoring the latter 30 projections, an image can be reconstructed representing a 180° scan. Finally, these data were acquired for three different gold/phantom configurations.

3.4 - Imaging Results and Imaging Metrics

In order to make a comparison with the results of the existing bench-top pencil-beam XFCT scans,[42] several scans under the current cone-beam geometry were simulated with

17 detectors in each bank. The results of these scans for all three phantoms are shown in Fig. 3.4.1. The first phantom contained three GNP-loaded columns of diameter 1 cm, each at a constant radial position relative to the center of the phantom and with gold concentrations of 0.5, 1.0, and 2.0% Au by weight. This phantom was very similar to the phantom used in previous pencil beam scanning, and showed similar results. The gold concentration varied quite linearly with signal intensity. In the second phantom, five GNP-loaded columns of diameter 8 mm were placed in a line across the center of the phantom in order to test the attenuation corrections for both radial depth and increased self-absorption by GNP-loaded regions. This would constitute a "worst-case" scenario for the reconstruction of XFCT images. One can see that there was some blurring of the location of GNP-loaded regions, and the signal intensity was not as linear with gold concentration. However, the lowest concentration (0.1% Au by weight) was still visible. In the third "spiral" phantom, eight gold columns of diameter 5mm ranging from 2.0% to 0.25% Au by weight spiraled radially outwards from the center. In this case, the GNP-loaded locations were well-determined, and signal response was very linear.

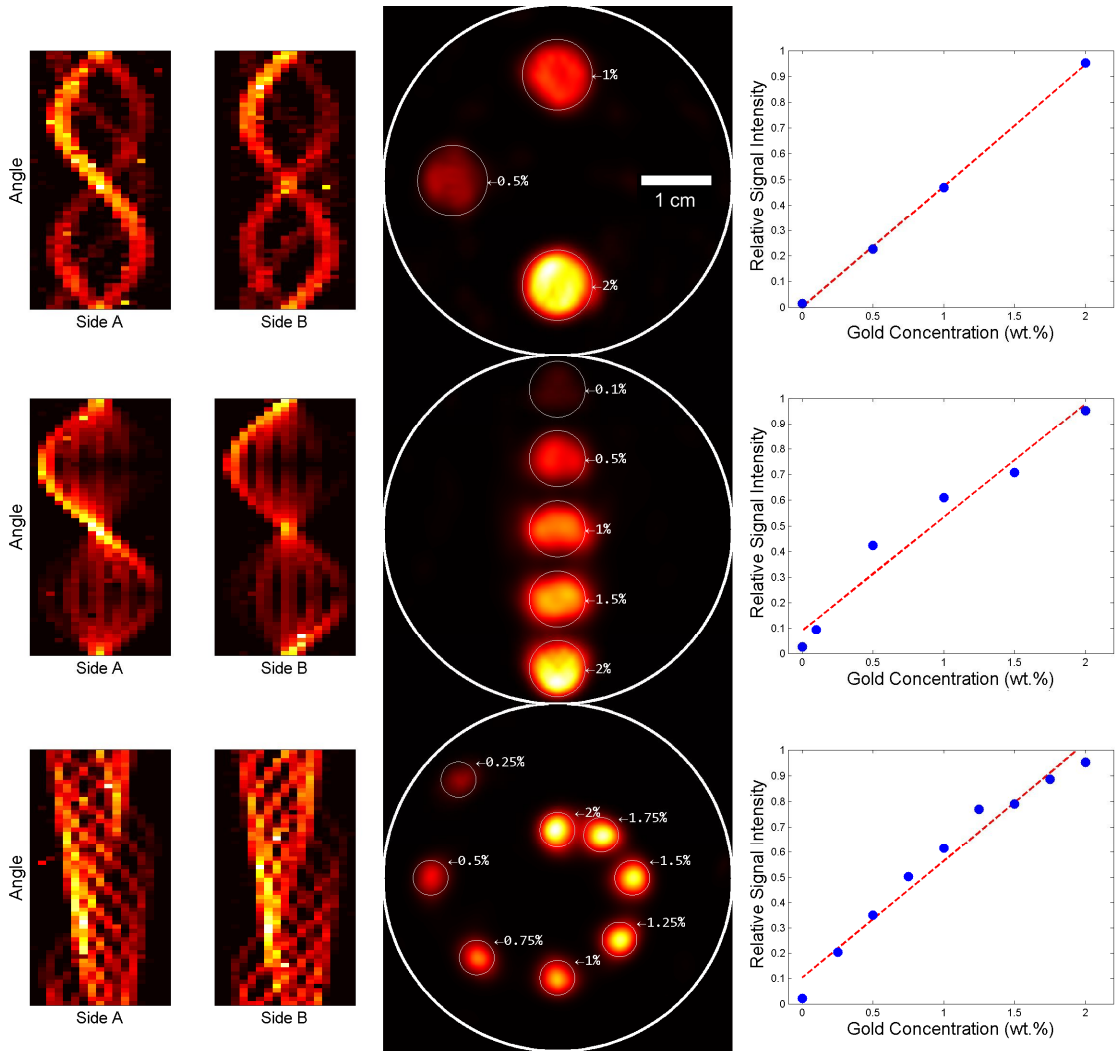

Figure 3.4.1: Reconstructed images for the three phantoms considered. Each phantom is labeled with the gold concentration (by weight) of each GNP-loaded column included. The right-side panels show the linear relationship between gold concentration and average signal intensity in each column. Results are shown for the XFCT setup with 360° data acquisition, 2-sided, 17 detectors.

In Fig. 3.4.2, the results of XFCT imaging using 11, 17, and 25 detectors are shown for the "spiral" phantom. The resolution of the image increases with more detectors; however, there seems to be diminishing returns by using more than 17 detectors. The distance between the two central columns (2% and 1.75%) is 1.3 mm, and it can be seen that those columns are resolved using 17 or more detectors.

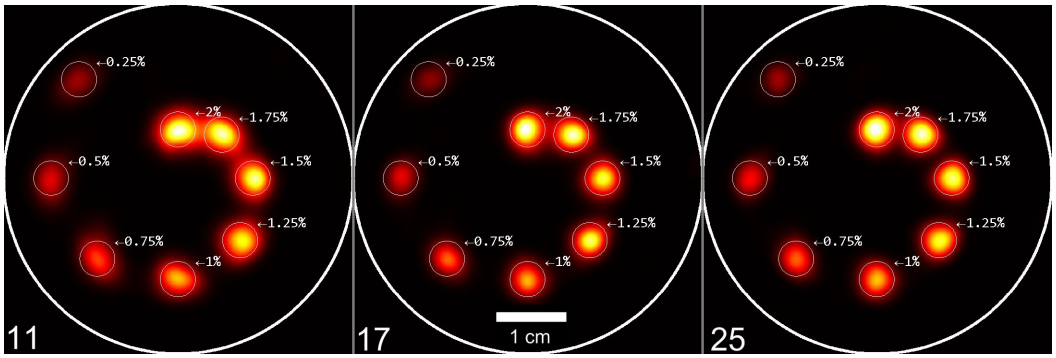

Figure 3.4.2: Reconstructed images for spiral phantom (see also Fig. 3.3.1) with 11, 17, and 25 detectors. As the number of detectors increases, spatial resolution improves. Results are shown for the XFCT setup with 360° data acquisition, 2-sided.

Fig. 3.4.3 compares the results of imaging the spiral phantom with limited information. Results are shown for scans using 25 detectors in each bank, and images are reconstructed using either one or both banks (one-sided or two-sided). Additionally, results are shown for images reconstructed using 60 projections (360°) to 30 projections (180°). Fig. 3.4.3(a) shows the relative error, which is defined as the sum of the squared difference of each pixel value in the image with the expected value. Fig. 3.4.3 (b) shows the coefficient of determination (R^2) for the linear fit of the gold concentration measured in each column (see Fig. 3.4.1). As expected, the image quality increases as more information is used in the reconstruction. The error decreases as the number of projections increase, and the calibration curve of gold concentration becomes much more accurate. It can also be seen that the two-sided scans perform much better than one-sided. Reducing the number of projections to 30 would decrease the overall scan time and dose by a factor of two, but reducing the number of detector banks to one would decrease the overall cost of an eventual bench-top XFCT scanner. Finally, it can be

noted that above 45 projections (270°), there seems to be diminishing returns in terms of image quality gained with increasing dose.

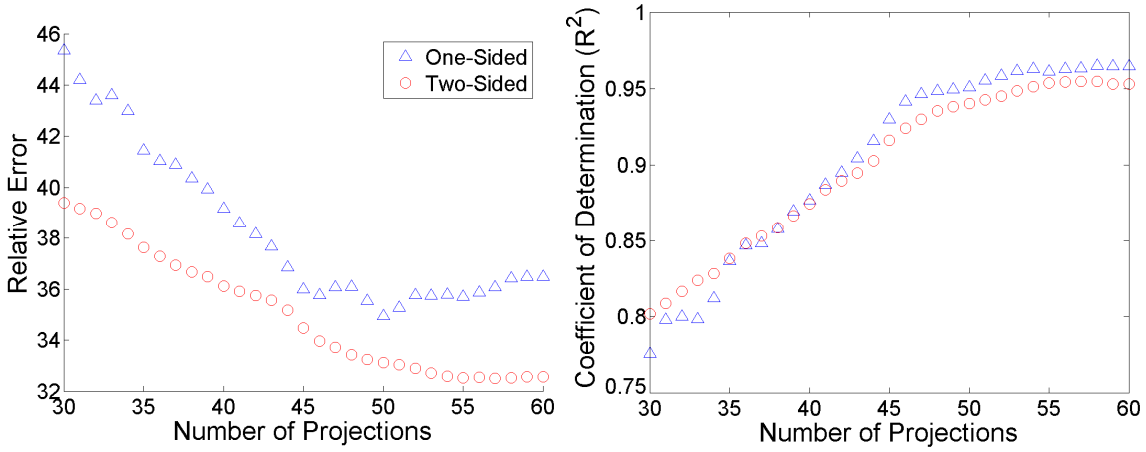

Figure 3.4.3: Imaging metrics for the "spiral" phantom with 25 detectors. Results are shown as the number of projections increases from 30 to 60, corresponding to 180°-360° imaging. Panel (a) shows the relative error, which is defined as the sum of the squared difference of each pixel value in the image with the expected value. Panel (b) shows the coefficient of determination (R^2) for the linear fit of the gold concentration measured in each column.

3.5 - Discussion

The feasibility of a polychromatic cone-beam XFCT device described in this MC study may not be fully established without a successful demonstration by an experimental study. Nevertheless, the current MC results may provide valuable insight into possible design and technical specifications associated with such a device. According to the current results, a cone-beam implementation of polychromatic XFCT would result in a significant reduction of overall scanning time, compared to the pencil-beam implementation described in a previous study.[42] It can be immediately noticeable there would be an almost 10 fold reduction in scanning time as a result of a cone-beam implementation, provided that the data acquisition time per projection during the cone-

beam XFCT scanning remains the same as that (i.e., 60 seconds) used during the previous pencil-beam work. This implies if the XFCT scanning of the phantom used in the pencil-beam study was repeated with the current cone-beam XFCT setup, the total scanning time could be less than an hour, which may be considered acceptable for *in-vivo* imaging.

While the current MC results may provide an encouraging outlook for a drastic reduction of scanning time, it appears to remain as a technical challenge whether or not the detection limit for gold concentration could be lowered below 0.1% by weight or even more perhaps on the order of part per million. The current MC simulations in conjunction with deterministic tallies were believed to have yielded less noisy fluorescence signals than realistic experiments. Therefore, the detection limit shown in this study (i.e., 0.1% Au by weight) could be considered as the best theoretically possible value achievable from the current polychromatic cone-beam XFCT setup. Similar to previous arguments,[42] the detection limit might be reduced further by a few additional modifications to the current setup such as further tailoring/quasi-monochromatization of incident x-ray spectrum, use of novel fluorescence peak selection algorithm, and further optimization of detector collimation. These modifications would also help improve the resolution of XFCT images. Note the current MC results indicate an XFCT image resolution on the order of 1 mm could be achievable, which is comparable to or slightly better than that available from currently available emission tomography devices such as micro-PET or micro-SPECT.

CHAPTER 4

EXPERIMENTAL STUDY OF CONE-BEAM POLYCHROMATIC XFCT

4.1 – Cone-beam Polychromatic XFCT - Experimental Setup and Image Acquisition

Imaging Phantom and X-ray Beam

In order to test a realistic small-animal XFCT scenario, samples containing gold nanoparticles (GNPs) were prepared which correlate with realistic tumor/blood gold concentrations achievable *in vivo*: namely, 2.0%, 1.0%, and 0.5% gold by weight.[16] Roughly cylindrical tubes of height 2 cm and diameter 6 mm were filled with saline solution, and commercially available GNPs of diameter 1.9 mm (Aurovist™, Nanoprobes Inc) were added. In total, the tubes contained 6.5 mg, 3.3 mg, and 1.6 mg of GNPs, respectively. The GNP-loaded tubes were then inserted into a cylindrical phantom 3 cm in diameter and 5 cm in height. The phantom was composed of polymethyl methacrylate (PMMA). The three tubes were located 9 mm from the center of the phantom, and spaced at 120º intervals. This geometry is shown in Figure 4.1.1.

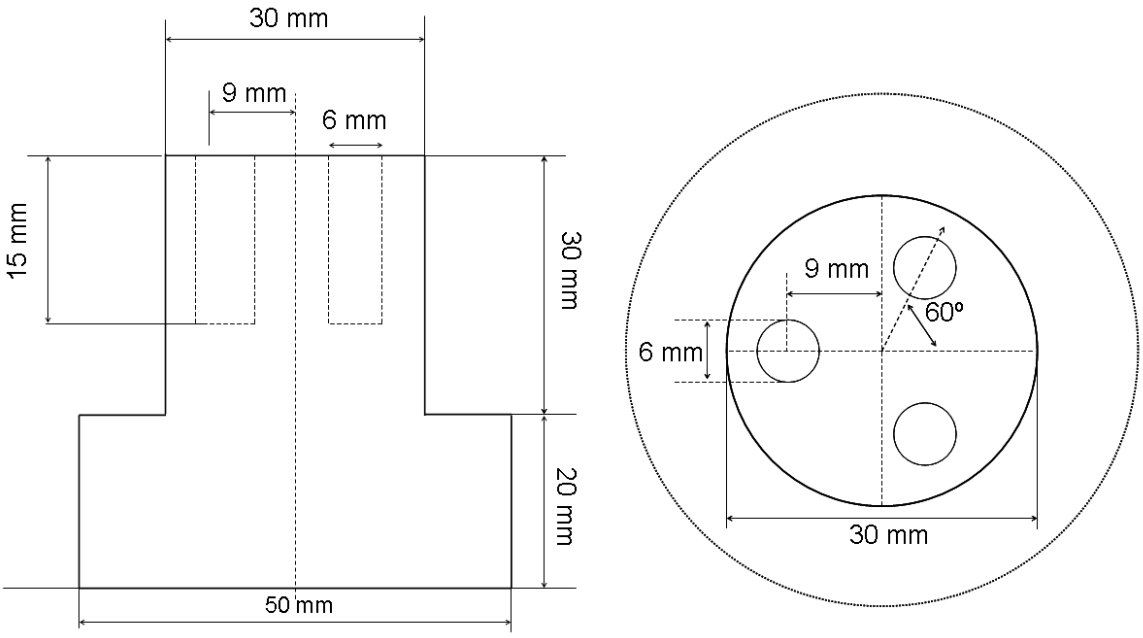

(a) (b)

Figure 4.1.1: Imaging Phantom. The PMMA phantom is shown from the side (a) and top (b).

To acquire images of the GNP location/concentration, the phantom was irradiated with a 110 kVp microfocus x-ray source (L9631, Hamamatsu Photonics, Inc) operating at 400 μA. The source had a focal spot size less than 100 μm and an emission angle of 62º. The beam was collimated by a conical hole through a lead block 5 cm thick. The angle of the conical hole was 11.4º, with front/back hole diameters of 1 and 2 cm. The center of the phantom was roughly 8 cm from the collimator surface (14.5 cm from exit window of source), yielding a beam whose diameter just exceeded the 3 cm phantom diameter.

Although the nominal maximum tube voltage was 110 kVp, the x-ray tube was operated at 105 kVp in order to increase beam stability over the entire course of the irradiation. The beam was filtered by 1.0 mm of lead, yielding the beam spectrum shown in Figure

4.1.2. The filter thickness must be chosen carefully in order to a) reduce image dose, b) maximize photon fraction over the *K*-edge of gold (80.7 keV), and c) retain as much fluence rate as possible in order to minimize scan time.

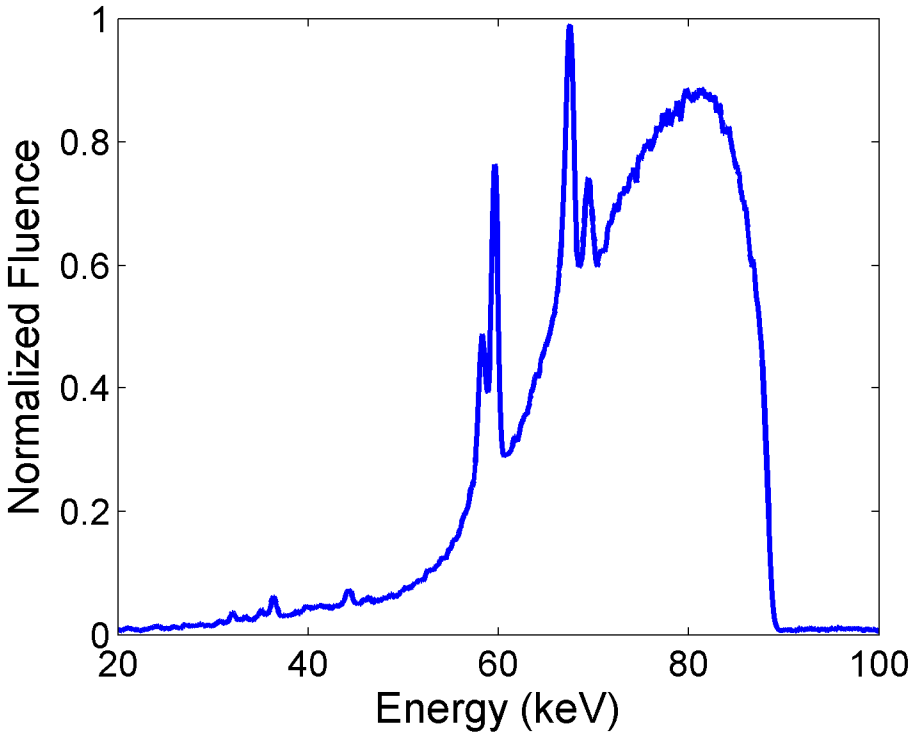

Figure 4.1.2: Filtered Beam Spectrum

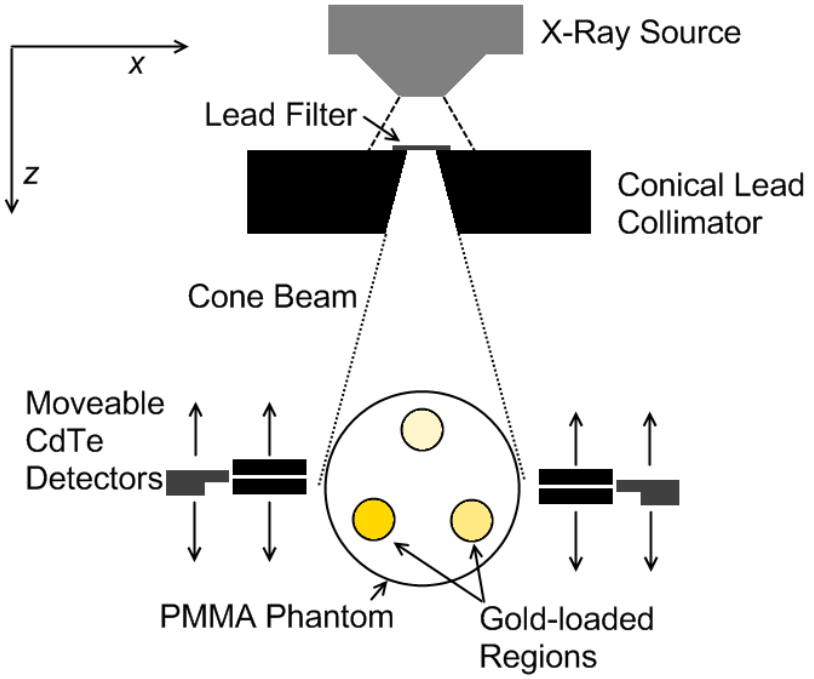

Figure 4.1.3: Image Acquisition Geometry. In order to simulate data acquisition by a serial CdTe detector behind a parallel-hole collimator, the single detectors were translated along the z-axis.

Image Acquisition

The imaging geometry is shown in Figure 4.1.3. Gold K-shell fluorescence photons were acquired by two identical thermoelectrically cooled cadmium telluride (CdTe) photodiode detectors (XR-100 T-CdTe, Amptek Inc). A digital pulse processor and multichannel analyzer (PX4, Amptek Inc) interfaced between the detectors and a personal computer, which collected, stored, and analyzed the results. Since the measured spectrum of photons emitted from the phantom was overwhelmingly dominated by Compton scatter (see Figure 3.1.3), it was essential to restrict the view of the detector within the phantom as tightly as possible. Thus, each detector sat behind a 4-cm-thick lead pinhole collimated with a hole diameter of 2.5 mm.

The view of each detector was along the x-axis, at a 90º angle to the central axis of the beam (z-axis). The system remained stationary for the acquisition of each projection, which lasted 1-5 minutes. After this, the phantom was rotation about its central axis by 6º, and this process was repeated for 60 projections, corresponding to 360º coverage of the phantom. In order to simulate an 11-pixel serial detector, each CdTe detector was translated along the z-axis after the completion of a full 360º rotation. The detector positions were 3 mm apart, and these 11 positions spanned the entire length of the phantom. In order to increase the data collection rate, as well as the spatial resolution, the detectors were slightly offset. For each phantom rotation, the view of the two detectors was offset 1.5 mm apart along the z-axis.

Data were acquired as a series of five sets of 60 projections (each one minute long), allowing the reconstruction of images using one, two, three, four, or five minutes per projection. In order to correct for differences in detection efficiency between the two CdTe detectors used, the spectra of total counts from one detector were normalized to have the same overall count rate as the other detector. For each detector position and projection angle, the gold fluorescence peak height was extracted from the Compton scatter background using the method described in Section 3.2, and these signals were assembled to form a sinogram of gold fluorescence signal with respect to position and angle. The reconstruction of the images was also accomplished using the same procedure as described in Section 3.2, which used a maximum-likelihood (ML-EM) iterative algorithm which corrected for the effects of attenuation in both the primary beam and emitted fluorescence photons.

4.2 - XFCT Sinograms and Reconstructed Images

It was necessary to normalize the magnitude of the spectra received by the two CdTe detectors, owing to the differences in response between them. This was done by equalizing the total sum of the detector response at each position. Ideally, this effect of detector response would be built into the attenuation matrix M (see Eq. 3.2.1) through standardized measurements with a constant source. However, the method used was adequate for these purposes.

The measured sinograms and reconstructed images for 360º acquisition are shown in Figure 4.2.1. Measurements were taken as a series of five 1-minute-projection acquisitions, allowing the reconstruction of images using one, two, three, four, or five minutes per projection. One can see that, as the amount of data collected increases, the image quality improves. In the 1-minute image, only the 2% column is well defined, and there is excessive noise throughout the image. At 3 minute per projection, all three columns are well defined and the noise is only a slight problem. There appear to be diminishing returns past 3 minutes per projection. The right column in Figure 4.2.1 shows the relationship between signal intensity in the reconstructed image and gold concentration. The goodness of fit (R^2) value for the 5 minute image is 0.93. The only significant change in this curve as more dose is given is to bring the intensity down for pixels that should not have any fluorescence signal.

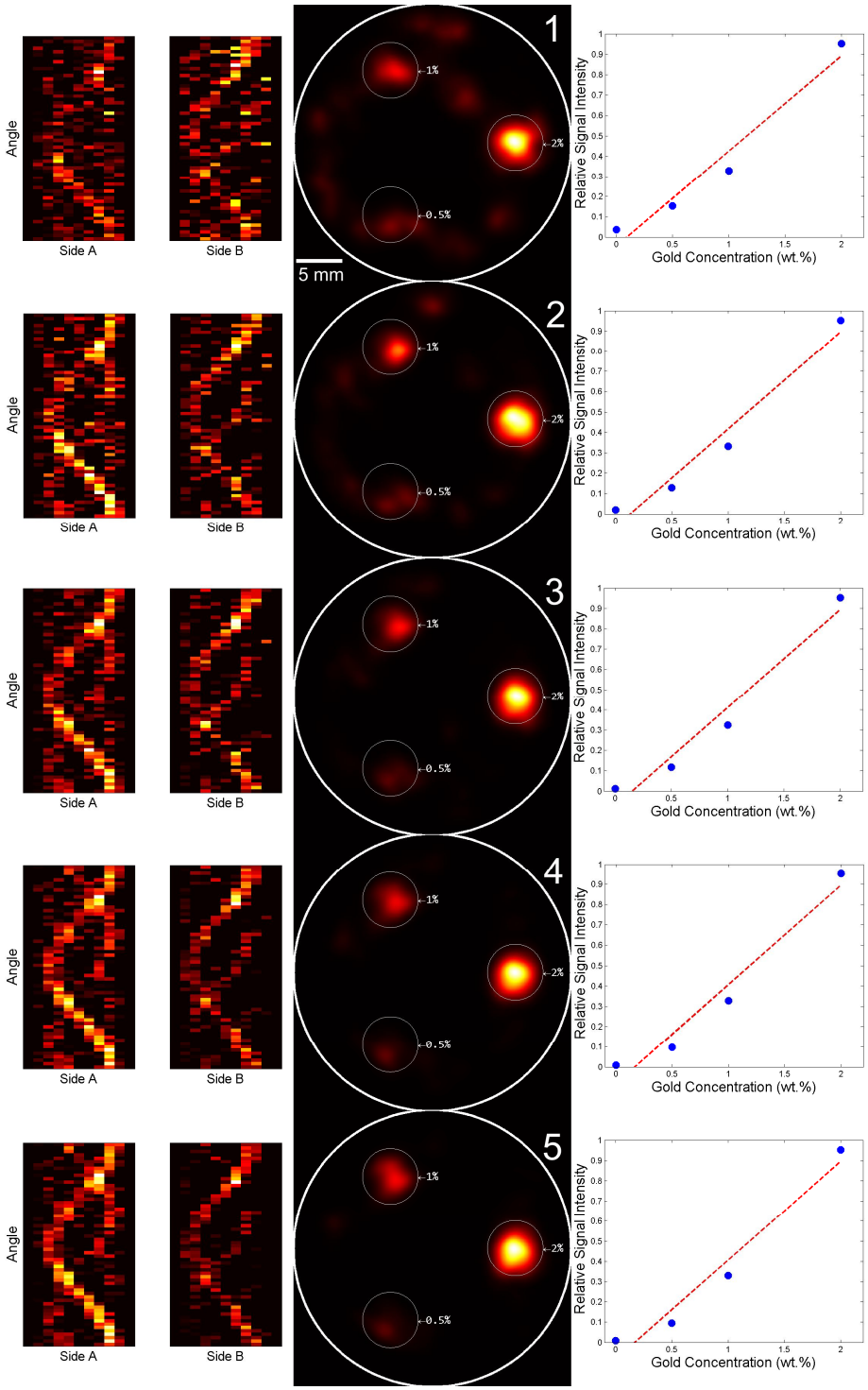

Figure 4.2.1: Reconstructed images of the 3-cm-diameter phantom for data acquisition using 1-5 minutes of scanning time per projection. Each phantom is labeled with the gold concentration (by weight) of each GNP-loaded column included. The right-side panels show the linear relationship between gold concentration and average signal intensity in each column. Results are shown for the XFCT setup with 360° data acquisition.

Figure 4.2.2 shows the results of several imaging metrics for images reconstructed using varying amount of information. The Image Error Factor is a function of the differences between the reconstructed and expected pixel value at each point in the image. For pixels within the GNP-loaded regions, the error is simply the square of the difference between actual and expected values. For pixels outside the GNP-loaded regions, the expected value is zero, and the sum of the squared differences is generally small compared to that of the GNP-loaded regions. However, these false-positive signals severely degrade the quality of the image. Therefore, for these pixels, the error factor is multiplied by a scalar factor to make the magnitude of the false-positive error comparable to that of the GNP-loaded regions. Data are shown for images reconstructed using only data from detectors on one side of the phantom as well as images using both detectors. Images are reconstructed using 30, 45, or 60 projections (180º, 270º, and 360º, respectively), corresponding to 50%, 75%, or 100% of the maximum imaging dose per projection. As expected, the image error decreases in all cases as more dose per projection is used. One can also see that, in general, the image quality improves as two detectors are used instead of one, and also as more projections (and therefore dose) are used.

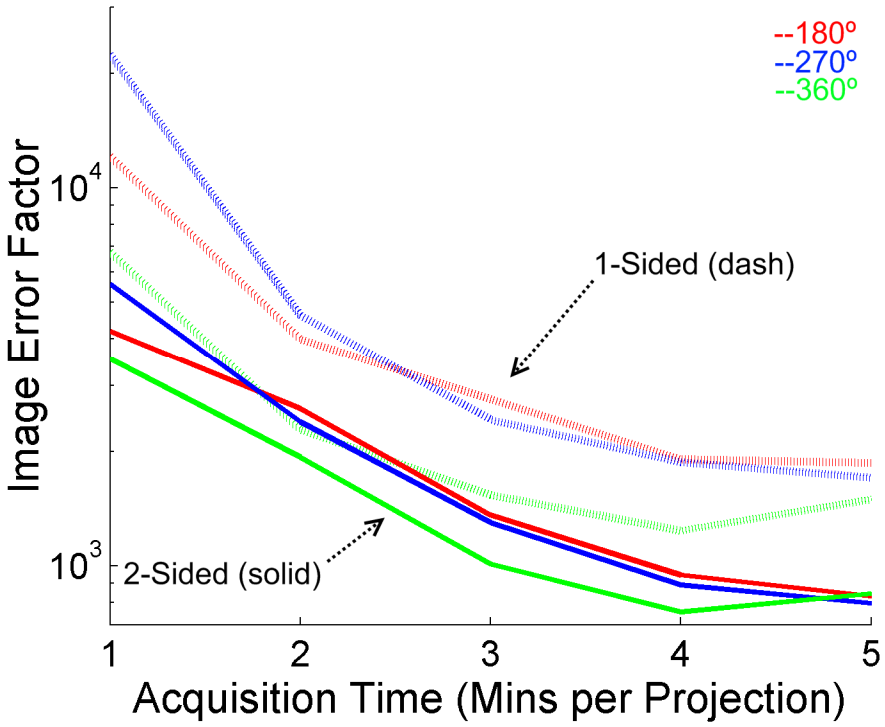

Figure 4.2.2: Image Error Factor for images reconstructed using varying amounts of information. As the error factor decreases, image quality improves. The dashed lines represent images reconstructed using only data from detectors on one side of the phantom, while the solid lines are those images using both detectors. Images are reconstructed using 30, 45, or 60 projections (180º, 270º, and 360º, respectively), corresponding to 50%, 75%, or 100% of the maximum imaging dose per projection.

4.3 - XFCT Imaging of Larger Phantom

The primary obstacle to a successful implementation of XFCT is the amount of Compton scatter which occurs within the phantom. Therefore, a larger object is more difficult to image with a cone beam as there is more scatter which drowns out the gold fluorescence signal. Early testing of cone beam XFCT was done using the same experimental setup as the pencil beam scanning: namely, a 5-cm-diameter phantom irradiated by a 110 kVp source filtered with 0.68 mm lead. It was seen that, using this configuration, it was difficult to image the regions loaded with GNPs at 1% by weight or lower. Once the

methods of cone beam XFCT were refined (Section 4.1) the 5-cm phantom (Figure 4.3.1) was revisited.

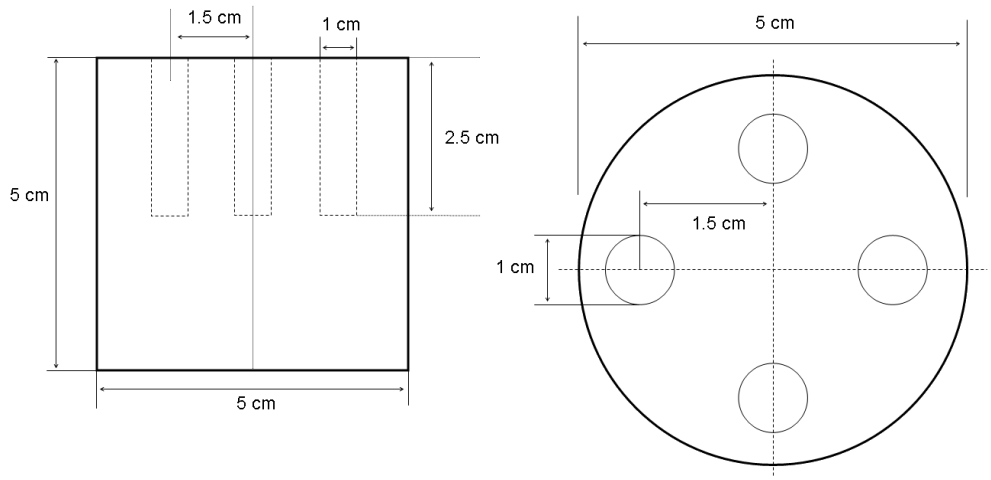

Figure 4.3.1: 5-cm-diamter phantom for XFCT imaging.

The 5-cm phantom was imaged using the same procedure described in Section 4.1. Note that, instead of the prior GNP-column configuration (3 columns 120º apart), the 5-cm phantom contains 4 holes for GNP-loaded tubes. For this image, three of the columns were filled with tubes containing water and GNPs at 2%, 1%, and 0.5% by weight. The tubes were 1 cm in diameter, and 3.5 cm in height. They sat in the phantom at a depth of 2.5 cm, with 0.5 cm extending above the top. The fourth hole was filled with a PMMA plug. The only difference in imaging setup was that the phantom center was 22.9 cm from the source exit window, in order for the beam to cover the entire phantom. This resulted in a lower dose rate than in the 3-cm phantom case (see Section 4.4). The image reconstruction process was also identical to the methods described in Section 4.2.

Imaging Results

The results of the 5-cm phantom XFCT are shown in Figure 4.3.2. All data are shown for sinograms and images reconstructed using 60 projections per scan at an interval of 6º, resulting in 360º coverage of the phantom. The time per projection varied from 1 to 5 minutes. Several points are notable from this figure. First, it was possible to distinguish all three gold columns (2%, 1%, and 0.5% by weight). Second, the imaging results are very noisy, even at 5 minutes per projection. This is due to both the increased phantom size (increasing Compton scatter and decreasing signal-to-noise ratio) and decreased dose rate of the source at this distance. However, it can be seen that the 5 minute image in the 5-cm phantom is roughly equivalent to the 3 minute image in the 3-cm phantom in terms of noise in gold-free regions. The goodness of fit (R^2) value for the 5 minute image is 0.99.

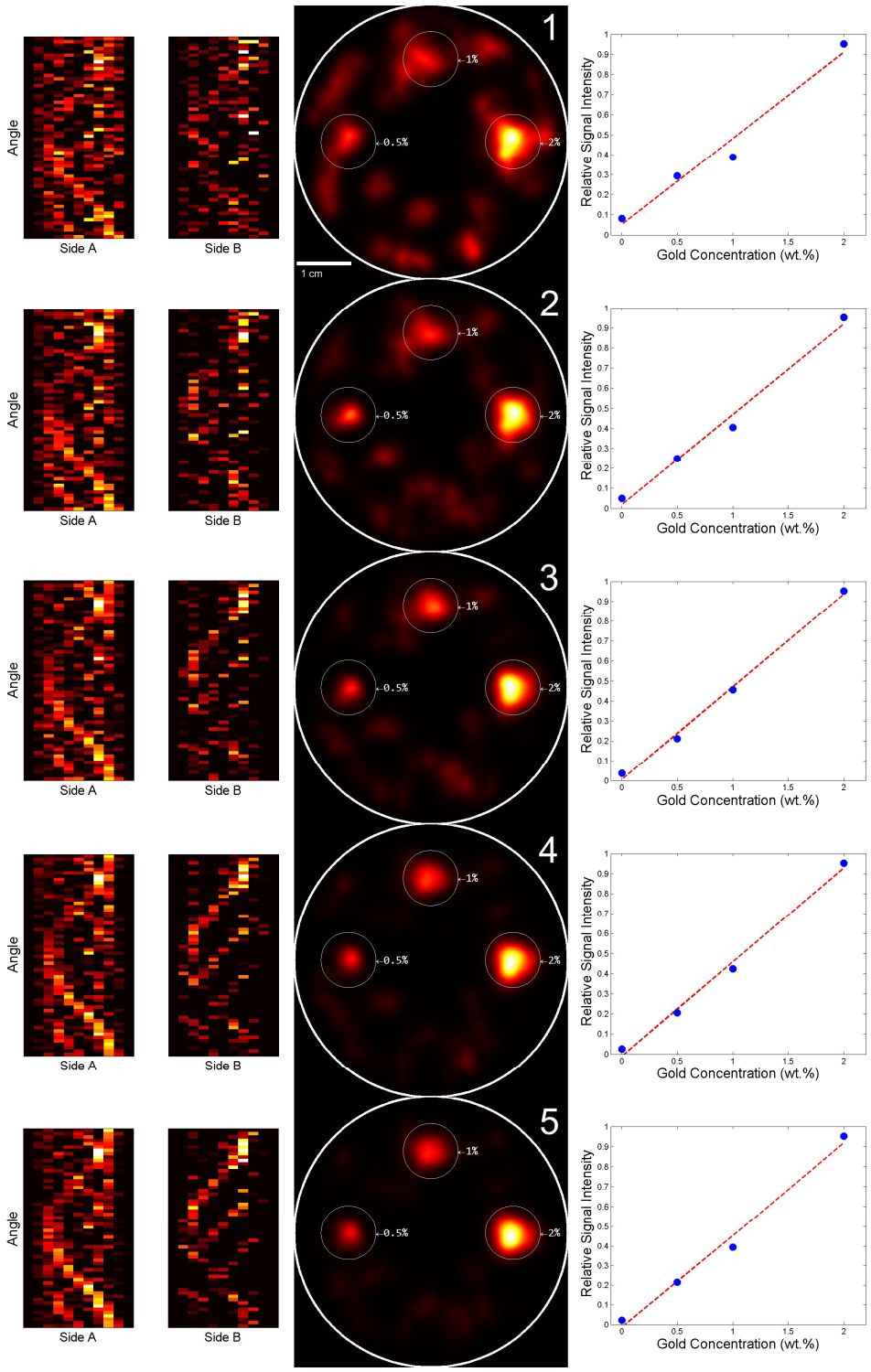

Figure 4.3.2: Reconstructed images of the 5-cm-diameter phantom for data acquisition using 1-5 minutes of scanning time per projection. Each phantom is labeled with the gold concentration (by weight) of each GNP-loaded column included. The right-side panels show the linear relationship between gold concentration and average signal intensity in each column. Results are shown for the XFCT setup with 360° data acquisition.

4.4 - Dose Measurements for XFCT Imaging Procedures

In order to measure the x-ray dose delivered during XFCT scanning, ion chamber measurements were performed using a standard Farmer-type ionization chamber (PTW N30013). The PMMA dose phantom, shown in Figure 4.4.1, consisted of a central 3-cm-diameter base and a 1-cm-thick cylindrical sleeve, which when placed onto the base makes a 5-cm-diameter cylindrical phantom. This allowed for dose measurements to be performed for both the 3-cm and 5-cm diameter phantoms. The phantom contained holes matching the shape of the ion chamber spaced roughly 1 cm apart. For each measurement, the chamber was placed into one of the phantom holes, and the others were filled with PMMA plugs whose shape matched that of the hole.

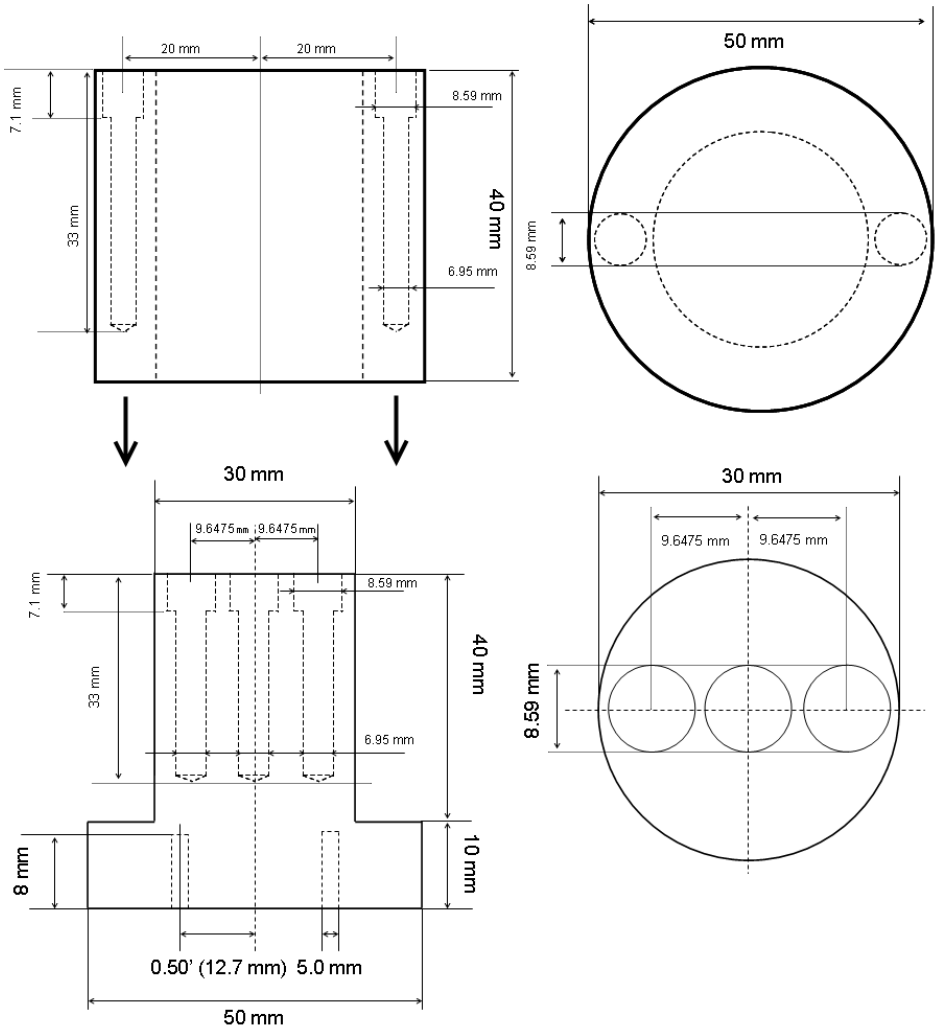

Figure 4.4.1: Dose Phantom for Ion Chamber Measurements. The dose phantom consists of a central 3-cm-diameter PMMA base and a 1-cm-thick cylindrical sleeve, which when placed onto the base makes a 5-cm-diameter cylindrical phantom. The phantom contains holes matching the shape of a PTW N300001 Farmer chamber spaced roughly 1 cm apart.

The dose measurement geometry was identical to the irradiation geometries used in Sections 4.4.2-3. The center of the 3-cm phantom was placed 14.5 cm from the beam exit window, while the 5-cm phantom (3-cm base with 1-cm-thick sleeve) was centered at 22.9 cm from the exit window. In both cases, the x-ray beam used matched the beam used in the corresponding 3-cm/5-cm imaging scenario in power/filtration used.

Measurement Protocol

Dose calibration was performed according to the AAPM TG-61 protocol,[61] using the aforementioned Farmer-type chamber connected to an electrometer (Max 4000, Standard Imaging, Inc). There were some deviations from this procedure: namely, calibration was performed in-phantom rather than in water, and the field size was the same as that used for imaging rather than 10x10 cm^2. The first problem was taken into account through the attenuation ratio (μ_{en}/ρ) for PMMA and air, and the second factor lead to some uncertainties (~1%) in the chamber correction factor $P_{Q,chamb}$, which was deemed acceptable within the scope of current study. The half-value layer (HVL) of the beam was measured to be 12 mm Al. This value is generally found in diagnostic beams > 150 kVp; however, the heavy filtration used (1.0 mm Pb) significantly hardens the beam. Because of this, the attenuation ratios (μ_{en}/ρ) for PMMA, air, and water were calculated explicitly using the measured spectrum in Figure 4.1.2.

Using this procedure, the dose rate was measured at the center of the phantom. For the 3-cm phantom, the dose rate was 0.17 cGy/min; for the 5-cm phantom, 0.092 cGy/min. The differences were due to both the increased size of the 5-cm phantom as well as the closer source-to-phantom center distance of the 3-cm phantom (14.5 cm vs. 22.9 cm). Dose was also measured at several points throughout the phantom. From these data, percent depth-dose and dose profile curves were constructed. These are shown in Figure 4.4.2. Additionally, it was measured that the dose rate for a full revolution of the

phantom was constant for points at various radial distances from the center (< 0.5% difference).

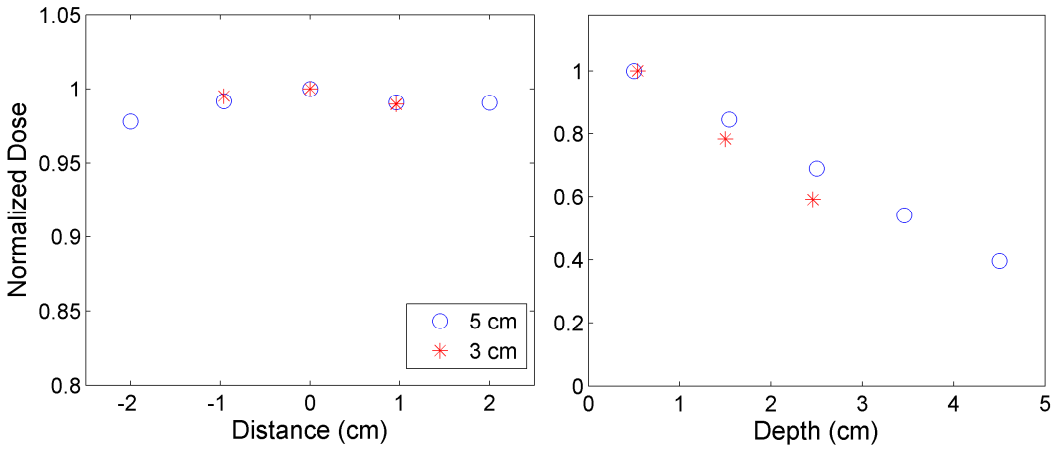

(a) (b)

Figure 4.4.2: Dose profile (a) and percent depth-dose (b) for the 3-cm and 5-cm phantoms. Dose profiles are measured at a depth equivalent to the center of the phantom.

4.5 - MicroCT of GNP-loaded Phantom

In order to compare the performance of XFCT to existing imaging modalities, a Micro Computed Tomography (MicroCT) scan of the XFCT phantom was performed. The image was performed on the 3-cm phantom (see Section 4.1). The phantom contained three GNP-loaded tubes, which contained a mixture of water and GNPs at 2%, 1%, and 0.5% by weight. The image was acquired using a commercial MicroCT scanner (SCANCO Medical) operating at 90 kVp filtered by 0.1 mm of aluminum. 512 projections were acquired with an integration time of 300 ms. The results of this scan are shown in Figure 4.5.1.

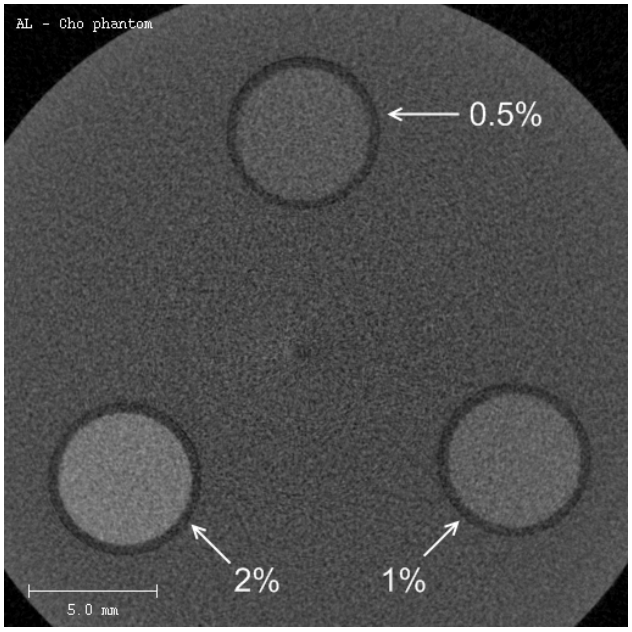

Figure 4.5.1: MicroCT of GNP-loaded phantom. The 3-cm-diameter contained three tubes with a mixture of water and GNPs. The concentration (weight %) of GNPs in each tube is denoted in the figure.

In Figure 4.5.1, it can be seen that there is a large amount of contrast in the case of the 2% tube, allowing one to discern its location. There is a significant decrease in contrast for the 1% and 0.5% tubes. It may be possible to distinguish these concentrations of GNPs in an otherwise perfectly homogeneous phantom, but in a realistic small-animal scenario, one would expect heterogeneities such as bone, lung, or other organs to make the small Hounsfield unit (HU) change due to GNPs indistinguishable. However, XFCT is acquired at a 90º angle with respect to the beam axis, and does not interfere with a normal transmission image. Consider the hypothetical fusion image shown in Figure 4.5.2. This image was formed by scaling/rotating the MicroCT and XFCT results by hand in order to align the relevant structures. It is possible that XFCT and MicroCT images could be acquired simultaneously using a single piece of equipment. Similar to

PET/CT, these two modalities are complimentary, with one providing anatomical information and the other providing functional information.

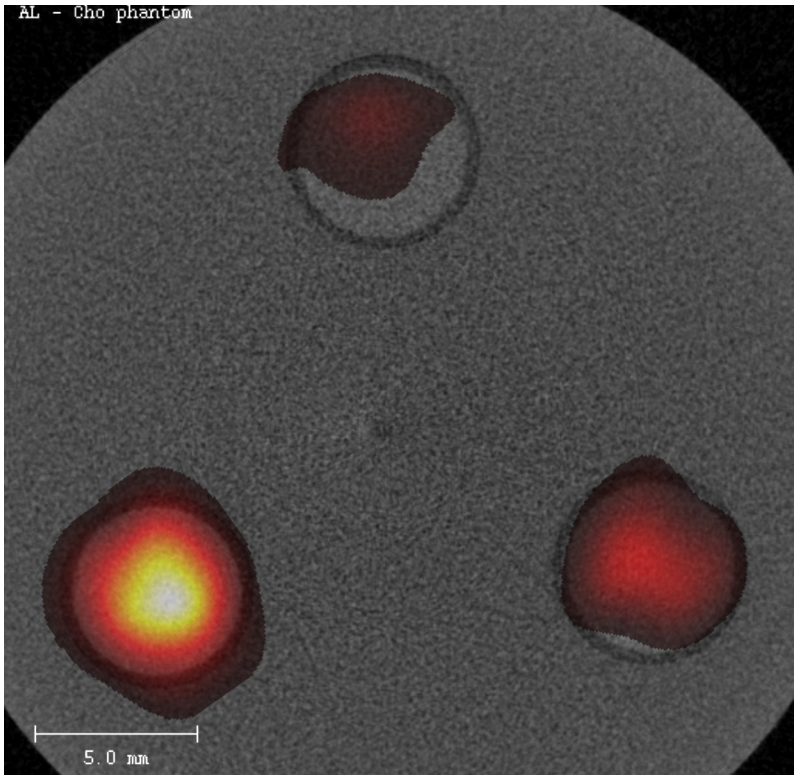

Figure 4.5.2: Fusion Image between MicroCT and XFCT.

One would also expect that XFCT would outperform MicroCT in delineating the location of GNPs in a heterogeneous geometry. Consider the geometry in Figure 4.5.3. This is a hypothetical MicroCT image of a phantom containing three GNP-loaded regions and three high-density regions such as bone. In this case, based on material density alone, MicroCT may not be able to distinguish between the two. However, by augmenting the image with XFCT, it becomes possible to distinguish the bones from GNP-loaded regions.

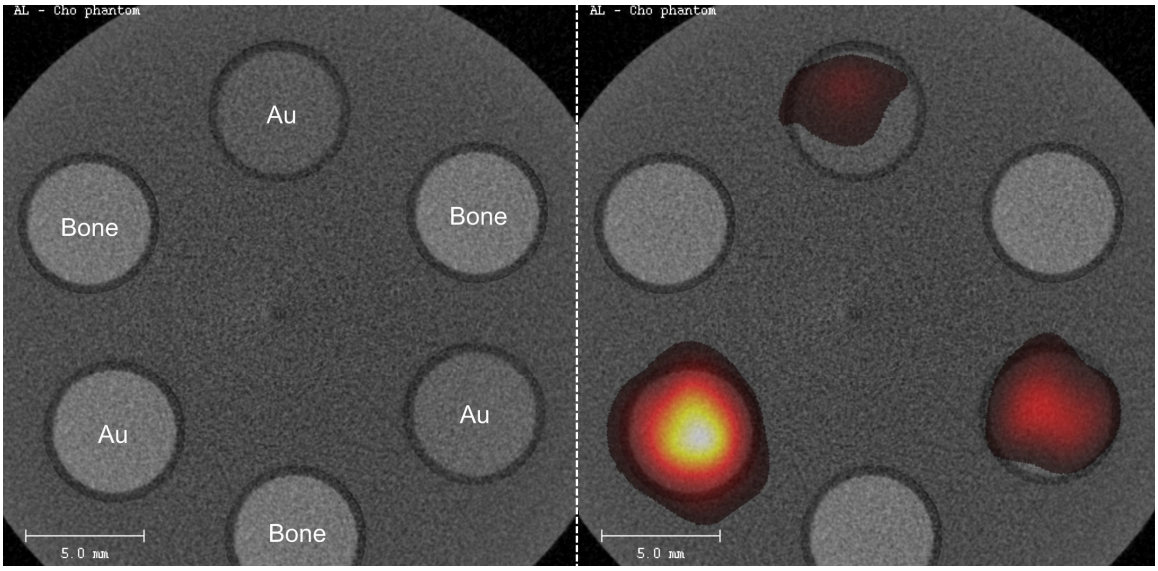

Figure 4.5.3: Hypothetical MicroCT/XFCT image of a digitally fabricated phantom containing three GNP-loaded regions and three high-density or "bone" regions. The left image shows the expected result of MicroCT scanning, and one cannot distinguish GNP-loaded regions from bones based solely on material density. The right panel shows a hypothetical CT/XFCT fusion image, allowing one to distinguish the two different regions.

4.6 - Monochromatization of Polychromatic X-Ray Source

The data collected during XFCT scanning are overwhelmingly dominated by Compton scatter, with a signal-to-noise ratio (SNR) of 1/100 to 1/1000. The quality of the reconstructed image can be significantly improved if advances can be made in reducing the amount of scattered photons. This makes it especially important to take great care in determining the spectrum of source photons used for XFCT. Ideally, the beam spectrum would be such that the gold fluorescence peaks and the Compton scatter spectrum of the beam are at different energies; however, due to the physics of x-ray generation and the limitation that the beam must be at least 80.7 keV to trigger gold *K*-shell fluorescence, this becomes difficult to accomplish realistically. Synchrotron facilities can produce very

bright monochromatic beams, but it is challenging to monochromatize a polychromatic broad-beam spectrum from a traditional x-ray tube.

Recently, efforts have been made to monochromatize a polychromatic broad-beam spectrum using Bragg Diffraction in a medium with sufficiently small lattice spacing, such as highly-oriented pyrolitic graphite (HOPG). This technology has been applied to radiation-based imaging and therapy,[62-63] and efforts were made to adapt this approach to GNP-based XFCT in the current study. Bragg Diffraction is governed by the relationship in Eq. 4.6.1, where the lattice spacing d and the angle of incidence θ define the wavelength λ that is coherently scattered out of the lattice.

$$2d \sin \theta = n\lambda \qquad \text{Eq. 4.6.1}$$

By depositing a thin film of HOPG (d = 335.4 pm) onto a properly curved surface, powerful manipulations of the x-ray spectrum are possible.[64] The goal in the case of XFCT is to scatter the beam in such a way as to create a source spectrum that, when scattered into the detector, does not significantly interfere with the gold fluorescence photons. To accomplish this, MCNP5[57] simulations were performed in which a PMMA phantom was irradiated by various quasi-monochromatic x-ray spectra. The phantom contained a region loaded with GNPs at 2% by weight, and the spectrum of photons emitted from the phantom was collected by an energy-sensitive volumetric (F4) tally placed at a 90º angle relative to the beam central axis, whose geometry mimicked a commercial CdTe detector. Quasi-monochromatic spectra were used due to the slight

angular spread of materials such as HOPG, causing the reflected spectrum to contain some deviation in energy. The results of these simulations are shown in Figure 4.6.1 for quasi-monochromatic sources of average energy 85, 90, and 95 keV, each with a full-width half-maximum (FWHM) of 5 keV. It is apparent that a source energy of at least 95 keV must be used for quasi-monochromatic XFCT at a 90º detection angle, otherwise the Compton scatter obscures the resultant gold fluorescence peaks. From Eq. 4.6.1, the 95 keV photons could be extracted from a polychromatic beam if it was incident onto a layer of HOPG at an angle of n*1.1º (n = 1, 2, 3 …).

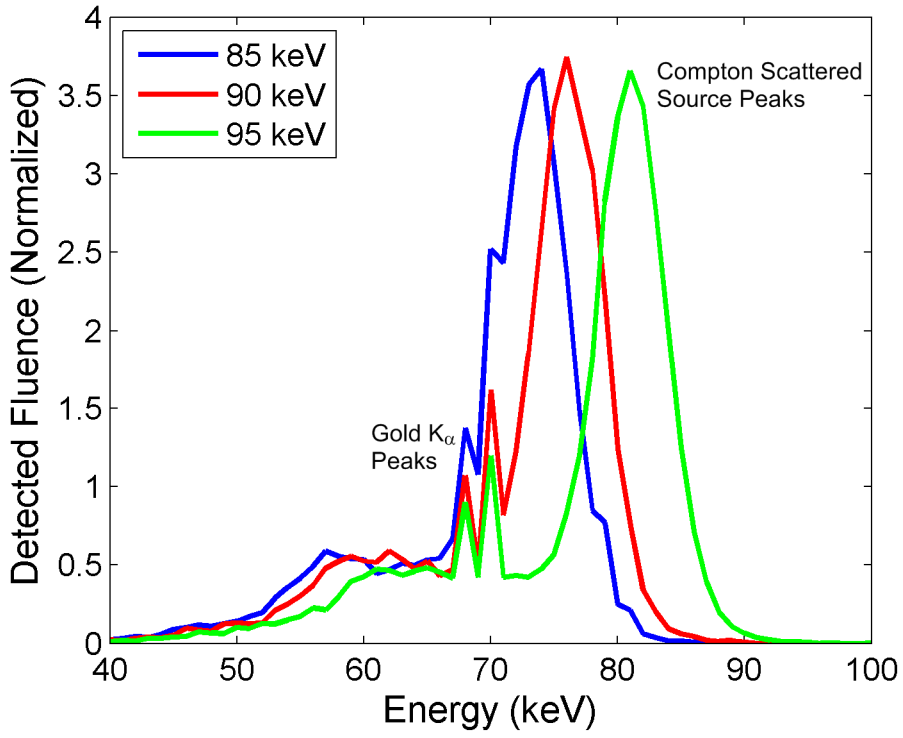

Figure 4.6.1: Spectrum of gold fluorescence and Compton scattered photons from quasi-monochromatic x-ray source spectra (FWHM 5 keV). At least 95 keV is required for a clear view of gold K_α peaks.

Unfortunately, this extremely small scattering angle makes this application difficult for benchtop, cone-beam use. Even if the n=5 angle of 5.5º was used (which would require filtration of the lower energy multiples of λ), a configuration capable of creating a quasi-monochromatic broad beam is challenging to envision. Figure 4.0.2 shows the shape of an HOPG layer required to reflect the rays of a cone beam at 5.5º. The cone beam enters the frame from the left side, and the HOPG layer is represented as a roughly parabolic black line. The color of the lines show the path of each ray as it reflects from the HOPG layer. Photons in the cone beam which do not match the energy of the required Bragg diffraction angle would interact with the HOPG layer normally.

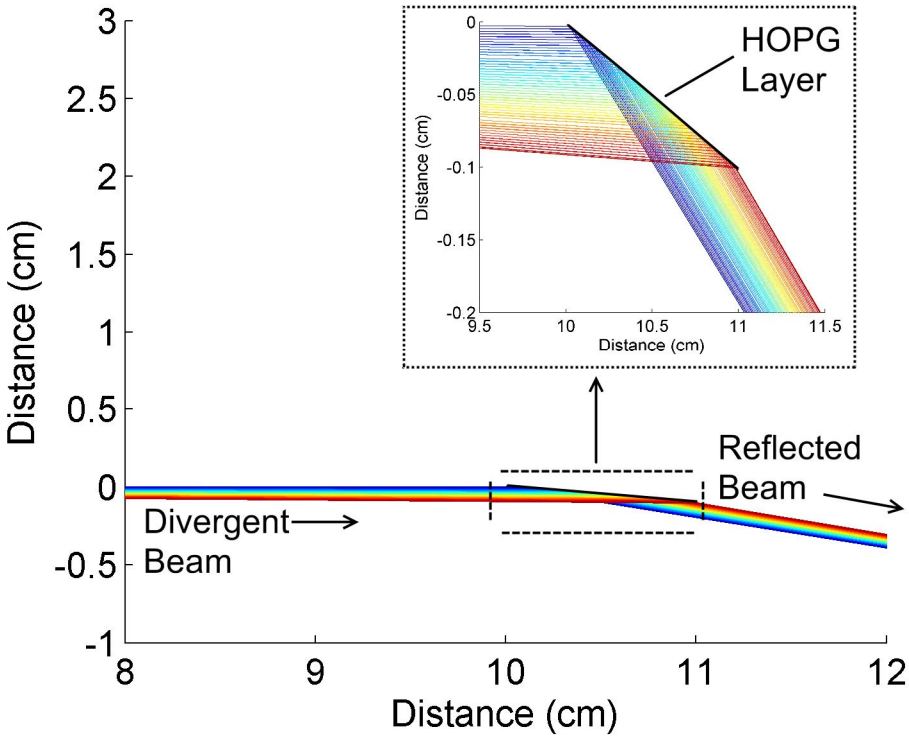

Figure 4.6.2: Monochromatic reflection of a cone-beam source with a thin HOPG film. A cone beam (source located at x=y=0, not shown) is reflected with HOPG at 5.5º, causing 5th-order Bragg diffraction of 95 keV photons. The curved HOPG surface required is 1 cm long and roughly 1 mm tall.

This low scattering angle geometry makes monochromatization difficult for many reasons. First, any slight change in angle has a very large effect on the scattered energy. For instance, at 1.1º, an increase of 0.5º corresponds to an energy of 65 keV (Eq. 4.6.1). Effects such as the intrinsic mosaic spread of HOPG and the x-ray spot size would increase the uncertainty in scattering angle. Secondly, in order to have any impact on the beam spectrum, one must separate the scattered photons from the primary beam. This could most easily be accomplished by constructing a cylindrical HOPG scatterer with an attenuator such as lead in the center. However, for the geometry in Fig. 4.6.2, this cylinder would have an inner radius of approximately 1 mm, and would utilize a very small fraction of the x-ray beam resulting in a low imaging dose rate.

On the other hand, there is no doubt that this method holds great promise for improving GNP-based XFCT. Figure 4.6.3 shows the spectrum of photons diffracted from a small layer HOPG. A 1x1 cm^2 piece of commercially available HOPG (1.2 mm thick, mosaic spread 1º, NT-MDT Co.) was placed in a pencil beam of 110 kVp photons 1.5 mm in diameter. A CdTe detector was placed just laterally outside the primary beam at a distance of 50 cm from the HOPG crystal. The detector was collimated by a 2x2x4 cm^3 lead pinhole collimator with a hole diameter of 2.5 mm. While the measured spectrum is far from ideal, including a large variance in the peak energy spread as well as Compton scattered photons, it demonstrates that, with a more careful approach to the HOPG geometry, it may be possible to reasonably monochromatize the 110 kVp beam for benchtop applications.

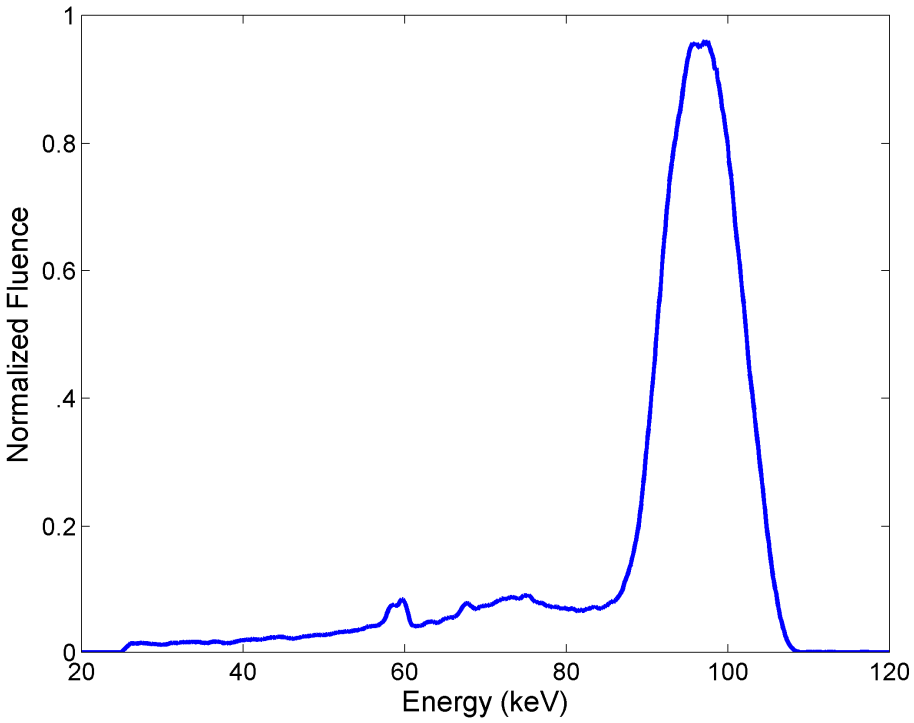

Figure 4.6.3: Spectrum of 110 kVp x-rays measured after small-angle reflection from a thin 1x1 cm^2 HOPG crystal.

4.7 Discussion

This study demonstrates the feasibility of imaging GNP location and concentration within 3-5 cm objects using an ordinary polychromatic x-ray source. Several molecular imaging applications of this technology are discernable. A recent study used conjugated quantum dots (QDs)[27] for molecular imaging of tumors *in vivo*. Another study[26] demonstrated the feasibility of targeting tumors using bio-conjugated GNPs. While optical imaging techniques can be used to image QDs *in vivo*, no current imaging modality can image GNPs *in vivo*. With some refinements to detection limit and scan time, it would eventually be possible to generate both 2D and 3D tomographic images of an animal injected with conjugated or unconjugated GNPs using XFCT.

It was found that the dose rate during imaging for the 3 and 5 cm phantoms was 0.17 cGy/min and 0.092 cGy/min, respectively. Thus, for the images described above containing 60 projections and 11 detector positions, the total dose delivered to the 3 and 5 cm phantoms was 5.7 Gy and 3.0 Gy, respectively. However, the cone-beam irradiation geometry allows for simultaneous data collection using multiple detectors, so the total dose could be reduced by a factor of 11 if a single-line CdTe array detector were used. A similar type of detector has been used for other similar imaging modalities, such as K-edge imaging.[41]

Table 4.7.1: Dose (cGy) required in the 3 and 5 cm phantoms for XFCT images acquired using 1-5 minutes per projection, with 30, 45, or 60 projections per image. This table assumes that an array detector is used.

Projection Time (min)	Projections per Image, 5 cm			Projections per Image, 3 cm		
	30	45	60	30	45	60
1	2.8	4.1	5.5	5.2	7.9	10.5
2	5.5	8.3	11.0	10.5	15.7	21.0
3	8.3	12.4	16.6	15.7	23.6	31.5
4	11.0	16.6	22.1	21.0	31.5	42.0
5	13.8	20.7	27.6	26.2	39.3	52.5

Table 4.7.1 shows the dose required to image the two phantoms using an array detector It was seen in Sections 4.3 and 4.4 that a sufficient image was generated with 60 projections using 3 min/projection in the 3 cm phantom, and 5 min/projection in the 5 cm phantom. Therefore, the dose required for XFCT imaging using the current methodology is roughly 30 cGy. This is much less than the general LD50 (50% Lethal Dose) for mice of about 7 Gy,[65] and possibly less than typical ranges of x-ray doses delivered during micro-CT scanning of small animals.[66-69] These are encouraging results, as they suggest

that XFCT is currently feasible with realistic constraints on the amount of x-ray dose delivered.

With an array detector, the scan time required could also be brought within acceptable limits. For a 60 projection scan, the time required for the 3 and 5 cm phantoms would be 3 and 5 hours, respectively. This could be further reduced by using a higher dose-rate source, or by improving image acquisition to require either less projections or less time per projection. It is also possible that the amount of data required to reconstruct an acceptable image could be reduced by using a more sophisticated gold fluorescence peak extraction algorithm, or by using a detector with a higher energy resolution at the energies considered (65-70 keV). With the implementation of all or part of these for the current XFCT setup, the scan time acceptable for routine *in-vivo* imaging work (~ < 1 hour) would ultimately be achievable.

CHAPTER 5

CONCLUSIONS

It has been shown that, by taking advantage of the high atomic number of gold (Z=79), several interesting applications for photon-based therapy and imaging are possible. The significant increase in photoelectric interaction probability for gold allows it to be used as a contrast agent, both in terms of increasing dose deposited during radiotherapy as well as allowing differentiation between gold-loaded and normal tissue during photon imaging. If gold nanoparticles (GNPs) can be preferentially targeted to tumor tissue, this allows one to selectively escalate dose to tumor tissue while sparing normal tissue from harm. If GNPs can be preferentially targeted to any structure (including tumors), this also allows one to generate a tomographic image of GNP location and concentration and, based on the results of this imaging, derive biological information about either the nature of the target of GNPs or the nature of the agents used to target them.

This study presents a nanometer-scale calculation framework which computes the energy spectrum of secondary electrons emitted during gold nanoparticle-aided Radiation Therapy (GNRT), the point dose kernels of these spectra, and the microscopic dose enhancement resulting from the addition of GNPs to tumors under realistic treatment scenarios. The results presented for dose enhancement during GNRT agree with the results of several other studies, including measurements of dose behind a gold foil,[51] theoretical calculations of GNP dose enhancement for vascular disruption,[70] and Monte

Carlo calculations of photon interaction enhancement in GNPs of various sizes.[50] The central theme of the GNRT-related results is that extreme dose enhancement can be achieved within very short (< 5 μm) distances from GNPs. Given the short ranges of secondary electrons from GNPs, it can be expected that the maximum radiobiological benefit (killing of tumor cells) can be accomplished by bringing the GNPs as close as possible to the target of the radiation, DNA. It is also apparent that the radiobiological consequences of GNRT are most likely dependant on the GNP distribution and energy spectrum used to take advantage of the enhanced photoelectric cross section.

This study also presents a potential benchtop molecular imaging modality for determining the location and concentration of high-Z materials in small animal-sized objects. The modality is based on the detection of K-shell fluorescence photons emitted by GNP-loaded regions in an object undergoing irradiation by a filtered cone beam of diagnostic polychromatic x-rays. The methods of data acquisition, fluorescence extraction from background, and image reconstruction were tested using Monte Carlo methods. The location and concentration of GNPs within a PMMA phantom was determined, and a lower limit of detection using this methodology was established at roughly 0.1% gold by weight. These methods were then applied to acquire images of GNP-loaded columns within PMMA phantoms of diameters 3 and 5 cm. The use of a cone beam image acquisition geometry allowed these images to be obtained under realistic constraints on dose, scan time, and resolution.

There are many avenues for improving upon the results of this work. The ultimate goal of this investigation is to apply the currently developed techniques to various pre-clinical studies with small animals. While it is difficult to experimentally verify dose delivered on such a small scale, the dose enhancement results presented here suggest a significant enhancement in the radiobiological consequences of radiation therapy by using GNPs; specifically, they predict an increase in the local dose deposited which would lead to an increase in tumor cell killing.

Since the results can be computed on extremely small (i.e. 1 nm) scales, the computational model presented here could be expanded to include calculating the dose directly to DNA or other cellular structures, given that the GNPs could be localized and imaged in a reasonable way. Since the size of the target of radiation damage (i.e. DNA) is roughly 2 nm in diameter, the dose enhancement results presented here could become part of a broader calculation framework which would use theoretical models to predict the number of single-strand/double-strand DNA breaks. Future targeting methods for GNPs could be evaluated based on a calculated cell survival fraction, and these results could be tested in *in vitro* dose enhancement studies. This would allow the formation of a calculation framework which could predict more accurately the radiobiological outcomes of GNRT.

There are also many feasible ways to improve imaging with XFCT. The most obvious improvement to the current XFCT setup would be the utilization of a CdTe array-based detection system that is able to record line integrals through the phantom in parallel

during cone-beam irradiation. This would immediately reduce scan time and dose by a factor of 11 or more, depending on the detector configuration. Moreover, since the measured signal is overwhelmingly dominated by Compton scatter and the primary impediments to image quality are the fluctuations in this scatter background, the best way to improve image quality is to reduce the amount of scatter. This could be accomplished using some novel configuration of HOPG which would create a bright, cone-beam, monochromatic source at 95 keV, which would significantly reduce the amount of Compton scatter detected at the energies of gold K_α fluorescence. Additionally, the results could be improved using a more sophisticated beam filter, such as one comprised of a tin/copper/aluminum mixture. Barring this, the signal could conceivably also be improved if some novel/sophisticated peak extraction algorithm were able to more easily discern gold fluorescence peaks from the Compton background. This would allow a reduction in x-ray dose delivered, or a decrease in the scan time required for image acquisition. This may also allow XFCT imaging of lower concentrations of GNPs or of larger objects.

XFCT is distinct in that it is a truly molecular imaging modality. Rather than detecting some property of a medium or an agent/molecule, XFCT is capable, in theory, of identifying any element within an object by observing its characteristic fluorescence. For a high-atomic-number agent, such as a GNP, it has been shown possible to image realistic concentrations (0.7 wt% Au) in a mouse-sized object. This technique could be used to facilitate small-animal studies for GNRT, and combined with the dose enhancement calculations presented herein could comprise a framework whereby the measured

concentrations of GNPs in a mouse tumor could be used to calculate the enhancement in photon dose during x-ray therapy. These results could be tested against the radiobiological outcomes of that therapy. XFCT could also facilitate small animal studies with any agent capable of functionalization with a GNP. For instance, if a novel drug or other therapeutic agent were attached to a GNP, XFCT could be used to measure the biological distribution of that agent within a mouse.

APPENDIX A

SPECTRUM OF SECONDARY ELECTRONS

A.1 - Spectrum of Secondary Electrons during GNRT

The secondary electron spectra from atoms of gold approximating GNPs and molecules of water during photon irradiation of a GNP-loaded tumor were obtained using the EGSnrc code system,[71] which was used to record the number and energies of electrons created through the photoelectric, Compton, and atomic relaxation processes. A total of six photon source spectra were considered: ^{125}I, ^{103}Pd, ^{169}Yb, ^{192}Ir, 50 kVp x-rays, and 6 MV x-rays. For the current investigation, water, instead of tissue, was chosen as the base material for the phantom and tumor, since the electron track structure code used for dose calculations is currently only capable of handling electron transport in water. For the brachytherapy sources (i.e., all sources apart from 6 MV), the dimensions of the phantom and tumor were 30 x 30 x 30 cm^3 and 3 x 3 x 3 cm^3, respectively. The tumor composed of either water or water loaded with gold at 7 mg Au/g was located centrally within the phantom and contained a source isotropically emitting photons at its center. In the case of the 6 MV x-ray source, the phantom geometry was altered to reflect external beam delivery rather than brachytherapy. Specifically, a 4 x4 cm^2 6 MV beam was incident normally onto the surface of a 30x30x30 cm^3 water phantom at 100 cm source-to-surface distance (SSD). The tumor was a 2x2x3 cm^3 region at 5-8 cm depth in the phantom along the central axis of the beam, and was composed of either water or water loaded with 7mg Au/g.

The six photon source spectra were chosen in an attempt to replicate realistic treatment scenarios. For ^{125}I, ^{103}Pd, and ^{169}Yb, measured spectra of physical brachytherapy seeds or sources were used.[22, 72-73] For ^{192}Ir, the spectrum of a microSelectron HDR source included in the EGSnrc code package was used. The 6 MV beam spectrum was obtained from a previous study on Varian 2100 series accelerators.[74] The 50 kVp source was intended to represent various miniature x-ray delivery devices,[75-77] but the spectrum used was that of a generic beam with 1.5 mm Al filter and 17° W target[78] independent of a particular make/model of miniature x-ray device. The cutoff energy for these simulations was 1 keV for both photon and electrons.

The secondary electron spectra for gold and water resulting from these photon irradiations are shown in Figures A.1-A.6. Here, the secondary electron spectra for gold are presented combined with the spectra for water to show the magnitude of the increase in secondary electron production caused by the presence of gold. On the other hand, during the current simulations for the dose point kernels, separate secondary electron spectra for gold atoms and water molecules were used.

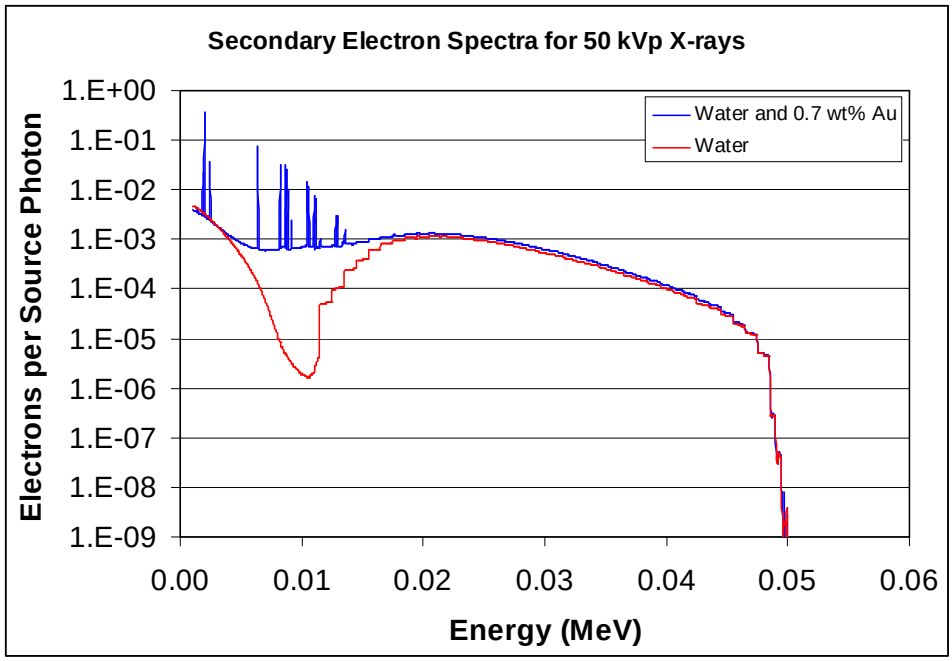

Figure A.1: Secondary Electron Spectra for 50 kVp X-ray Source

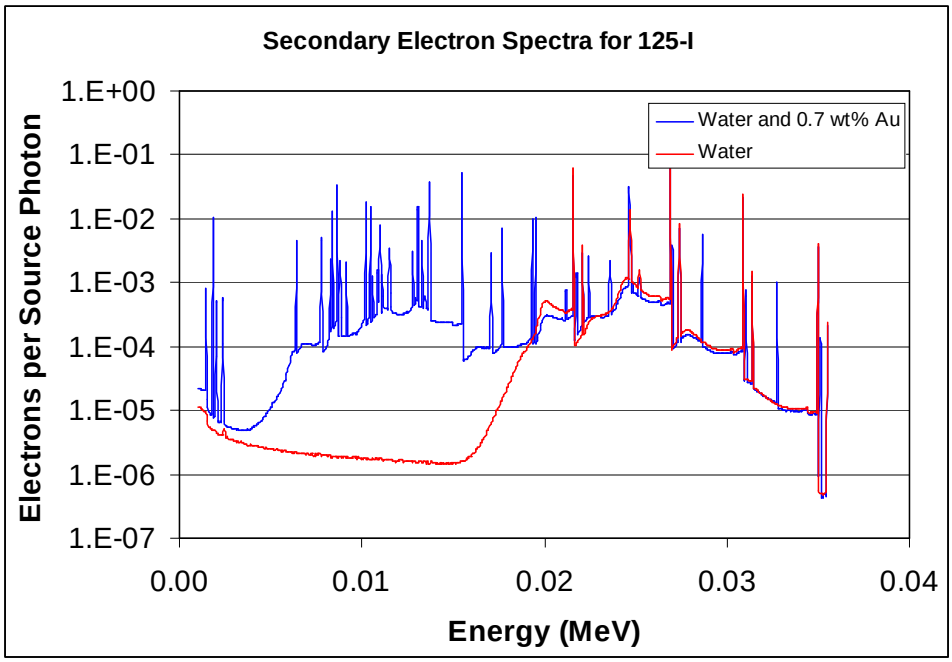

Figure A.2: Secondary Electron Spectra for ^{125}I Source

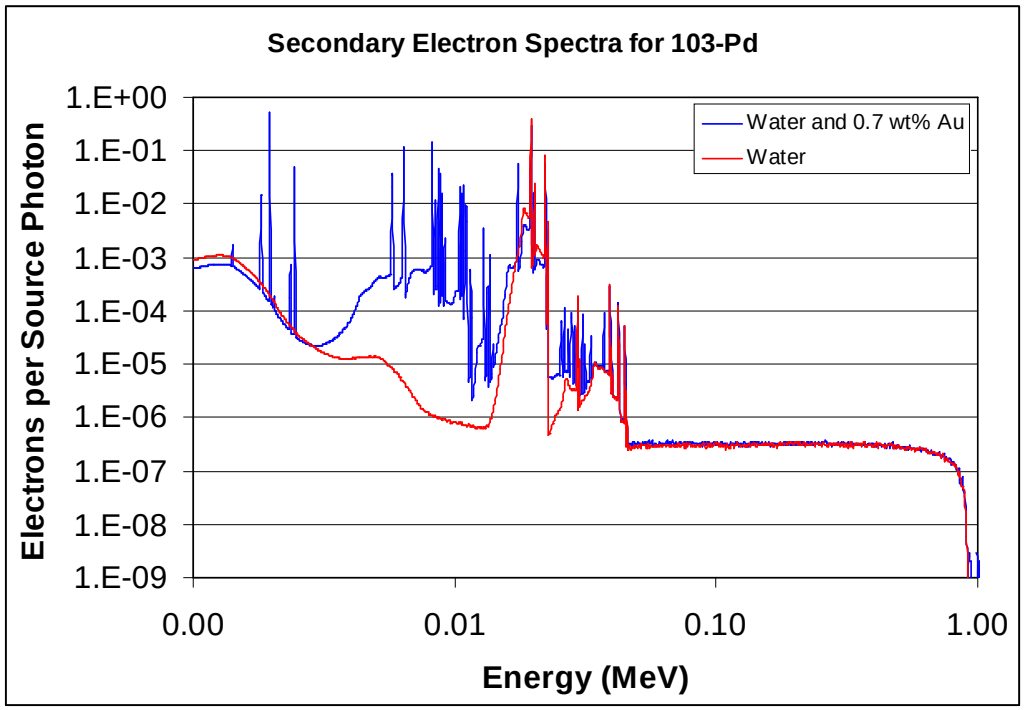

Figure A.3: Secondary Electron Spectra for ^{103}Pd Source

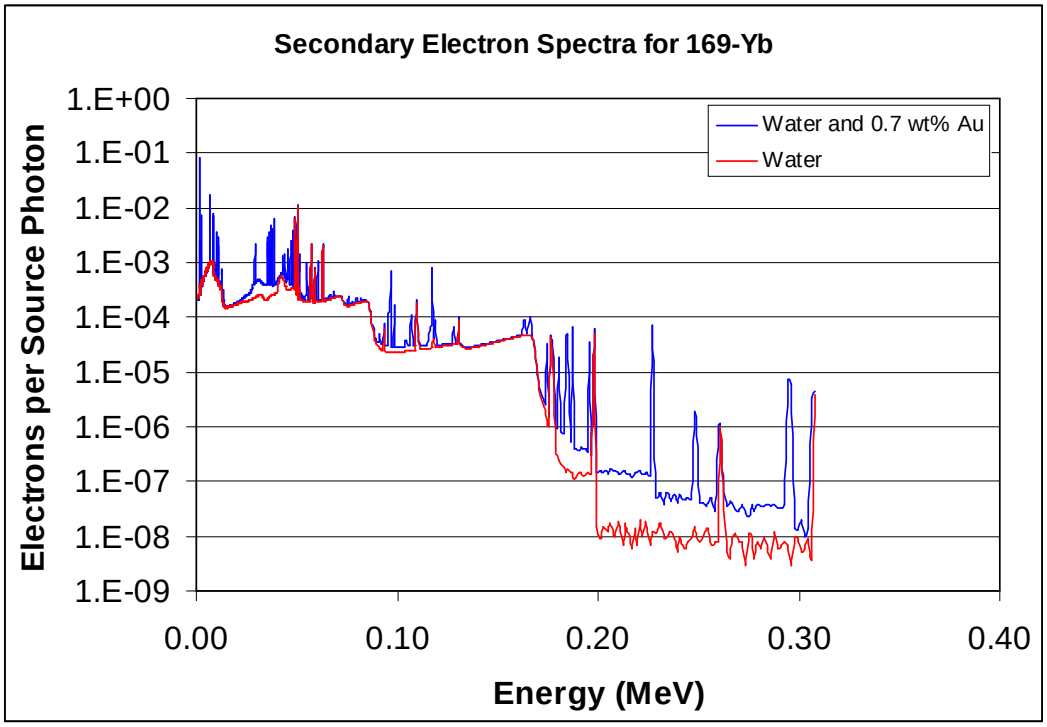

Figure A.4: Secondary Electron Spectra for ^{169}Yb Source

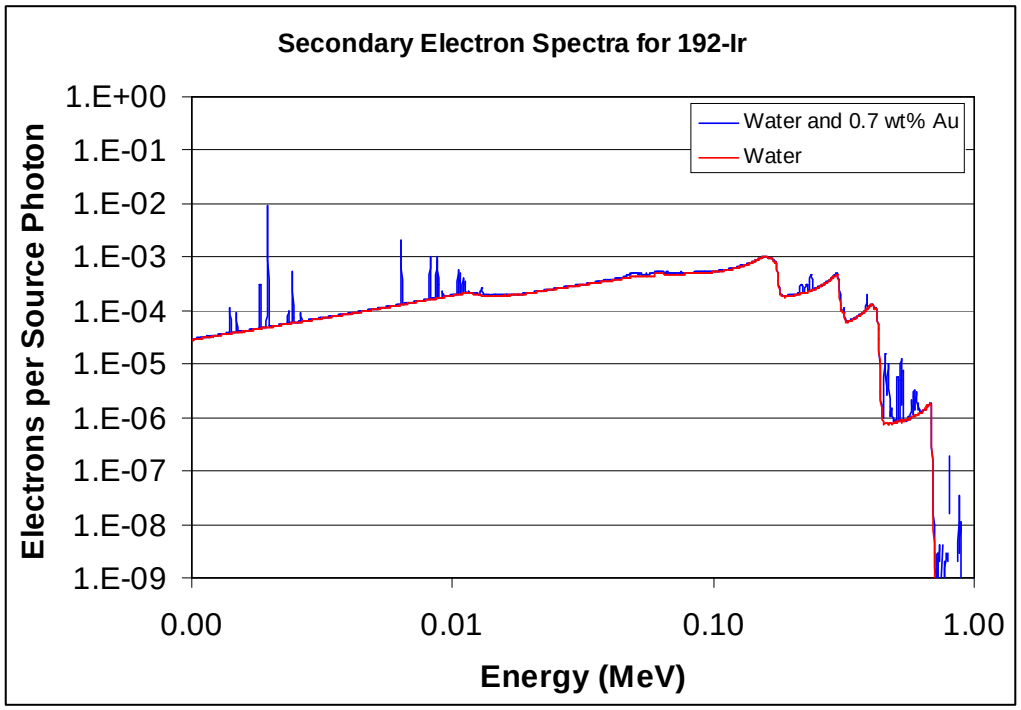

Figure A.5: Secondary Electron Spectra for ^{192}Ir Source

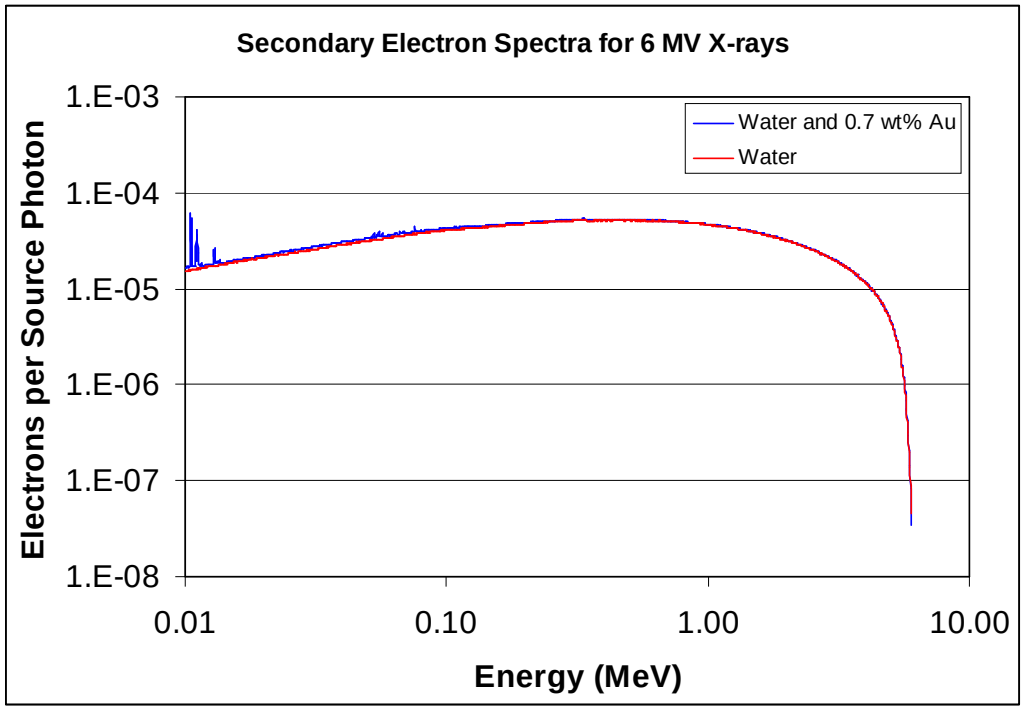

Figure A.6: Secondary Electron Spectra for 6 MV X-ray Source

APPENDIX B

MICROSCOPIC DOSE ENHANCEMENT

To calculate the microscopic dose enhancement due to the presence of gold, the kernels were applied to a scanning electron microscopy (SEM) image of a GNP distribution in tissue.[30] Using the methods described in Section 2.4, each pixel in the image was treated as a point source of either gold or water secondary electrons based on the intensity of that pixel, and with the dose point kernels, the radial dose distribution around each pixel was calculated. The microscopic dose enhancement due to GNPs in the sample SEM image, defined as the ratio of dose deposited at each point between the gold and water cases, is shown in Figures B.1-4 for the sources ^{192}Ir, ^{103}Pd, ^{125}I, and 6 MV.

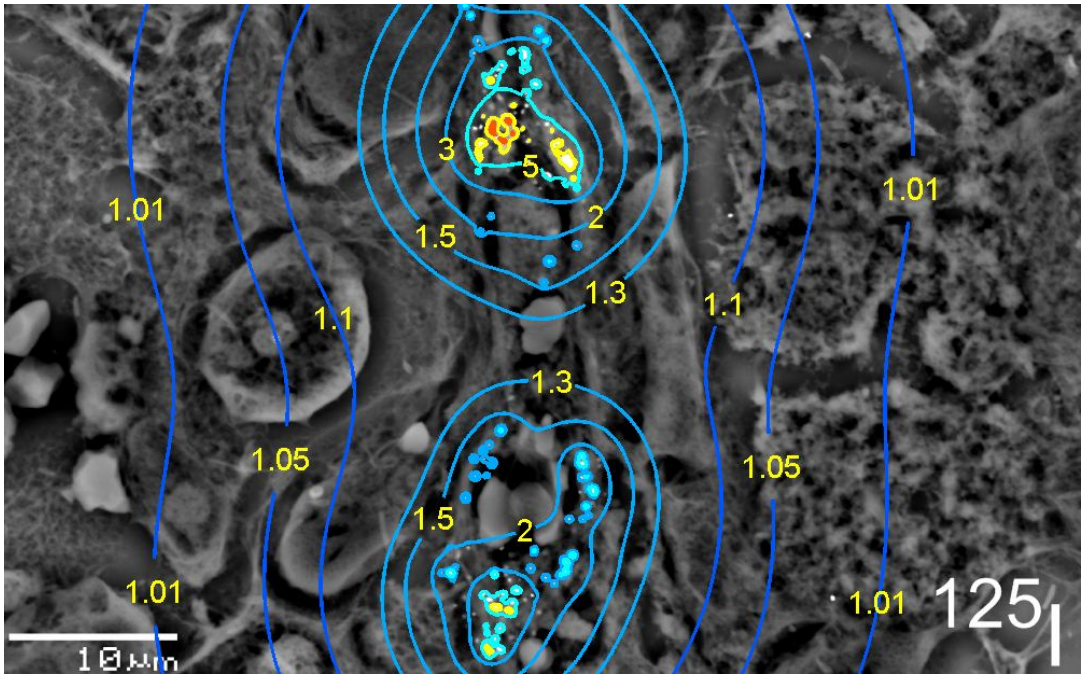

Figure B.1: Microscopic Dose Enhancement from ^{125}I photon source for the specific GNP distribution *in vivo* obtained from the previous work.[32] 1.05, 1.10, and 2 represent 5%, 10%, and 100% enhancement, respectively.

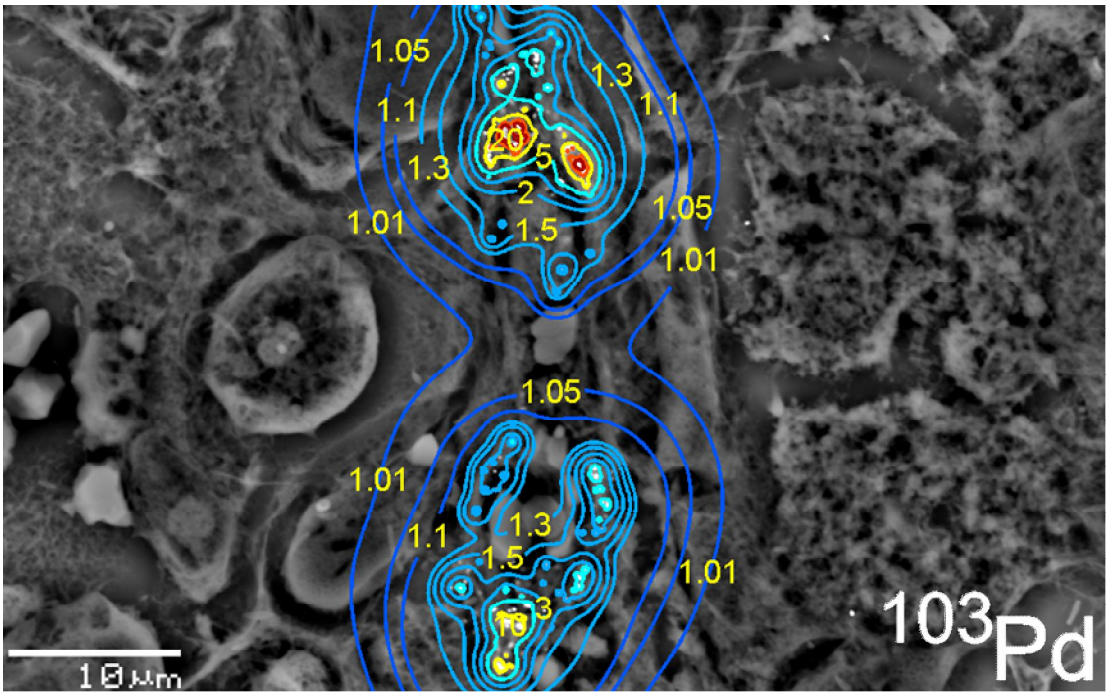

Figure B.2: Microscopic Dose Enhancement from ^{103}Pd photon source for the specific GNP distribution *in vivo* obtained from the previous work.[32]

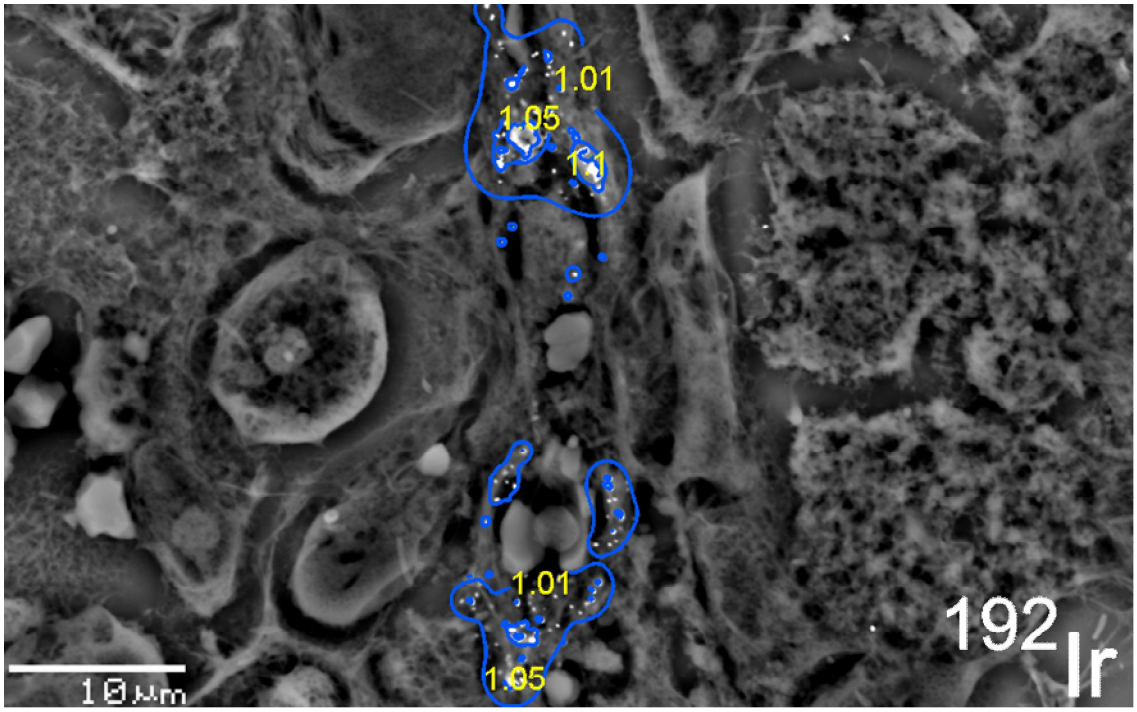

Figure B.1: Microscopic Dose Enhancement from ^{192}Ir photon source for the specific GNP distribution *in vivo* obtained from the previous work.[32]

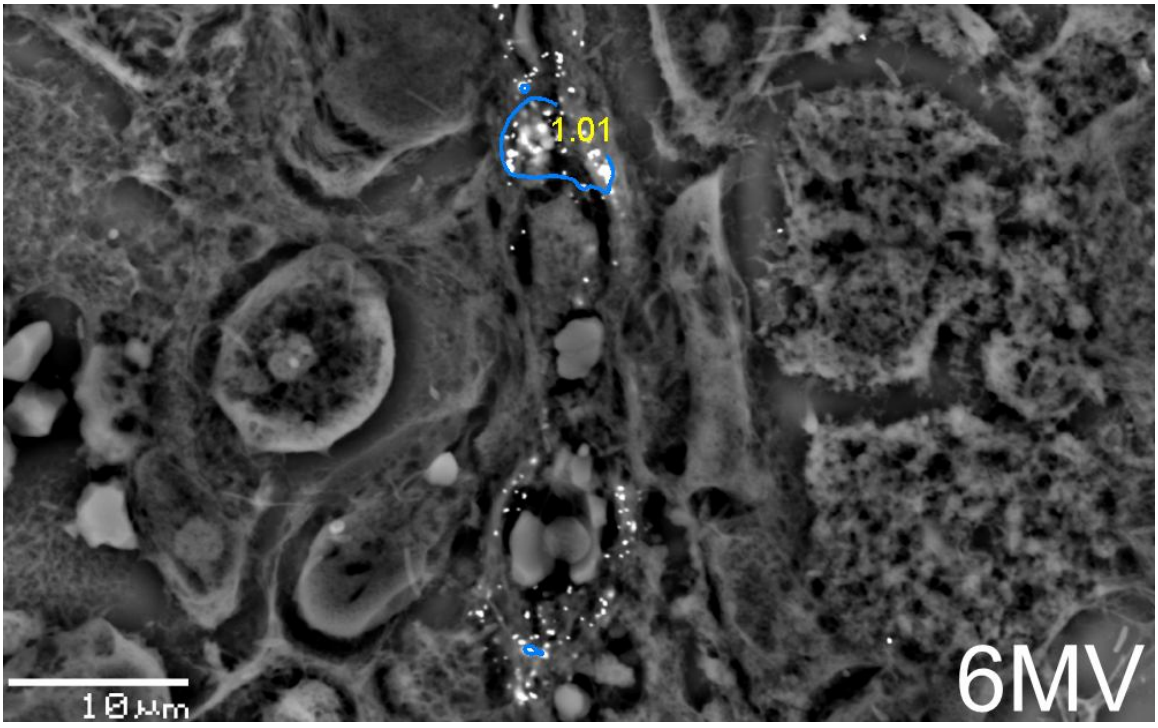

Figure B.1: Microscopic Dose Enhancement from 6 MV photon source for the specific GNP distribution *in vivo* obtained from the previous work.[32]

APPENDIX C

SAMPLE INPUT CODES

C.1 - Sample NOREC Input Code

```
#include <iostream>
#include <fstream>
#include "track.h"
#include <ctime>
#include <math.h>
#include <signal.h>
#include <windows.h>

using namespace std;
using std::cout;

const double pi = 3.14159265;

double norec_source(double *, float *, int, RandomNumber &);
//samples the source spectrum

void isotropic(double &, double &, double &, RandomNumber &);
//isotropically generates a direction vector

volatile int ctrlc_pressed = 0;
void ctrlc_handler ( int sig ) {
    ctrlc_pressed = 1;
}


int main(int argc, char *argv[])
{
  long int time1=time(0), time2;
  double timer;
  RandomNumber ran;
  ran.setSeed((unsigned)time(0));
  int k, j, N, nps, rbin;
  double *E, energy=0;
  float *prob;
  double u=0,v=0,w=1;
  double r_max;

  int Nbins;
  long double * dose;
  long int * hits;
  char fn[80], fn2[80];
  ifstream spec, inp;
  ofstream output;

  signal( SIGINT, ctrlc_handler );

  if (argc != 2)
  {
```

```
    cout << "NOREC <filename>\n";
    return 0;
  }
  inp.open(argv[1], ios::in); //open the input file

  //read the name of the input spectrum filename and open it
  inp >> fn;
  spec.open(fn, ios::in);
  inp >> fn;

  inp >> nps;  //number of particles to simulate
  inp >> Nbins; //total number of dose bins
  inp >> r_max; //maximum radius to transport particles to
  if (!(spec.is_open() ))
  {
    cout << "Problem with filenames " << argv[1] << ' ' << argv[2] <<
'\n';
    return 0;
  }
  dose = new long double [Nbins]; //energy deposition in each bin
  hits=new long int [Nbins]; //number of deposition events in each bin


  //initialize energy deposition to zero
  for (k=0; k<Nbins; k++)
  {
    dose[k]=0;
    hits[k]=0;
  }




  cout << "\n\n-----------------------------------------------------" <<
'\n';
  cout << "Running NOREC for spectrum in file " << argv[1] << '\n';
  cout << "-----------------------------------------------------" <<
'\n';
  cout << "Number of Histories to run: " << nps << '\n' << '\n';


  ////////////////////////
  //READ INPUT SPECTRUM//
  ////////////////////////
  spec >> N;
    E = new double [N];
    prob = new float [N];
  for (k=0; k<N; ++k)
    spec >> E[k] >> prob[k];

  //normalize probabilities
  double max=0;
  for (k=0; k<N; ++k)
    if (prob[k] > max)
      max=prob[k];
  for (k=0; k<N; ++k)
    prob[k]/=max;
```

```
  ////////////////////////////
  //BEGIN MAIN TRANSPORT LOOP//
  ////////////////////////////

    Track t;
  double x, y, z, r;
  for (k=0; k<nps; ++k)
  {
    if (k==nps/100)
    {
      time2=time(0);
      timer=time2-time1;
      cout << (double(nps)-k)*timer/3600/k << " hours remain\n";
    }
    if (k%(nps/10)==0)
    {
      cout << "Particle #" << k << '\n';
      if (k)
      {
        for (j=0; fn[j]!='\0';j++)
          fn2[j]=fn[j];
        fn2[j]='0'+10*k/nps;
        fn2[j+1]='\0';
        output.open(fn2, ios::out);
        output << "R(um)\tDose(eV)\tError(%)\n";
        for (j=1; j<Nbins; ++j)
          output << (j)*r_max/Nbins << '\t' << dose[j]/nps << "\t\t" <<
100/sqrt(float(hits[j])) << '\n';
        output.close();
      }
    }


    //isotropically generate a direction vector
    isotropic(u,v,w,ran);


    //allow user to pause simulation to check progress
    if (ctrlc_pressed)
    {
      cout << "------------------------------------------------------
-\n";
      cout << "INTERRUPT at particle " << k << '\n';
      time2=time(0);
      timer=time2-time1;
      int status_input = 1;
      while (status_input)
      {
        cout << "d: Dump dose information to file\n";
        cout << "q: Dump dose information to file and exit\n";
        cout << "Q: Exit without saving\n";
        cout << "c: Continue running\n";
        cout << (double(nps)-k)*timer/3600/k << " hours remain\n";

        char status;
```

```
        cin >> status;
        if (status == 'd' || status == 'q')
        {
          status_input = 0;
          output.open(fn, ios::out);
          output << "R(um)\tDose(eV)\tError(%)\n";
          for (j=1; j<Nbins; ++j)
            output << (j)*r_max/Nbins << '\t' << dose[j]/k << "\t\t" <<
100/sqrt(float(hits[j])) << '\n';
          if (status == 'q')
            return 0;
          output.close();
        }
        else if (status == 'Q')
          return 0;
        else if (status == 'c')
          status_input = 0;
      }

      ctrlc_pressed=0;
      signal( SIGINT, ctrlc_handler );
      cout << "----------------------------------------------------------
-\n\n";
    }


    //sample from the energy spectrum until a result < 1MeV is obtained
    do
      energy=1000000*norec_source(E, prob, N, ran); //energy in eV
    while (energy > 1000000);

    t.generateTrack(energy,0,0,0,u,v,w); //generate particle
    int escape = 0;

    //transport particle until it falls below energy threshold or
escapes
    while(!t.isOver() && !escape)
    {
      t.getLine(&x,&y,&z,&energy);  //determine location and energy of
next event
      r=sqrt(pow(x,2)+pow(y,2)+pow(z,2)); //calculate radial position

      //if particle is within geometry, deposit its energy in the
appropriate bin
      if (r<r_max)
      {
        rbin = ceil(r/r_max*Nbins);
        dose[rbin] += energy;
        hits[rbin]++;
      }
      else
        escape=1;
    }
  }

  //output results and clean up memory
  output.open(fn, ios::out);
```

```
  output << "R(um)\tDose(eV)\tError(%)\n";
  for (k=1; k<Nbins; ++k)
    output << (k)*r_max/Nbins << '\t' << dose[k]/nps << "\t\t" <<
100/sqrt(float(hits[k])) << '\n';

  spec.close();
  output.close();
  inp.close();
  delete E, prob, dose, hits;

  time2=time(0);
  timer=time2-time1;
  cout << '\n' << nps << " particles in " << timer/3600 << " hours\n";
  cout << nps/timer*3600 << " particles per hour\n";

  return 0;
}


double norec_source(double * E, float * prob, int N, RandomNumber &r)
{
/*  E - energy bins
  E[0] = energy lower bound - below this bin prob = 0
  prob[0] = 0
*/

  int finished = 0, bin;
  double lower, upper;

  bin = floor(r.ran2()*N);
  while (r.ran2() > prob[bin])
    bin = floor(r.ran2()*N);

  upper = E[bin];
  lower = E[bin-1];

  return (r.ran2()*(upper-lower)+lower);
}

void isotropic(double &u, double &v, double &w, RandomNumber &r)
{
  double phi, theta;

  phi = pi*r.ran2();
  theta = 2*pi*(r.ran2()-1);

  u = sin(phi)*cos(theta);
  v = sin(phi)*sin(theta);
  w = cos(phi);

  return;
}
```

REFERENCES

1. H. F. Dvorak, J. A. Nagy, J. T. Dvorak and A. M. Dvorak, "Identification and characterization of the blood vessels of solid tumors that are leaky to circulating macromolecules," Am J Pathol **133**, 95-109 (1988).
2. H. Maeda, J. Fang, T. Inutsuka and Y. Kitamoto, "Vascular permeability enhancement in solid tumor: various factors, mechanisms involved and its implications," Int Immunopharmacol **3**, 319-328 (2003).
3. I. El-Sayed, X. Huang and M. El-Sayed, "Surface plasmon resonance scattering and absorption of anti-EGFR antibody conjugated gold nanoparticles in cancer diagnostics: applications in oral cancer," Nano Lett **5**, 829-834 (2005).
4. J. A. Copland, M. Eghtedari, V. L. Popov, N. Kotov, N. Mamedova, M. Motamedi and A. A. Oraevsky, "Bioconjugated gold nanoparticles as a molecular based contrast agent: implications for imaging of deep tumors using optoacoustic tomography," Mol Imaging Biol **6**, 341-349 (2004).
5. P. Mukherjee, R. Bhattacharya, N. Bone, Y. K. Lee, C. R. Patra, S. Wang, L. Lu, C. Secreto, P. C. Banerjee, M. J. Yaszemski, N. E. Kay and D. Mukhopadhyay, "Potential therapeutic application of gold nanoparticles in B-chronic lymphocytic leukemia (BCLL): enhancing apoptosis," J Nanobiotechnology **5**, 4 (2007).
6. J. Li, A. Chaudhary, S. J. Chmura, C. Pelizzari, T. Rajh, C. Wietholt, M. Kurtoglu and B. Aydogan, "A novel functional CT contrast agent for molecular imaging of cancer," Phys Med Biol **55**, 4389-4397 (2010).
7. R. Mello, H. Callisen, J. Winter, A. Kagan and A. Norman, "Radiation dose enhancement in tumors with iodine," Medical Physics **10**, 75 (1983).
8. P. Dawson, M. Penhaligon, E. Smith and J. Saunders, "Iodinated contrast agents as" radiosensitisers"," British Journal of Radiology **60**, 201 (1987).
9. K. Iwamoto, S. Cochran, J. Winter, E. Holburt, R. Higashida and A. Norman, "Radiation dose enhancement therapy with iodine in rabbit VX-2 brain tumors," Radiotherapy and Oncology **8**, 161-170 (1987).
10. J. Holt Rose, A. Norman and M. Ingram, "First experience with radiation therapy of small brain tumors delivered by a computerized tomography scanner," International Journal of Radiation Oncology* Biology* Physics **30**, 166-167 (1994).
11. A. Mesa, A. Norman, T. Solberg, J. Demarco and J. Smathers, "Dose distributions using kilovoltage x-rays and dose enhancement from iodine contrast agents," Physics in Medicine and Biology **44**, 1955 (1999).
12. J. Robar, S. Riccio and M. Martin, "Tumour dose enhancement using modified megavoltage photon beams and contrast media," Physics in Medicine and Biology **47**, 2433 (2002).
13. F. Verhaegen, B. Reniers, F. Deblois, S. Devic, J. Seuntjens and D. Hristov, "Dosimetric and microdosimetric study of contrast-enhanced radiotherapy with kilovolt x-rays," Physics in Medicine and Biology **50**, 3555 (2005).

14. J. Robar, "Generation and modelling of megavoltage photon beams for contrast-enhanced radiation therapy," Physics in Medicine and Biology **51**, 5487 (2006).
15. F. Adams, A. Norman, R. Mello and D. Bass, "Effect of radiation and contrast media on chromosomes. Preliminary report," Radiology **124**, 823 (1977).
16. J. F. Hainfeld, D. N. Slatkin and H. M. Smilowitz, "The use of gold nanoparticles to enhance radiotherapy in mice," Phys Med Biol **49**, N309-315 (2004).
17. J. F. Hainfeld, F. A. Dilmanian, D. N. Slatkin and H. M. Smilowitz, "Radiotherapy enhancement with gold nanoparticles," J Pharm Pharmacol **60**, 977-985 (2008).
18. J. Hainfeld, F. Dilmanian, Z. Zhong, D. Slatkin, J. Kalef-Ezra and H. Smilowitz, "Gold nanoparticles enhance the radiation therapy of a murine squamous cell carcinoma," Physics in Medicine and Biology **55**, 3045 (2010).
19. S. H. Cho, "Estimation of tumour dose enhancement due to gold nanoparticles during typical radiation treatments: a preliminary Monte Carlo study," Physics in Medicine and Biology **50**, N163 (2005).
20. S. H. Cho, B. L. Jones and S. Krishnan, "The dosimetric feasibility of gold nanoparticle-aided radiation therapy (GNRT) via brachytherapy using low-energy gamma-/x-ray sources," Phys Med Biol **54**, 4889-4905 (2009).
21. J. Roeske, L. Nunez, M. Hoggarth, E. Labay and R. Weichselbaum, "Characterization of the theorectical radiation dose enhancement from nanoparticles," Technology in cancer research & treatment **6**, 395-401 (2007).
22. D. Medich, M. Tries and J. Munro III, "Monte Carlo characterization of an ytterbium-169 high dose rate brachytherapy source with analysis of statistical uncertainty," Medical Physics **33**, 163 (2006).
23. K. Parodi, A. Ferrari, F. Sommerer and H. Paganetti, "Clinical CT-based calculations of dose and positron emitter distributions in proton therapy using the FLUKA Monte Carlo code," Phys Med Biol **52**, 3369-3387 (2007).
24. K. Sokolov, M. Follen, J. Aaron, I. Pavlova, A. Malpica, R. Lotan and R. Richards-Kortum, "Real-time vital optical imaging of precancer using anti-epidermal growth factor receptor antibodies conjugated to gold nanoparticles," Cancer research **63**, 1999 (2003).
25. J. Hainfeld, D. Slatkin, T. Focella and H. Smilowitz, "Gold nanoparticles: a new X-ray contrast agent," British Journal of Radiology **79**, 248 (2006).
26. X. Qian, X. H. Peng, D. O. Ansari, Q. Yin-Goen, G. Z. Chen, D. M. Shin, L. Yang, A. N. Young, M. D. Wang and S. Nie, "In vivo tumor targeting and spectroscopic detection with surface-enhanced Raman nanoparticle tags," Nat Biotechnol **26**, 83-90 (2008).
27. P. Diagaradjane, J. Orenstein-Cardona, N. Colon-Casasnovas, A. Deorukhkar, S. Shentu, N. Kuno, D. Schwartz, J. Gelovani and S. Krishnan, "Imaging epidermal growth factor receptor expression in vivo: pharmacokinetic and biodistribution characterization of a bioconjugated quantum dot nanoprobe," Clinical Cancer Research **14**, 731 (2008).
28. B. L. Jones, S. Krishnan and S. H. Cho, "Estimation of microscopic dose enhancement factor around gold nanoparticles by Monte Carlo calculations," Med Phys **37**, 3809-3816 (2010).

29. L. R. Hirsch, R. J. Stafford, J. A. Bankson, S. R. Sershen, B. Rivera, R. E. Price, J. D. Hazle, N. J. Halas and J. L. West, "Nanoshell-mediated near-infrared thermal therapy of tumors under magnetic resonance guidance," Proc Natl Acad Sci U S A **100**, 13549-13554 (2003).
30. P. Diagaradjane, A. Shetty, J. C. Wang, A. M. Elliott, J. Schwartz, S. Shentu, H. C. Park, A. Deorukhkar, R. J. Stafford, S. H. Cho, J. W. Tunnell, J. D. Hazle and S. Krishnan, "Modulation of in vivo tumor radiation response via gold nanoshell-mediated vascular-focused hyperthermia: characterizing an integrated antihypoxic and localized vascular disrupting targeting strategy," Nano Lett **8**, 1492-1500 (2008).
31. G. von Maltzahn, J. Park, A. Agrawal, N. Bandaru, S. Das, M. Sailor and S. Bhatia, "Computationally guided photothermal tumor therapy using long-circulating gold nanorod antennas," Cancer research **69**, 3892 (2009).
32. S. Krishnan, P. Diagaradjane and S. Cho, "Nanoparticle-mediated thermal therapy: Evolving strategies for prostate cancer therapy," International Journal of Hyperthermia, 1-15 (2010).
33. P. Boisseau and Massachusetts Institute of Technology. Dept. of Physics., Thesis Ph. D. --Massachusetts Institute of Technology Dept. of Physics 1986., 1986.
34. R. Cesareo and S. Mascarenhas, "A new tomographic device based on the detection of fluorescent x-rays," Nuclear Instruments and Methods in Physics Research Section A: Accelerators, Spectrometers, Detectors and Associated Equipment **277**, 669-672 (1989).
35. J. P. Hogan, R. A. Gonsalves and A. S. Krieger, "Fluorescent computer tomography: a model for correction of X-ray absorption," Nuclear Science, IEEE Transactions on **38**, 1721-1727 (1991).
36. T. Yuasa, M. Akiba, T. Takeda, M. Kazama, A. Hoshino, Y. Watanabe, K. Hyodo, F. A. Dilmanian, T. Akatsuka and Y. Itai, "Reconstruction method for fluorescent X-ray computed tomography by least-squares method using singular value decomposition," Nuclear Science, IEEE Transactions on **44**, 54-62 (1997).
37. A. Simionovici, M. Chukalina, C. Schroer, M. Drakopoulos, A. Snigirev, I. Snigireva, B. Lengeler, K. Janssens and F. Adams, "High-resolution X-ray fluorescence microtomography of homogeneous samples," Nuclear Science, IEEE Transactions on **47**, 2736-2740 (2000).
38. T. Takeda, Q. Yu, T. Yashiro, T. Zeniya, J. Wu, Y. Hasegawa, L. Thet Thet, K. Hyodo, T. Yuasa, F. A. Dilmanian, T. Akatsuka and Y. Itai, "Iodine imaging in thyroid by fluorescent X-ray CT with 0.05 mm spatial resolution," Nuclear Instruments and Methods in Physics Research Section A: Accelerators, Spectrometers, Detectors and Associated Equipment **467-468**, 1318-1321 (2001).
39. R. Zaman, P. Diagaradjane, J. Wang, J. Schwartz, N. Rajaram, K. Gill-Sharp, S. Cho, H. Rylander, J. Payne and S. Krishnan, "In vivo detection of gold nanoshells in tumors using diffuse optical spectroscopy," IEEE Journal of Selected Topics in Quantum Electronics **13**, 1715 (2007).
40. T. Johnson, B. Krauß, M. Sedlmair, M. Grasruck, H. Bruder, D. Morhard, C. Fink, S. Weckbach, M. Lenhard and B. Schmidt, "Material differentiation by dual energy CT: initial experience," European radiology **17**, 1510-1517 (2007).

41. J. P. Schlomka, E. Roessl, R. Dorscheid, S. Dill, G. Martens, T. Istel, C. Baumer, C. Herrmann, R. Steadman, G. Zeitler, A. Livne and R. Proksa, "Experimental feasibility of multi-energy photon-counting K-edge imaging in pre-clinical computed tomography," Phys Med Biol **53**, 4031-4047 (2008).
42. S. K. Cheong, B. L. Jones, A. K. Siddiqi, F. Liu, N. Manohar and S. H. Cho, "X-ray fluorescence computed tomography (XFCT) imaging of gold nanoparticle-loaded objects using 110 kVp x-rays," Phys Med Biol **55**, 647-662 (2010).
43. J. Park, A. Estrada, J. A. Schwartz, P. Diagaradjane, S. Krishnan, A. K. Dunn and J. W. Tunnell, "Intra organ biodistribution of gold nanoparticles using intrinsic two photon induced photoluminescence," Lasers in Surgery and Medicine **42**, 630-639 (2010).
44. F. H. Attix and E. Corporation, "Introduction to radiological physics and radiation dosimetry," (1986).
45. B. Jones, "Monte Carlo calculations of microscopic dose enhancement for gold nanoparticle-aided radiation therapy," (2009).
46. V. Semenenko, J. Turner and T. Borak, "NOREC, a Monte Carlo code for simulating electron tracks in liquid water," Radiation and environmental biophysics **42**, 213-217 (2003).
47. S. Cho, O. Vassiliev and J. Horton, "Comparison between an event-by-event Monte Carlo code, NOREC, and ETRAN for electron scaled point kernels between 20 keV and 1 MeV," Radiation and environmental biophysics **46**, 77-83 (2007).
48. C. Bousis, D. Emfietzoglou, P. Hadjidoukas and H. Nikjoo, "A Monte Carlo study of absorbed dose distributions in water in the vapour and liquid phases by intermediate energy electrons: the effect of different condensedhistory schemes," Phys. Med. Biol **53**, 3739–3761 (2008).
49. D. Rogers, I. Kawrakow, J. Seuntjens, B. Walters and E. Mainegra-Hing, "NRC user codes for EGSnrc," National Research Council of Canada Report (2001).
50. M. K. K. Leung, J. C. L. Chow, B. D. Chithrani, M. J. G. Lee, B. Oms and D. A. Jaffray, "Irradiation of gold nanoparticles by x-rays: Monte Carlo simulation of dose enhancements and the spatial properties of the secondary electrons production," Medical Physics **38**, 624 (2011).
51. D. Regulla, L. Hieber and M. Seidenbusch, "Physical and biological interface dose effects in tissue due to X-ray-induced release of secondary radiation from metallic gold surfaces," Radiation research **150**, 92-100 (1998).
52. G. F. Rust and J. Weigelt, "X-ray fluorescent computer tomography with synchrotron radiation," Nuclear Science, IEEE Transactions on **45**, 75-88 (2005).
53. H. von Busch, G. Harding, G. Martens, J. P. Schlomka and B. Schweizer, 2005 (unpublished).
54. S. Cherry, J. Sorenson and M. Phelps, "Physics in Nuclear Medicine 3rd edn (Philadelphia, PA: Saunders)," (2003).
55. L. Shepp and Y. Vardi, "Maximum likelihood reconstruction for emission tomography," Medical Imaging, IEEE Transactions on **1**, 113-122 (2007).
56. K. Lange and R. Carson, "Em Reconstruction Algorithms for Emission and Transmission Tomography," Journal Of Computer Assisted Tomography **8**, 306-316 (1984).

57. X-5 Monte Carlo Team, "MCNP-A General Purpose Monte Carlo N-Particle Transport Code, Version 5," LA-UR-03-1987 (2003).
58. B. Silverman, M. Jones, J. Wilson and D. Nychka, "A Smoothed EM Approach to Indirect Estimation Problems, with Particular, Reference to Stereology and Emission Tomography," Journal of the Royal Statistical Society. Series B (Methodological) **52**, 271-324 (1990).
59. E. Slijpen and F. Beekman, "Comparison of post-filtering and filtering between iterations for SPECT reconstruction," Nuclear Science, IEEE Transactions on **46**, 2233-2238 (2002).
60. F. Catté, P. Lions, J. Morel and T. Coll, "Image selective smoothing and edge detection by nonlinear diffusion," SIAM Journal on Numerical Analysis **29**, 182-193 (1992).
61. C. Coffey, L. DeWerd, C. Liu, R. Nath, S. Seltzer and J. Seuntjens, "AAPM protocol for 40–300 kV x-ray beam dosimetry in radiotherapy and radiobiology," Medical Physics **28**, 868 (2001).
62. G. Jost, S. Golfier, R. Lawaczeck, H. J. Weinmann, M. Gerlach, L. Cibik, M. Krumrey, D. Fratzscher, J. Rabe and V. Arkadiev, "Imaging-therapy computed tomography with quasi-monochromatic x-rays," European Journal of Radiology **68**, S63-S68 (2008).
63. G. Jost, T. Mensing, S. Golfier, R. Lawaczeck, H. Pietsch, J. Hütter, L. Cibik, M. Gerlach, M. Krumrey and D. Fratzscher, "Photoelectric-enhanced radiation therapy with quasi-monochromatic computed tomography," Medical Physics **36**, 2107 (2009).
64. I. Grigorieva and A. Antonov, "HOPG as powerful x ray optics," X Ray Spectrometry **32**, 64-68 (2003).
65. E. J. Hall and A. J. Giaccia, *Radiobiology for the Radiologist*. (Lippincott Williams & Wilkins, 2006).
66. P. L. Chow, A. L. Goertzen, F. Berger, J. J. DeMarco and A. F. Chatziioannou, 2002 (unpublished).
67. J. Boone, O. Velazquez and S. Cherry, "Small-animal X-ray dose from micro-CT," Molecular imaging: official journal of the Society for Molecular Imaging **3**, 149 (2004).
68. A. Obenaus and A. Smith, "Radiation dose in rodent tissues during micro-CT imaging," Journal of X-Ray Science and Technology **12**, 241-249 (2004).
69. S. C. Lee, H. K. Kim, I. K. Chun, M. H. Cho and S. Y. Lee, "A flat-panel detector based micro-CT system: performance evaluation for small-animal imaging," Physics in Medicine and Biology **48**, 4173 (2003).
70. W. Ngwa, G. M. Makrigiorgos and R. I. Berbeco, "Applying gold nanoparticles as tumor-vascular disrupting agents during brachytherapy: estimation of endothelial dose enhancement," Physics in Medicine and Biology **55**, 6533 (2010).
71. I. Kawrakow and D. Rogers, "The EGSnrc code system," NRCC Report PIRS-701 (Nov. 7, 2003).
72. C. Ling, E. Yorke, I. Spiro, D. Kubiatowicz and D. Bennett, "Physical dosimetry of 125I seeds of a new design for interstitial implant," International Journal of Radiation Oncology* Biology* Physics **9**, 1747-1752 (1983).

73. Z. Chen and R. Nath, "Dose rate constant and energy spectrum of interstitial brachytherapy sources," Medical Physics **28**, 86 (2001).
74. S. Cho, O. Vassiliev, S. Lee, H. Liu, G. Ibbott and R. Mohan, "Reference photon dosimetry data and reference phase space data for the 6 MV photon beam from Varian Clinac 2100 series linear accelerators," Medical Physics **32**, 137 (2005).
75. M. Birch and R. Blowes, "A contact x-ray therapy unit for intracavitary irradiation," Physics in Medicine and Biology **35**, 275 (1990).
76. G. Gutman, E. Sozontov, E. Strumban, F. Yin, S. Lee and J. Kim, "A novel needle-based miniature x-ray generating system," Physics in Medicine and Biology **49**, 4677 (2004).
77. M. Rivard, S. Davis, L. DeWerd, T. Rusch and S. Axelrod, "Calculated and measured brachytherapy dosimetry parameters in water for the Xoft Axxent x-ray source: An electronic brachytherapy source," Medical Physics **33**, 4020 (2006).
78. R. Birch, M. Marshall, G. Ardran and H. P. A. D. R. T. Group, *Catalogue of spectral data for diagnostic x-rays*. (Hospital Physicists' Association, 1979).